

**University of Alberta**

Spectroscopy of methane using a vertical cavity surface-emitting laser  
system with emphasis on development for portable applications

by

Matthew Dzikowski

A thesis submitted to the Faculty of Graduate Studies and Research  
in partial fulfillment of the requirements for the degree of

Master of Science

in

Photonics and Plasmas

Department of Electrical and Computer Engineering

©Matthew Dzikowski

Fall, 2009

Edmonton, Alberta

Permission is hereby granted to the University of Alberta Libraries to reproduce single copies of this thesis and to lend or sell such copies for private, scholarly or scientific research purposes only. Where the thesis is converted to, or otherwise made available in digital form, the University of Alberta will advise potential users of the thesis of these terms.

The author reserves all other publication and other rights in association with the copyright in the thesis and, except as herein before provided, neither the thesis nor any substantial portion thereof may be printed or otherwise reproduced in any material form whatsoever without the author's prior written permission.

**Examining Committee**

Supervisor: Dr. John Tulip

Committee member: Dr. Ying Tsui

Committee member: Dr. Wolfgang Jaeger

Chair: Dr. Vien Van

**Department**

(ECE)

(ECE)

(Chemistry)

(ECE)

## **Abstract**

There is a great deal of interest in monitoring atmospheric greenhouse gases such as methane. Although distributed feedback edge-emitting lasers are often used for atmospheric detection, the development of the vertical cavity surface-emitting laser (VCSEL) has allowed for an alternative source. The VCSEL exhibits several advantages over distributed feedback (DFB), edge-emitting lasers, especially in terms of power requirements and tuning capabilities. A second harmonic spectroscopy system based on a VCSEL laser is presented. Battery operation of the driver, temperature control and receiver is achieved. The system is used to detect methane gas in open path situations, as well as in gas cylinders. Temperature and current scanning are compared as methods for laser wavelength modulation. Mathematical methods for characterizing and filtering absorption signals are investigated. The receiver system is also used with a DFB laser to compare performance with the VCSEL. A software receiver using LabVIEW is implemented, and its performance is compared with the hardware designs. A minimum detectable limit of 1.4 ppm-m of methane for the hardware receiver is reported.

## Table of Contents

<b>Chapter 1. Introduction.....</b>	<b>1</b>
1.1 Gases in the Atmosphere.....	1
1.2 Laser Spectroscopy .....	2
1.3 Research Goals.....	3
1.4 Outline of Topics .....	4
<b>Chapter 2. Background Information .....</b>	<b>5</b>
2.1 Principles of Absorption .....	5
2.2 Line Shape and Line Broadening.....	6
2.3 Spectroscopy Mechanics.....	8
2.4 Wavelength Modulation Spectroscopy (2f).....	15
2.5 VCSEL Fundamentals.....	22
2.6 Literature Review.....	24
<b>Chapter 3. System Design.....</b>	<b>28</b>
3.1 The Driver Board .....	28
3.2 High Frequency Modulation .....	32
3.3 Design of the Ramp Generator.....	33
3.4 Receiving and Data Processing Systems.....	33
3.4.1 Photodiode and Front End Amplifier.....	34
3.4.2 Phase Locked Loop Detection System.....	34
3.4.3 External Reference Receiver.....	37

<b>Chapter 4. Experimental Results</b> .....	<b>39</b>
4.1 Receiver Functionality Demonstration .....	39
4.2 Modulation Index and Temperature Scanning.....	44
4.3 Current Scan Results and Receiver Comparison .....	50
4.4 Waveform Validation .....	52
4.5 Open Path Results .....	53
4.6 Data Processing.....	55
4.7 Wavelet Transforms .....	61
4.8 Noise Factors.....	69
4.9 Distributed Feedback (DFB) Laser Characterization.....	73
4.10 Software and Hardware Receiver Comparison .....	75
4.11 Minimum Detectable Limit.....	80
<b>Chapter 5. Conclusion</b> .....	<b>83</b>
<b>Bibliography</b> .....	<b>86</b>
<b>Appendix</b> .....	<b>i</b>

## **List of Tables**

1 – Optical modulation indices for various modulation amplitudes	48
2 – Value of the regression coefficient at various concentrations	59
3 – Regression coefficients and signal to noise ratios for different receivers	81

## List of Figures

2.1	Possible transitions between two energy levels	5
2.2	A Lorentzian function	7
2.3	The general wavelength range for each type of transition	9
2.4	Electronic, vibrational and rotational energy levels	9
2.5	Normal vibrations of a tetrahedral molecule	12
2.6	Branches of ro-vibrational transitions	13
2.7	$I_f$ absorption and dispersion signals as a function of normalized modulation index	17
2.8	Theoretical WMS at the first three harmonics of the Lorentzian line shape	20
2.9	Absorption signal amplitude versus modulation index for several different cases	21
2.10	Basic VCSEL structure	22
2.11	A TO-46 packaged VCSEL	24
2.12	Portable Spectroscopy System	25
2.13	A portable remote methane detector based on a DFB laser	26
3.1	Experimental VCSEL system	28
3.2	Block diagram of the high frequency modulation circuit	33
3.3	Block diagram of the PLL receiver system	37
3.4	External reference receiver block diagram	38
4.1	Receiver input from the photodiode, 500ppm·m gas sample	39
4.2	Output of the 20 kHz bandpass filters with a 500ppm·m gas methane sample	40
4.3	VCO 20 kHz output compared to signal 20 kHz and filtered signal 20 kHz	41
4.4	Mixer output with a 500ppm·m gas sample	41
4.5	PLL receiver final output, 512 averages (500ppm·m)	42
4.6	Frequency domain signals at various stages of the PLL receiver	42
4.7	External reference receiver waveform shifting	44
4.8	Temperature scan results for various modulation indices	45
4.9	Signal to noise ratios for various modulation indices	47
4.10	PLL receiver noise values for various modulation indices	49
4.11	Current scan results from PLL and external reference receivers	50
4.12	External reference receiver with no light input	52
4.13	Open path methane measurement, compared with cell reference	55
4.14	The effect of shifting and windowing on $R^2$ and $\beta$	57
4.15	Experimental and theoretical regression slopes for various concentrations	58
4.16	$R^2$ versus concentration	60
4.17	The Mexican hat wavelet	62
4.18	Surface plot of the wavelet transform of a 50 ppm absorption signal	63
4.19	Previous plot viewed from another angle	64
4.20	Cross-section of the same figure at several different dilation values	64
4.21	Wavelet transform of a 0 ppm signal, $R^2 = 0.255$	65

4.22	Wavelet transform of a 0 ppm signal, $R^2 = 0.00026$	66
4.23	Wavelet adjusted $R^2$ versus concentration	67
4.24	A sample scan with no gas, and its closest matching wavelet transform	68
4.25	Averaged 2 <sup>nd</sup> harmonic outputs with no optical elements in the system	72
4.26	PLL 2 <sup>nd</sup> harmonic output using a DFB source	74
4.27	Open path experimental design for comparison of hardware and software	76
4.28	High concentration measurements for the PLL, external ref. and software	76
4.29	4.0 meter open path measurement for external reference and software	77
4.30	1.0 meter open path measurements for hardware and software	78
4.31	Experimental system for feedback noise reduction	79
4.32	Hardware and software feedback reduction measurements, 1 m path open path	80

# Chapter 1: Introduction

## 1.1 Gases in the Atmosphere

Gases in the world around us are of great interest, as much for environmental concerns as for health and safety issues. The atmosphere is an amalgam of dozens of different gases. Although nitrogen and oxygen form more than 98% <sup>(1)</sup> of atmospheric gas by volume, trace gases play an important role in everything from weather and precipitation to pollution and health issues. Gases such as carbon monoxide and nitrous oxide can be highly dangerous to human life, even in fairly small concentrations. Pollution in urban centers can greatly alter the most basic aspects of life; cities such as Jakarta, Beijing and London have experienced smog so severe that asthmatics and persons with respiratory difficulties could not leave their houses <sup>(2)</sup>. Poor atmospheric air quality also leads to long term health effects such as increased cancer rates, higher asthma instances, and birth defects <sup>(3) (4)</sup>. On a smaller scale, gas mixtures in personal residences and industrial applications are paramount to health and safety. Carbon monoxide has been responsible for thousands of deaths in homes over the years. Poisonous gases have been notorious killers in mines dating back centuries, and air monitoring is still extremely important in mining today. Chemical plants, oil rigs, pulp and paper mills, steel mills; virtually every type of heavy industry or manufacturing plant involves processes that entail harmful gases. For all of these applications and many more, there is a highly warranted interest in monitoring the air around us.

In recent years, greenhouse gases have been of particular interest in the atmosphere due to their connection to global warming. Greenhouse gases act as a medium to trap some of the radiation emitted by the sun in the atmosphere, warming the planet. The greenhouse effect is virtually a basic need for human life; without it, the Earth would be an average of nearly 30C colder <sup>(5)</sup>. Despite the merits of the greenhouse effect, many worry that a drastic increase in the

quantities of greenhouse gases in the air will lead to a much warmer Earth, with dire consequences on the environment. This phenomenon is called global warming. Although there is still debate over the validity of global warming, the risk has certainly been enough to shift public perception and policy-making. As a result, monitoring greenhouse gases in the atmosphere, and the sources of greenhouse gas emission has become an important field. The main greenhouse gases are water, carbon dioxide, ozone and hydrocarbon compounds such as methane.

## **1.2 Laser Spectroscopy**

Spectroscopy is a constantly evolving field with applications in many diversified areas. It is used in atmospheric monitoring, medical sensing, industrial safety and monitoring, and greenhouse gas measurements. Spectroscopy has three major fields of study: absorption, emission and scattering. The work presented in this these focuses on absorption spectroscopy, and more specifically, tunable diode laser absorption spectroscopy (TDLAS).

Although laser absorption spectroscopy is a relatively established technology, recent developments in semiconductor lasers have enabled new possibilities for laser gas detection. Semiconductor lasers are much smaller and require less power than other types of lasers such as solid state lasers (Nd:YAG) or carbon dioxide lasers. Until recently, spectroscopy using semiconductor lasers has largely been the domain of edge emitting, distributed feedback (DFB) laser diodes. Most laser diodes are edge emitting lasers, meaning that the laser light emanates from the edge of the semiconductor wafer that forms the laser. Recently, a new type of laser known as the vertical cavity surface emitting laser (abbreviated as VCSEL) has been developed. VCSELs bring many exciting new possibilities to the field of laser spectroscopy. Owing to the fact that VCSELs emit vertically rather than edgewise, they tend to be considerably cheaper and easier to manufacture and test than DFB laser diodes <sup>(6)</sup>. VCSELs are also typically much smaller and have far lower power requirements than most laser

diodes. In addition, VCSEL lasers have one of the largest single mode tuning ranges among any type of laser – an important feature for spectroscopy.

It is interesting to note that, although VCSELs were developed primarily for applications in communications networks and fiber optics, overlap in the design criteria has also made VCSELs attractive for laser spectroscopy. Communications lasers are typically designed for extremely high modulation rates for data transmission, most VCSELs are capable of 3 Gbps transfer rates if not higher. Fortunately, spectroscopy applications use much lower modulation ranges, typically in the low kilohertz to low megahertz. Most fiber optic networks use wavelength transmission ranges around 1500 nm, owing to the fact that this wavelength tends to minimize dispersion and pulse spreading over long cables. As a result, most VCSELs emit near this wavelength range – also known as the near infrared range. There are several important gas absorption lines in this wavelength range, most notably for methane and carbon dioxide – two greenhouse gases of great interest. The ever present communication goals of minimizing power and space requirements also serve to support the possibility of portable gas sensing lasers.

### **1.3 Research Goals**

There is a variety of objectives this research attempts to explore. The primary goal is the development of a VCSEL based spectroscopy system which can be made portable, with the ultimate goal being open path measurements. Another important question this work investigates is whether or not there any advantages to employing analog detection methods as opposed to digitization. Although not confined to this particular work, the goal of improving signal to noise ratios in spectroscopy systems is continual, and vital to optimizing minimum detectable limits. As such, methods for minimizing noise, signal processing, and mathematical models for comparison play a significant role in this research. Lastly, the suitability of VCSELs for portable detection and spectroscopy in general is also an essential component of this thesis.

## **1.4 Outline of Topics**

Chapter 2 of this document is devoted to developing a theoretical basis for spectroscopy and VCSEL technology. Topics covered include absorption mechanics, rotational and vibrational transitions, VCSEL structure, line broadening and second harmonic detection theory. An exploration of some results demonstrated by other researchers is also presented.

Chapter 3 presents information on the VCSEL spectroscopy systems that were designed. The requirements for successful operation are analyzed, and the basics of the electronics are explained.

Chapter 4 is a detailed account of the experimental results generated by the spectroscopy system. Many different areas are explored, including temperature scanning, current scanning, a comparison of phase locked loop detection with external reference detection, and noise considerations. The results are also contrasted with theoretical expectations. Mathematical analysis methods for improving detection limits are examined. The minimum detectable signal level achieved is presented, and compared with results from other researchers.

Finally in Chapter 5, the results of the research are compared with the original goals of the project. Detection limits and system design are contrasted with previous work from other researchers. The VCSEL is evaluated as a source for portable spectroscopy, and new areas for improvement and further research are suggested.

## Chapter 2: Background Information

### 2.1 Principles of absorption

The underlying mechanism in laser spectroscopy is absorption of photon energy by molecules. The energy of an incident photon is given by

$$E = h\nu \quad (2.1)$$

where  $E$  is the photon energy,  $h$  is Planck's constant,  $6.626 \times 10^{-34}$  J·s, and  $\nu$  is the frequency of the photon. A photon can be absorbed by an atom or molecule when it matches one of the transitional energies of the atom or molecule (shown in Figure 2.1).

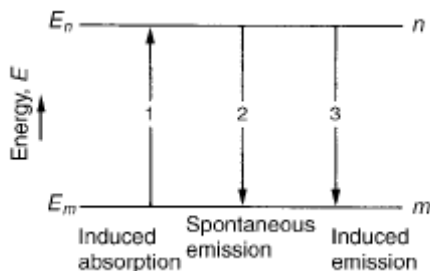


Figure 2.1 – Possible transitions between two energy levels  
Source: Hollas, M. J. Modern Spectroscopy, 4<sup>th</sup> Edition (2004) <sup>(7)</sup>.

The transitional energy between two states in an atom or molecule is governed by

$$\Delta E = E_n - E_m \quad (2.2)$$

where  $\Delta E$  is the difference between energy levels  $n$  and  $m$ . A photon of incident energy matching this transition energy can induce a transition in the atomic or molecular energy levels, and is thereby absorbed in the process <sup>(7)</sup>. Spontaneous emission is modeled by

$$E_n \rightarrow E_m + hc\tilde{\nu} \quad (2.3)$$

In spontaneous emission, a photon of wavenumber  $\tilde{\nu}$  is radiated by the spontaneous transition from energy level  $n$  to energy level  $m$ . Wavenumbers are frequently used to describe light (in units of  $\text{cm}^{-1}$ ), and are related to frequency by

$$\tilde{\nu} = \frac{\nu}{c} = \frac{1}{\lambda}, \quad (2.4)$$

where  $c$  is the speed of light, and  $\nu$  is the frequency of the photon <sup>(7)</sup>. Induced emission, also known as stimulated emission, such as the type found in lasers, operates somewhat differently. An incident photon of frequency  $\nu$  can cause a transition from energy level  $n$  to  $m$ , along with the re-emission of the incident photon, as well as a second photon at wavelength  $\nu$ .

## 2.2 Line Shape and Line Broadening

Quantum theory shows that energy levels in atomic structures are not confined to a single discrete value. Instead, energy levels are more precisely defined as energy regions, which are areas statistically likely to contain electrons. As a result, transitions between energy regions are not restricted to a single energy value (and therefore not to a specific wavelength). Therefore, transitions that cause absorption are actually the entire set of wavelengths that cause a transition over a continuous region of the electromagnetic spectrum. These sets typically form Gaussian curves centered on an average value, and are referred to as the line shape of the absorption.

One relevant feature of the line shape as it pertains to spectroscopy is the line width. The width of the line refers to the range of frequencies over which absorption occurs. It is important to note that all compounds exhibit a continuous absorption profile, with multiple separate absorption lines with varying strengths. In this context, the line width refers to a single absorption line of interest, centered on a specific frequency in the absorption profile. Line widths, often given the symbol  $\Delta\nu$ , typically describe the full-width, half maximum (FWHM) of the line shape. The reason the line width is of critical importance in laser spectroscopy relates to the laser's ability to accurately resolve the shape of the gas line, and therefore the associated absorption. Although lasers are often considered to emit at a single frequency, in actual fact all lasers have an associated output linewidth as well. When a laser emission is tuned through an absorption profile, the idea is to produce a convolution of the laser output with the absorption shape. In general, it is desirable to use a laser with a small linewidth, in order to minimize the length

of the convolution produced with the gas absorption line, thereby reducing or eliminating contributions from neighboring lines. It is worth noting that VCSELS typically exhibit very narrow emission linewidths, and are thusly very well suited to this spectroscopy consideration <sup>(7)</sup>.

Now that the importance of linewidth has been explained, the factors that affect the linewidths of gases are considered. These factors are generally referred to as line broadening effects.

Natural line broadening occurs when a species has an arbitrary energy level  $n$  populated in excess of the Boltzmann population (the equilibrium point between energy levels) as a result of absorption. Under these conditions, the width of the line is governed by the equation:

$$\Delta\nu \geq \frac{32\pi^3\nu^3}{(4\pi\epsilon_0)3hc^3} |R^{nm}|^2, \quad (2.5)$$

where  $\epsilon_0$  is the permittivity of free space, and  $|R^{nm}|^2$  refers to the transition probability between the upper level  $n$  and the lower level  $m$ . Natural line broadening is a type of homogenous broadening, since the atoms and molecules in the species behave the same way. This type of broadening exhibits a Lorentzian line shape – an example of which is shown in the following figure. <sup>(7)</sup>

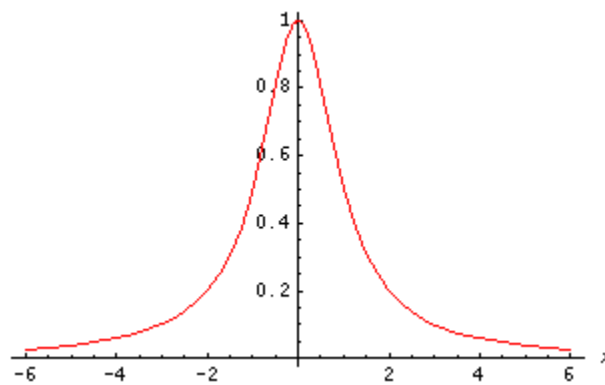


Figure 2.2 – A Lorentzian function.

Source: Weisstein, Eric W. "Lorentzian Function." From MathWorld--A Wolfram Web Resource. <http://mathworld.wolfram.com/LorentzianFunction.html> <sup>(8)</sup>

Doppler broadening, which occurs when the molecules of interest are moving with respect to the laser source, is another type of line broadening. Under the effects of Doppler broadening, the linewidth is characterized by the equation:

$$\Delta\nu = \frac{v}{c} \left( \frac{2kT \ln 2}{m} \right)^{1/2}, \quad (2.6)$$

where  $c$  is the speed of light,  $k$  is the Boltzmann constant, and  $m$  is the mass of the molecule in question. Doppler broadening is a type of inhomogeneous broadening, since the molecules in a sample behave differently. This type of broadening produces a Gaussian line shape, generally with a linewidth much larger than the natural case <sup>(7)</sup>.

Increased pressure in a sample gas causes an increase in molecular collisions. When molecules collide, the energy levels interact, thereby causing changes to the transition energies. As a result, the linewidth of the gas is enlarged. Although pressure broadening has a similar effect to Doppler broadening in terms of linewidth, in the pressure case, the lineshape remains Lorentzian <sup>(7)</sup>. For experimental conditions that are close to atmospheric pressure and ambient temperature, the contributions to the line shape of a gas from Doppler and natural broadening are dominated by collisional broadening <sup>(9)</sup>. As a result, in later derivations, the line shape of the target gas is assumed to be Lorentzian.

### 2.3 Spectroscopy Mechanics

There are three major types of atomic and molecular transitions that can cause absorption. Rotational transitions involve the axial rotation and rotational momentum of molecules. This type of transition requires comparatively low energy radiation. Incident radiation at higher energy can produce vibrational transitions, which involve the oscillation of the atoms within a molecule. Relatively powerful radiation can produce electronic transitions in an atom or

molecule, characterized by excitation of electrons between orbital shells. Figure 2.3 shows the general wavelength range needed to produce each type of transition.

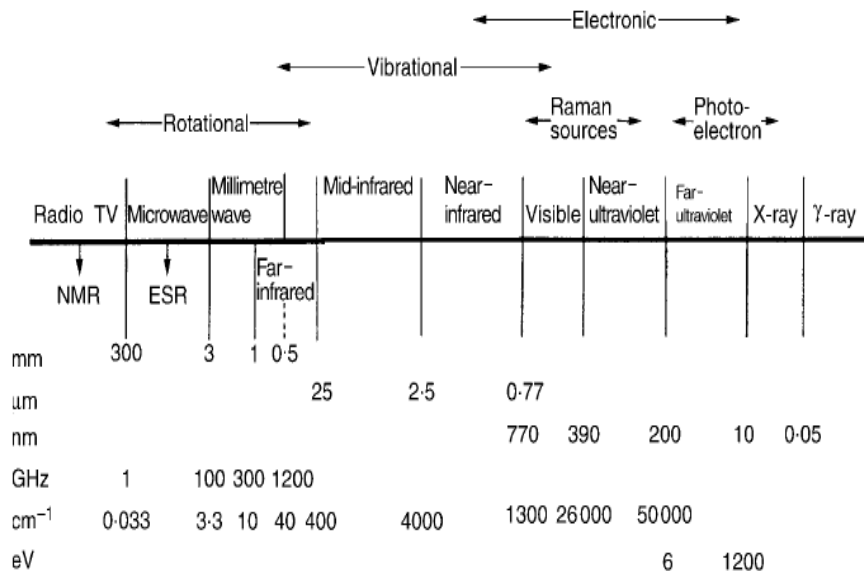


Figure 2.3 – The general wavelength range for each type of transition.  
Source: Hollas, Michael J. Modern Spectroscopy, 4<sup>th</sup> Edition. 2004, p 42.

Each transition is a subset of the previous type. As such, for each electronic state of a molecule, there is a series of vibrational levels, and for each vibrational level, there is a series of rotational energy levels. Figure 2.4 is a simplified illustration of the energy level subsets.

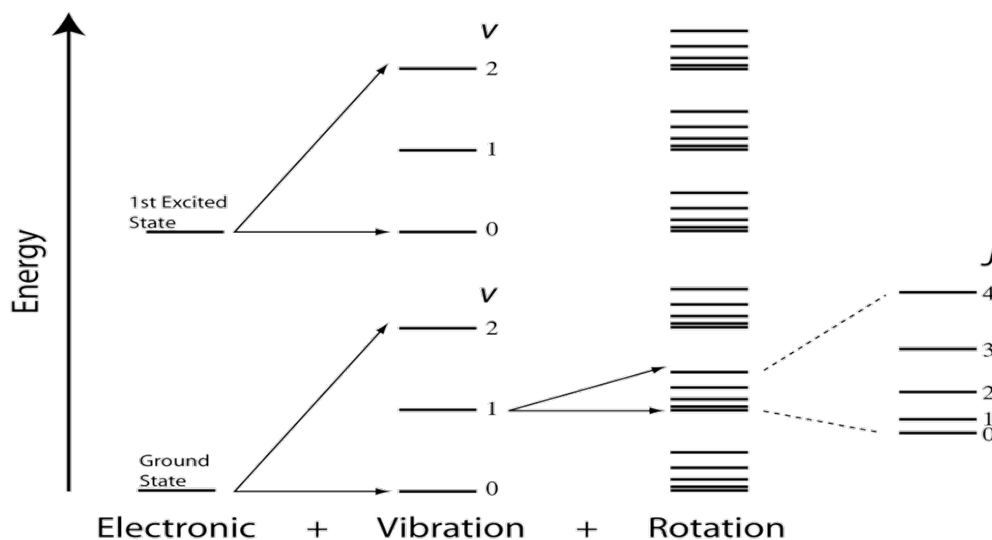


Figure 2.4 – Electronic, Vibrational and Rotational energy levels  
Source: Arnott, 2008, (10).

Although the energy levels of each molecule are unique, molecules of certain properties can be grouped into a set that follows the same transitional rules. These sets are called point groups, and they are defined based on the shape and symmetry of molecular species. For resolving the purely rotational energy levels, molecules can be further grouped by their characteristic moments of inertia. By modeling the molecule as a rigid body, the moment of inertia ( $I$ ) for a molecule about an axis is given by:

$$I = \sum m_i p_i^2, \quad (2.7)$$

where  $p_i$  is the perpendicular distance of the mass element  $m_i$  from the axis. When the moment of inertia is calculated for the various axes going through the centre of mass, a theorem of mechanics states that there are three mutually perpendicular axes for which the moment of inertia is either maximized or minimized. These axes are known as the principal axes, and the corresponding moments of inertia are called the principal moments of inertia. The relation between the principal axes of a molecule gives rise to several rotational groupings. Molecules for which the three principal moments of inertia are different are called asymmetric top rotors. If two of the principal moments of inertia are the same, the molecule is called a symmetric top rotor. Molecules in which all three principal moments are the same are known as spherical tops. Methane ( $\text{CH}_4$ ), which is the molecule of interest in this research, exhibits a tetrahedral molecular structure (belonging to point group  $T_d$ ), and is a spherical top rotor. The energy levels of rotation for a spherical top are given by the following formula:

$$\frac{E_r}{hc} = F(J) = BJ(J + 1) - DJ^2(J + 1)^2 + \dots, \quad (2.8)$$

where  $E_r$  is the rotational energy,  $h$  is Planck's constant, and  $c$  is the speed of light.  $F(J)$  is called the rotational term value, and  $J$  is the rotational quantum number (which takes integer values 0,1,2,...). The rotation constant  $B$  is related to the moment of inertia by:

$$B = \frac{h}{8\pi^2 cI}. \quad (2.9)$$

$D$  is known as the mean rotational constant, which is a series representing the influence of centrifugal forces. In the lower vibrational states,  $D$  is generally very small, meaning that the second order and higher order terms of  $F(J)$  can be neglected<sup>(11), (12)</sup>.

In a molecular species with  $N$  atoms, there are  $3N$  degrees of freedom. Of these freedoms, three are the well known translational freedoms belonging to the Cartesian coordinate system. Three more freedoms of motion are the associated rotational axes about the Cartesian vectors. This leaves  $3N-6$  vibrational modes. For example, in methane ( $\text{CH}_4$ ), there are  $3 \times 5 - 6 = 9$  vibrational modes in the ground electronic state. Classical mechanics can give us a surprisingly accurate first approximation for the vibrational frequencies of a molecule by considering the system as a superposition of  $3N$  simple harmonic oscillators in  $3N$  normal coordinates. In the classical solution, the atoms in a molecule are considered as masses joined by springs (which represent the restoring forces of the molecular bonds). This solution produces a system of  $3N$  linear equations which can be solved to find the fundamental vibration frequencies ( $\nu$ ) of the system. A similar solution is reached by solving the Schrödinger equation for a system of  $N$  particles. It is possible that the solution to the set of linear equations governing the vibrational motion will have one or more roots of multiplicity two or higher. These roots are said to be degenerate with one another. The vibrational states of a tetrahedral  $\text{XY}_4$  molecule are shown in Figure 2.5.<sup>(12), (13)</sup>

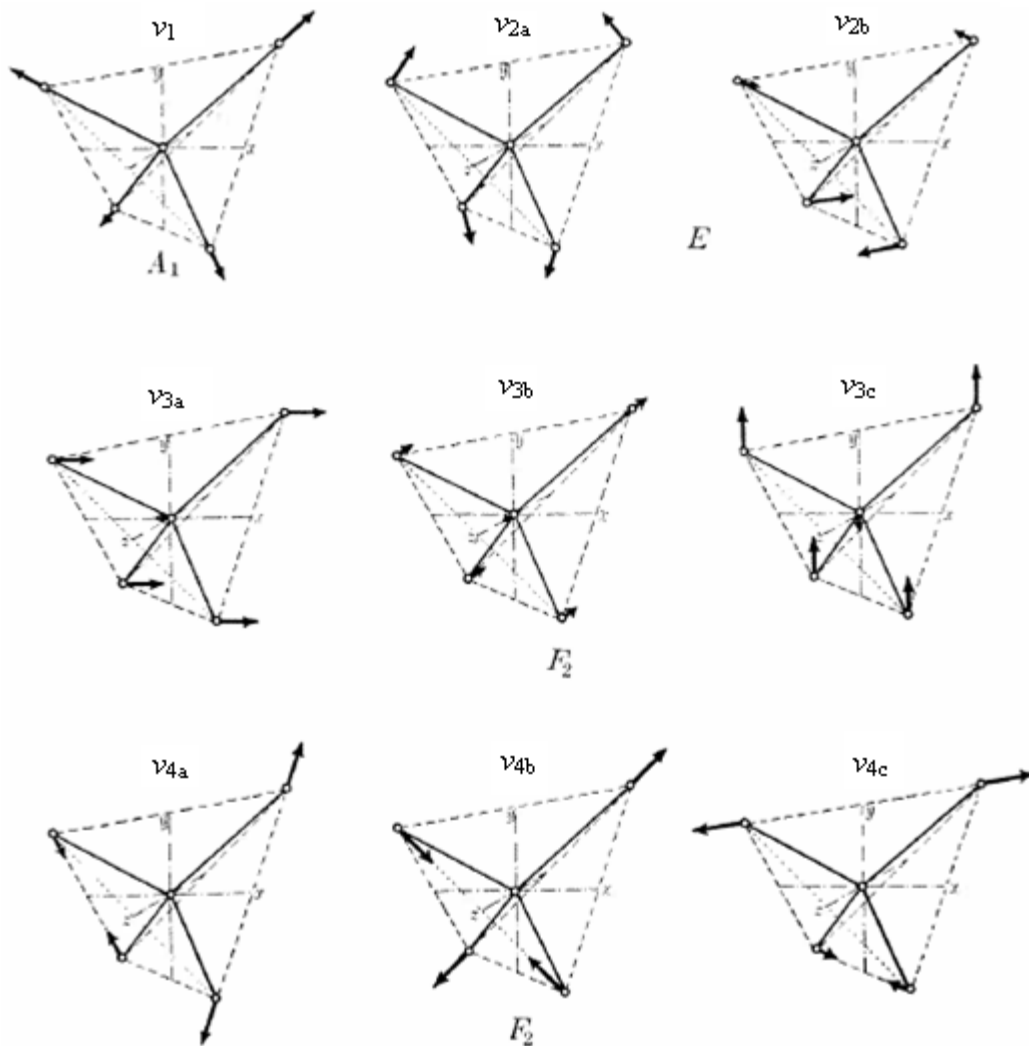


Figure 2.5 – Normal vibrations of a tetrahedral molecule.  
 Source: Herzberg, Infrared and Raman Spectra (1945), p. 100.

As illustrated in the figure, a tetrahedral molecule like methane has four fundamental vibrations. The first vibration,  $\nu_1$ , is a stretching mode of species  $A_1$  (which refers to the type and degree of symmetry of the vibration). The second fundamental vibration is a bending mode that is doubly degenerate, with  $E$  symmetry. Both  $\nu_3$  (stretching) and  $\nu_4$  (bending) are triply degenerate with  $F_2$  symmetry. The energy levels produced by harmonic oscillator  $i$  are given by the expression

$$E_i = h\nu_i \left( v_i + \frac{1}{2} \right), \quad v_i = 0, 1, 2, \dots \quad (2.10)$$

in which  $\nu_i$  is the classical oscillation frequency of the normal vibration  $i$  and  $v_i$  is the vibrational quantum number. Overtone vibrations can also exist, whereby the frequency of vibration is a harmonic of a fundamental vibration. Composite

vibrational states are also possible, in which two or more vibrational levels are excited, as well as sum and difference transitions. Although a number of combinations exist for each molecular species, whether or not a combination band may occur depends on the symmetry and types of fundamental vibrations. Group theory is used to derive which combination bands are allowed. <sup>(12)</sup>

Absorption and emission of molecular species due to vibrational effects are typically in the infrared region, however it is rare that a given infrared transition is purely vibrational in nature. Most vibrational transitions also involve a rotational transition. The characteristics of these so called ro-vibrational transitions are a function of the shape and symmetry of the molecule. Each molecular grouping has its own selection rules for allowed ro-vibrational transitions; for spherical top molecules, the selection rule is

$$\Delta J = 0, \pm 1 . \quad (2.11)$$

According to this rule, any allowable vibrational transition will also include a rotational transition where the change in the rotational quantum number is either zero, or plus or minus one. This selection rule generates a series of allowed transitions between vibrational levels, as shown in Figure 2.6.

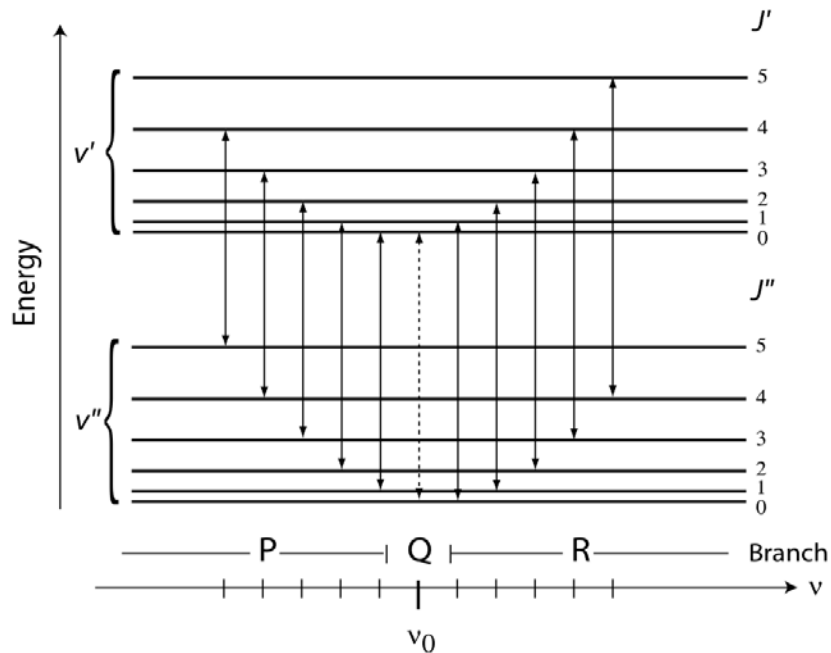


Figure 2.6 – Branches of ro-vibrational transitions.  
Source: Arnott, 2008. (10)

The different transitions are divided into three separate branches. For transitions in which  $\Delta J = 0$ , the set is known as the  $Q$  branch. Likewise, the set of transitions governed by  $\Delta J = J' - J'' = +1$ , is referred to as the  $R$  branch, while  $\Delta J = -1$  defines the  $P$  branch. The  $Q$  branch is denoted by a dotted line in the Figure 2.6 because it is a forbidden transition for some molecular groups. <sup>(12)</sup>

The energy levels for electronic, vibrational and rotational transitions shown in Figure 2.4 are complicated further by several effects. Firstly, the rigid rotor model of a molecule does not include the influence of nuclear spin. The individual spin of the various nuclei within a molecule can alter the symmetry of the molecular moment of inertia. When the effects of nuclear spin are included in rotational states, each rotational level  $J$  exhibits  $(2J+1)$  sub-levels of rotational energy. Additionally, since vibrating molecules are not truly simple harmonic oscillators, anharmonic effects (non-linear oscillation) tend to shift the energy levels of vibrational states. Lastly, when the motion of a particle is referred to a uniformly rotating coordinate system (which is used in the derivation of vibrational states), the effects of the centrifugal and Coriolis forces must be taken into account. These two forces account for the discrepancy between particle motion in an inertial reference frame and motion in a stationary frame. Although the effects of the centrifugal force are generally weak, the Coriolis force can cause a coupling between energy levels. In a molecule that is both rotating and vibrating in an arbitrary state  $\nu_a$ , the Coriolis forces on the molecules induced by the rotation can give rise to other vibrational motion. This means that several different vibrational species can exist in a molecule, even if only one fundamental vibration is excited. The coupling between rotational and vibrational states caused by Coriolis effects therefore greatly complicates the ro-vibrational energy levels of molecular species. In particular, Coriolis coupling causes degenerate vibrations to separate into distinct energy levels, as well as causing similar splitting between degenerate rotational sub-levels. The effects of Coriolis coupling become more pronounced if the frequency difference between

vibrational states is small. The ro-vibrational transitions of methane are strongly affected by Coriolis coupling since  $\nu_1$ ,  $\nu_3$  and the second overtone of  $\nu_2$  occur at nearly the same frequency. As a result, the overall band structure of methane is extremely complex, with thousands of possible transitions.<sup>(12), (14)</sup>

In this research, the emission wavelength of the laser is near 1650 nm ( $6060 \text{ cm}^{-1}$ ), which corresponds to the energy needed to excite methane from the ground vibrational state to the second overtone of the third fundamental vibration ( $2\nu_3$ ). Due to Coriolis effects, the  $2\nu_3$  vibration includes vibrational species of all fundamental symmetry types ( $A$ ,  $E$ ,  $F_2$ ). At the more precise wavelength of the absorption (1651.5 nm or  $6055 \text{ cm}^{-1}$ , refer to appendix), the transition is between  $J' = 5$  to  $J'' = 4$ , which corresponds to the fifth transition of the  $R$  branch ( $R(4)$  since  $R(0)$  is the first), as documented by HITRAN.<sup>(15)</sup>

## 2.4 Wavelength Modulation Spectroscopy (2f)

Wavelength modulation spectroscopy (WMS) is a popular method for trace gas detection, especially when using semiconductor lasers such as VCSELs. WMS is a technique that is best suited to lasers capable of a relatively wide tuning range, as well as flexibility to modulation; features that are intrinsic to semiconductor lasers. WMS relies on gently tuning laser emission wavelength through an absorption feature while also modulating the laser output at a higher frequency. The interaction of the modulated laser output with the absorption line creates harmonics of the modulation frequency. These harmonics can be accurately measured using lock-in detection and are directly proportional to the absorption feature. One major benefit of WMS is that it enables shifting the system to a higher operating frequency, thereby reducing the effect of  $1/f$  (thermal) laser noise<sup>(9)</sup>.

In semiconductor lasers such as VCSELs, modulation of the emitted light is achieved simply by modulation of the input injection current. This modulation

produces two effects: the changing current causes the frequency output of the laser to shift, producing frequency modulation (FM), however changes in the modulation current also produce changes in the overall laser output power, also called intensity modulation (IM). In nearly all WMS detection schemes, the signal of interest is the FM created by the absorption line. The intensity modulated signal, often known as residual amplitude modulation (RAM), is an undesired effect that reduces detection resolution <sup>(9)</sup>.

In general, the signal received at the detector is a product of both absorption and dispersion mechanics. Wavelength modulation, however, is low in frequency compared to the half width of the absorption line of interest ( $f \ll \Delta\nu_{\text{line}}$ ). In the experiments in this research, the modulation frequency is set at 10 kHz, while a gas at atmospheric pressure typically has an absorption half width of several gigahertz. Figure 2.7 shows the amplitudes of the first harmonic absorption and dispersion signals as a normalized function of  $x_m = f / \Delta\nu_{\text{line}}$ . From the figure, it is clear that when modulation frequencies

are of similar order to the absorption feature in frequency, both the absorption and dispersion contributions to the signal are significant. Once  $x_m$  decreases well below unity, it is clear that the contribution of the dispersion signal decreases far more rapidly than that of the absorption signal. One can conclude that it is valid to discount the effects of dispersion when modeling absorption profiles if  $x_m$  is sufficiently low. <sup>(9)</sup>

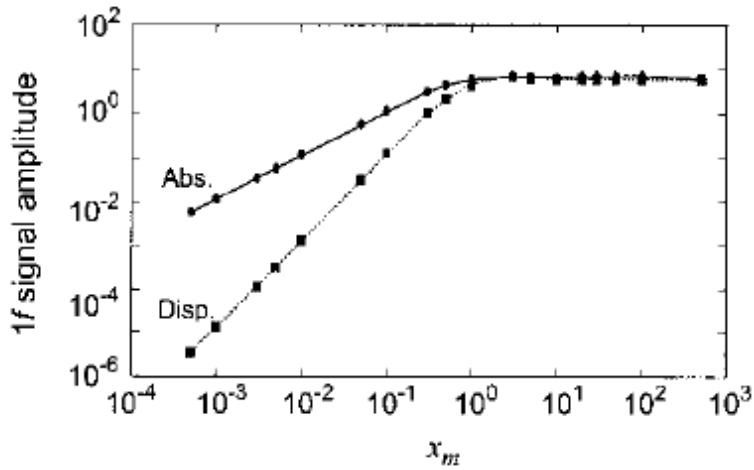


Figure 2.7 –  $1f$  absorption and dispersion signals versus normalized modulation frequency,  $x_m$ .

Source: Schilt. "Wavelength modulation spectroscopy: combined frequency and intensity laser modulation," *Applied Optics* **42**, p 6729.

The following material develops some of the mathematical equations which can be used to predict signal shapes in  $2f$  spectroscopy. In order to reduce the length and complexity, the derivations are not shown completely. The derivation is taken largely from the work of Arndt (1965) and Schilt (2003), for more information refer to these papers.<sup>(9)(16)</sup>

In a WMS system model that includes the contributions of intensity modulation (IM), the laser frequency can be modeled as:

$$\nu(t) = \nu_0 - \Delta\nu \cos(\omega t + \Psi), \quad (2.12)$$

where  $\nu_0$  is the laser frequency,  $\Delta\nu$  is its maximum variance,  $\omega$  is the modulation angular frequency, and  $\Psi$  is the phase shift between the IM and frequency modulation. In a VCSEL, this light characteristic is the result of an applied electrical current

$$i(t) = i_0 + \Delta i \cos(\omega t), \quad (2.13)$$

which also produces a corresponding modulation of light intensity  $I$  such that

$$I(t) = I_0 + \Delta I \cos(\omega t). \quad (2.14)$$

In a WMS system, there is also generally a low frequency ramp which slowly scans across the absorption profile of the target gas. Let the ramp angular

frequency be denoted by  $\Omega$ . Combining the effects of intensity modulation and frequency modulation yields

$$I_0(x) = I_0(p\Delta v_{line}x + 1), \quad (2.15)$$

where  $x$  is the laser frequency,  $I_0$  is the laser intensity at line center, and the slope coefficient  $p$  describes the laser power variation as a function of the optical frequency. At the receiver side of the system, the employment of lock-in detection tracks the incoming light at a specific harmonic of the modulation frequency  $nf$  ( $n = 1, 2, 3, \dots$ ). The general expression for transmitted light through an absorptive media, also known as the Beer-Lambert law, is given by:

$$t(x) = I_0 e^{-\alpha(x)}, \quad (2.16)$$

where  $\alpha$  is the absorption coefficient and  $x$  is the path length. If the amount of absorption is weak compared to the total light intensity ( $\alpha \ll 1$ ), equation 2.16 can be approximated as

$$t(x) = I_0[1 - \alpha(x)]. \quad (2.17)$$

By substituting equation 2.15 into 2.17, the expression becomes

$$t(x) = I_0(p\Delta v_{line}x + 1)[1 - \alpha(x)]. \quad (2.18)$$

The variable  $p$ , which relates to the laser power variation can be further subdivided into the component that stems from the laser modulation frequency,  $p_w$ , and the contribution to output power from the ramping signal,  $p_\Omega$ . By assuming that the absorbing gas of interest exhibits a Lorentzian line-shape, the detected signal is given as:

$$s_{IM-FM}(x) = I_0(p_\Omega \Delta v_{line} x_0 - p_\omega \Delta v_{line} m \cos(\omega t) + 1) \times \left\{ 1 - \frac{\alpha_0}{1 + [x_0 - m \cos(\omega t + \Psi)]^2} \right\} \quad (2.19)$$

where  $m$  is the modulation index of the FM signal. <sup>(16)</sup>

The equation for  $s_{IM-FM}$  can also be represented as a harmonic series as follows

$$s_{IM-FM}(x) = I_0 \left[ \sum_{n=0}^{\infty} s_{np}(x) \cos(n\omega t) - \sum_{n=0}^{\infty} s_{nq} \sin(n\omega t) \right], \quad (2.20)$$

where  $p$  and  $q$  refer to the in phase and quadrature coefficients respectively, and where:

$$\begin{aligned}
s_{np}(x) = & I_{\Omega}(x) \cos(n\Psi) s_n(x) - p_{\Omega} \Delta v_{line} \frac{m}{2} \left( \frac{\epsilon_n}{2} - \epsilon_n + 1 \right) \cos(n\Psi) s_{n+1}(x) \\
& - p_{\omega} \Delta v_{line} \frac{m}{2} \left\{ \left( \frac{2}{\epsilon_{n-1}} \right) \cos[(n-1)\Psi] s_{n-1}(x) \right. \\
& \left. + (\epsilon_n - 1) \cos[(n+1)\Psi] s_{n+1}(x) \right\} \quad (2.21)
\end{aligned}$$

$$\begin{aligned}
s_{nq}(x) = & I_{\Omega}(x) \sin(n\Psi) s_n(x) - p_{\Omega} \Delta v_{line} \frac{m}{2} \left( \frac{\epsilon_n}{2} - \epsilon_n + 1 \right) \sin(n\Psi) s_{n+1}(x) \\
& - p_{\omega} \Delta v_{line} \frac{m}{2} \left\{ \left( \frac{2}{\epsilon_{n-1}} \right) \sin[(n-1)\Psi] s_{n-1}(x) \right. \\
& \left. + (\epsilon_n - 1) \sin[(n+1)\Psi] s_{n+1}(x) \right\} \quad (2.22)
\end{aligned}$$

and

$$I_{\Omega}(x) = p_{\Omega} \Delta v_{line} x + 1. \quad (2.23)$$

In the above expressions, the function  $s_n$  is described by the equation:

$$s_n(x) = I_0 \left( J_n(0) - \frac{\alpha_0}{2} \left\{ (-j)^n \epsilon_n \frac{[\sqrt{(1-jx)^2 + m^2} - (1-jx)]^n}{m^n \sqrt{(1-jx)^2 + m^2}} + c.c. \right\} \right) \quad (2.24)$$

where c.c. refers to the complex conjugate of the previous term,  $j$  is the complex number,  $\alpha_0$  is the absorption coefficient at line center,  $\epsilon$  is a function such that  $\epsilon_0=1$ ,  $\epsilon_n=2$  for  $n \geq 1$ , and  $J_n$  is the  $n^{\text{th}}$  order Bessel function.

In order to best make sense of the meaning of these equations, it is valuable to consider a special modulation case, in which “pure” frequency modulation is used. Under these circumstances, intensity modulation is discounted, meaning that  $p_{\omega} = p_{\Omega} = 0$  and  $I_{\Omega} = 1$ , thereby yielding  $s_{np}(x) = \cos(n\Psi) s_n(x)$  and  $s_{nq}(x) = \sin(n\Psi) s_n(x)$ . Consequently, the first three harmonics of  $s_{IM-FM}$  reduce to:

$$\begin{cases} s_{1p}(x) = I_{\Omega}(x) \cos(\Psi) s_1(x) - p_{\omega} \Delta v_{line} \frac{m}{2} [2s_0(x) + \cos(2\Psi) s_2(x)] \\ s_{1q}(x) = I_{\Omega}(x) \sin(\Psi) s_1(x) - p_{\omega} \Delta v_{line} \frac{m}{2} [\sin(2\Psi) s_2(x)] \end{cases} \quad (2.25)$$

$$\begin{cases} s_{2p}(x) = I_{\Omega}(x) \cos(2\Psi) s_2(x) - p_{\omega} \Delta v_{line} \frac{m}{2} [\cos(\Psi) s_1(x) + \cos(3\Psi) s_3(x)] \\ s_{2q}(x) = I_{\Omega}(x) \sin(2\Psi) s_2(x) - p_{\omega} \Delta v_{line} \frac{m}{2} [\sin(\Psi) s_1(x) + \sin(3\Psi) s_3(x)] \end{cases} \quad (2.26)$$

$$\begin{cases} s_{3p}(x) = I_{\Omega}(x) \cos(3\Psi) s_3(x) - p_{\omega} \Delta v_{line} \frac{m}{2} [\cos(2\Psi) s_2(x) + \cos(4\Psi) s_4(x)] \\ s_{3q}(x) = I_{\Omega}(x) \sin(3\Psi) s_3(x) - p_{\omega} \Delta v_{line} \frac{m}{2} [\sin(2\Psi) s_2(x) + \sin(4\Psi) s_4(x)] \end{cases} \quad (2.27)$$

Under the conditions of pure frequency modulation (discounting intensity modulation effects), the received signal at the  $n$ th harmonic is proportional to the  $n$ th derivative of the line-shape function. This somewhat simplified case produces WMS signals that correspond to the various derivatives of  $t(x)$  in equation (2.18). Since equation (2.18) refers to a Lorentzian line, the WMS signals produced at the various harmonics directly correspond to the successive derivatives of a Lorentzian profile (shown in Figure 2.2 previously).<sup>(9)</sup> Figure 2.8 gives an illustration of the shape of WMS signals using pure FM.

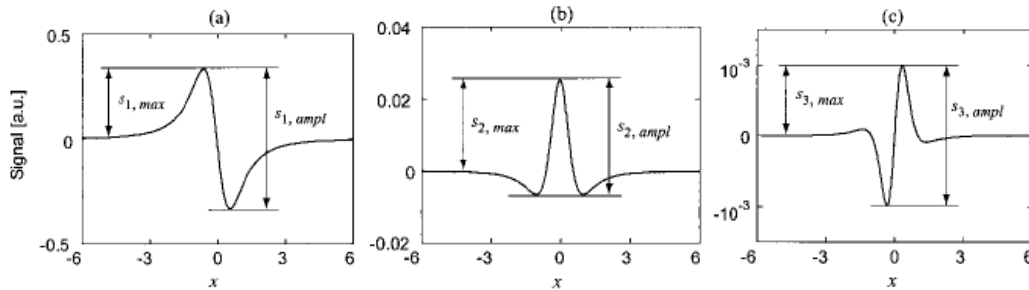


Figure 2.8 – Theoretical WMS signals at the first 3 harmonics of the Lorentzian line-shape (pure FM,  $m = 0.1$ ). The maximum signal and amplitude are shown on each.

Source: Schilt. “Wavelength modulation spectroscopy: combined frequency and intensity laser modulation,” Applied Optics **42**, p 6731.

The more general case which considers the effects of intensity modulation in WMS signals is somewhat more complicated. In systems where the modulation index is small ( $m \ll 1$ ), the derivative relationship between the absorption line and the signal holds true, however at higher modulation indices, distortion occurs. The maximum ( $s_{n,max}$ ) and amplitude ( $s_{n,amp}$ ) shown in Figure 2.8 are a function of the modulation index. For each harmonic, there is a modulation index which maximizes either  $s_{n,max}$  or  $s_{n,amp}$ . In the frequency modulation case with little to no IM, the optimal modulation index for maximum signal,  $m_{n,max}$ , for the first three harmonics are 2.00, 2.20, and 3.59. Similarly, the index which provides maximum amplitude,  $m_{n,amp}$ , are 2.00, 3.09, and 3.59.<sup>(9)</sup> The introduction of intensity modulation tends to alter the maximizing indices, and in some cases produces more than one optimal index (or at least locally optimal). From Figure 2.8, it can be noted that all of the first three harmonics exhibit even or odd symmetry. The distortion of WMS signals caused by IM generally lead to asymmetric results, as well as a DC offset in the case of the first

harmonic. Figure 2.9 compares the pure FM and FM-IM cases in several different manners. <sup>(9)</sup>

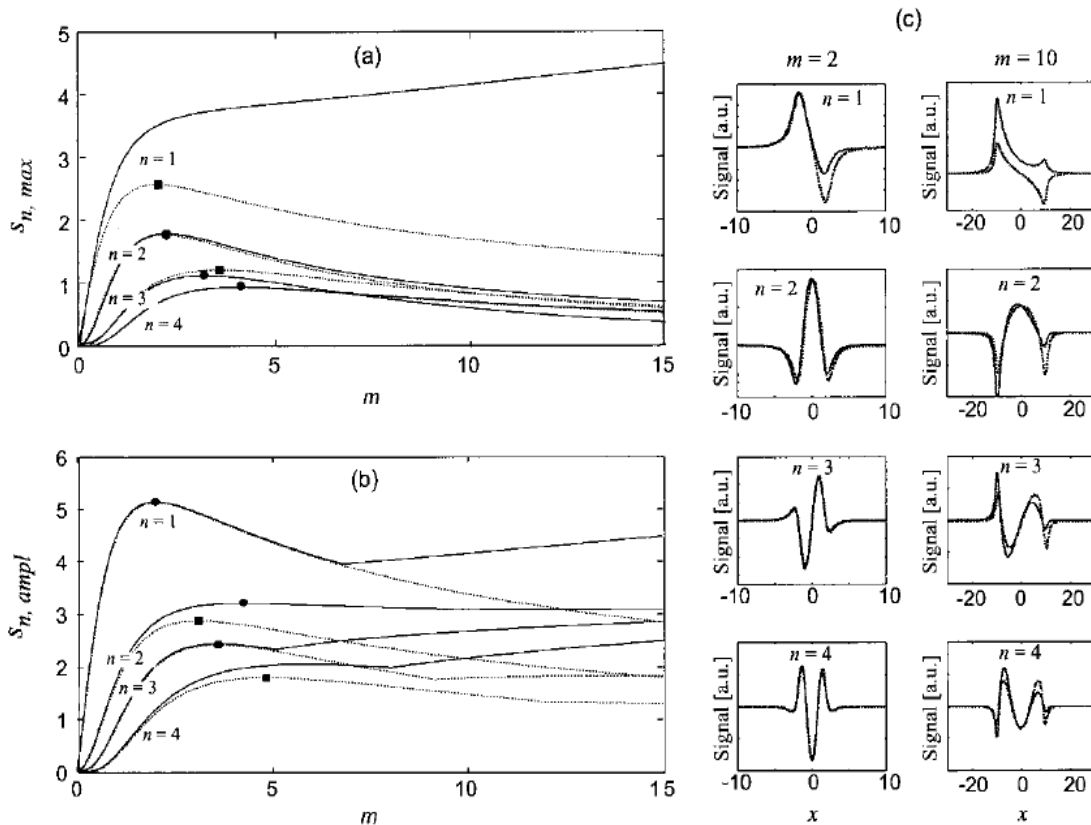


Figure 2.9 – Signal versus modulation index in (a) the maximum case, and (b) the amplitude case. Solid lines are FM-IM with  $p_{\Omega} = -1$  ( $1/\text{cm}^{-1}$ ) and  $p_{\omega} = -2$  ( $1/\text{cm}^{-1}$ ) and  $\Psi = -90$  degrees, while the dotted lines are the pure FM case. Where applicable, the optimal values for  $m$  are indicated. (c) Shows the corresponding WMS signals at  $m = 2$  and  $m = 10$ .

Source: Schilt. "Wavelength modulation spectroscopy: combined frequency and intensity laser modulation," Applied Optics **42**, p 6732.

The mathematical analysis of WMS signals produces several important results. Firstly, it is clear that, when modulated properly, the resultant waveforms correspond to the derivative of the absorption line of the scanned gas. This is a valuable result, especially since, in many cases, the direct absorption feature of a gas is extremely small. However, since absorption features occur at a high frequency, the corresponding derivative signal is often significantly larger than the original, allowing for superior resolution. Figure 2.9 indicates that best WMS signal amplitudes are given by relatively large indices ( $m \geq 1$ ), an area where IM distortion can alter the derivative characteristics of the signal. The first harmonic in particular is highly distorted at high indices, as well as offset from zero. The

second harmonic signal, however, maintains a zero offset, and remains very close to the ideal FM form despite IM distortion. The higher orders provide even better performance at high indices, however, they are generally more difficult to implement. Fortunately, the second harmonic WMS signal is very close to ideal at the maximal indices (in the range 2.0-3.09). For these reasons, second harmonic detection is a very powerful method for resolving a gas which exhibits a Lorentzian line-shape.

## 2.5 VCSEL Fundamentals

A vertical cavity surface emitting laser (VCSEL) is a type of semiconductor laser. As such, VCSELs use electrical current as their pumping source, and diode-like structure as the basis for emission. Unlike other types of semiconductor lasers, which usually emit edgewise out of the semiconductor wafer, VCSELs emit vertically. A VCSEL is structured as a vertical resonator; a p-n junction, often employing the use of quantum wells, forms the active region, while thin layers on top and bottom of the active region form the distributed Bragg reflectors (DBR) which act as the resonator ‘mirrors’. An illustration of a VCSEL model is shown in Figure 2.10.

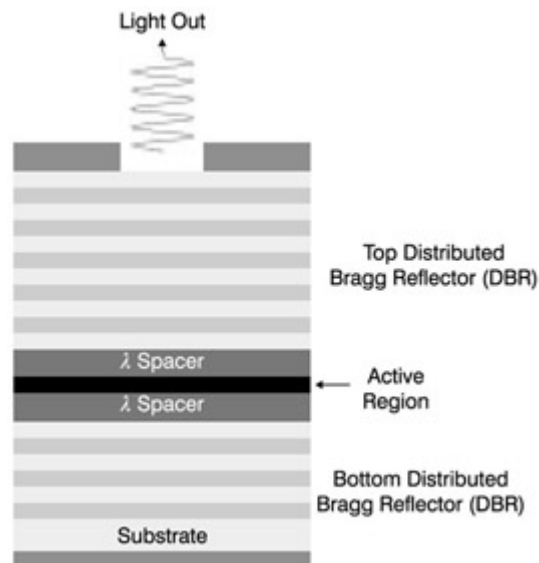


Figure 2.10 – Basic VCSEL Structure

Source: Fiber Optic Reference Guide: A practical Guide to Communications Technology, Third Edition, 2002, Chapter 5.  
(17)

The distributed Bragg reflectors are crucial to accurate VCSEL operation. Each DBR layer is composed of alternating semiconductor layers with slightly varying indices of refraction spaced at very precise intervals. At each interface layer in the DBR, part of the emission from the active region is reflected, and part of the emission continues to propagate. The indices and spacing of the DBR layering is carefully calculated to ensure that, in a very narrow band of frequencies, the reflected contributions from each interface constructively interfere (they are in phase). One of the reasons that VCSELs have advanced so rapidly in the past few years is that more accurate manufacturing techniques have become available. As a result, DBR layers can be constructed with incredible accuracy and reflectivity, leading to extremely narrow emission frequency bands, better efficiency, and a desirable beam shape (TEM<sub>00</sub>).<sup>(18)</sup>

In semiconductor lasers, the stimulated emissions of the active region are caused by carriers (either electrons or holes) transitioning between the valence band and the conduction band of the semiconductor. In general, a uniform p-n junction structure in the active region has a large number of allowable transitions between the valence and conduction bands. The distribution of transitional probabilities between these bands is known as the density of states. A quantum well can be introduced into the p-n junction by adding a small region, with a size comparable to the de Broglie wavelength of the carriers (typically 10-50nm), of another semiconductor type. If the transitional energy material used to form the quantum well is lower than the transitional energy of the surrounding material, the density of states in the region will be greatly confined. In a normal semiconductor, the density of states is a continuously increasing function; in a region influenced by a quantum well, the density of states becomes a step function. Each transition between the conduction and valence band has an associated energy, and thereby, an associated emission wavelength. By confining the density of states to a step function, a great deal of the transitions occur at the same wavelength. Essentially, this means that quantum wells significantly narrow

the frequency emission of the laser. Quantum wells also produce the additional desired effect of reduced threshold energies.<sup>(18)</sup>

VCSELs are rapidly increasing in popularity and functionality due to a number of reasons. The advent of incredibly precise semiconductor fabrication techniques has allowed for the introduction of nearly ideal DBR resonators, as well as quantum wells. As a result, VCSELs exhibit excellent beam characteristics for a number of applications; narrow emission linewidth, very low power consumption, low threshold currents and wide tuning ranges. These properties make VCSELs highly attractive for spectroscopy applications, especially when cost, power consumption and size are also major factors. Figure 2.11 is a picture of a TO package VCSEL, similar to the one used in the following chapters.

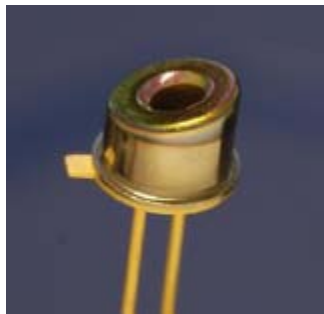


Figure 2.11 – A TO-46 Packaged VCSEL  
(Source: Vertilas)

## 2.6 Literature Review

In order to achieve a thorough understanding of the design goals and challenges presented in this research, it is valuable to consider the results of similar research and experiments. Evaluation of related efforts in the field of laser spectroscopy is also a useful as a basis for comparison for the quality of the designed system and results. Tunable diode laser spectroscopy (TDLAS) is a reasonably mature field, however, portable applications, and the use of VCSELs for TDLAS is still an area of intense research.

Several portable spectroscopy devices based on distributed feedback lasers and standard edge emitting diode lasers have already been developed; a few of these systems are even available as consumer products. R. T. Wainner et al. (2002) describe the construction of a handheld, battery powered methane spectroscopy system based on a tunable diode laser of 1.65 micron wavelength. The system (shown in Figure 2.12) can be operated in direct absorption, frequency modulation, or balanced detection. The transceiver and battery pack weigh about 1.5 kg each, with a total power dissipation of about 1.5 W.

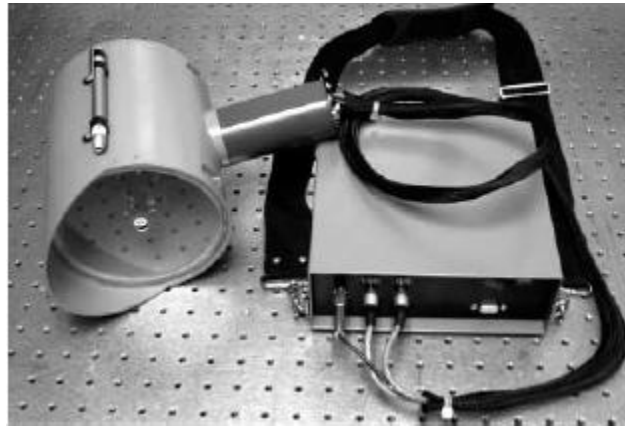


Figure 2.12 – Portable spectroscopy system

Source: Handheld, battery-powered near-IR TDL sensor for stand-off detection of gas and vapor plumes, Applied Physics B, page 250, 2002.

Optical collection occurs in the transceiver, and relies solely on open path backscatter (no external optics are needed). The system uses on-board digital signal processing (DSP) for signal analysis. The system demonstrated an experimental accuracy of  $(2-4) \times 10^{-4}$  (referring absorption peak magnitude to modulation signal of the laser) over open path lengths of 1 to 30 m. For methane gas, this absorbance sensitivity corresponds to a minimum detectable concentration of about 12 ppm·m<sup>(19)</sup>.

T. Iseki (2004) demonstrated a portable methane sensor based on laser spectroscopy accurate and small enough to become a commercial product. The device uses a InGaAsP distributed feedback laser (DFB) as the spectroscopy radiation source, and 2<sup>nd</sup> harmonic wavelength modulation as the detection method. The laser wavelength is 1.65372  $\mu\text{m}$ , centered on a methane absorption

line. The system operates from a nickel metal hydride (NiMH) battery, which weighs 1.3 kg and generates an output of 5-10 mW. Laboratory results for this system using a 5 m path length with concrete as the background and a 10 cm absorption cell as the target showed a relative sensitivity of  $9.9 \times 10^{-5}$  (corresponding to about 1.3 ppm·m for methane gas). Open path length results demonstrated a range of up to 10 m, with a noise level below 5 ppm. Figure 2.13 is a photograph of the system developed by Iseki<sup>(20)</sup>.



Figure 2.13 – A portable remote methane detector based on a DFB laser.  
Source: (Iseki, 2004)

VCSELs are a fairly new player in the field of spectroscopy, but show promising results and excellent practical qualities (low cost, extreme large tuning range). To the author's best knowledge, a portable spectroscopy system based on VCSEL technology has not been demonstrated, however, a large body of work surrounding lab and bench-top technology has been generated by many researchers.

M. Lackner et al. (2003) used a VCSEL emitting at  $1.68 \mu\text{m}$  to detect methane in a lab environment. Although the authors were only attempting to prove the concept and did not report sensitivity findings, they achieved repetition rates up to 5 MHz, and at pressures ranging from 10 mbar to 1.3 bar. A combination of direct scanning using a triangular wave, and temperature scanning was employed as the method for tuning the laser through a 44 cm gas cell.<sup>(21)</sup>

VCSEL systems near 1.55  $\mu\text{m}$  have also been used to detect gases such as carbon dioxide, carbon monoxide and ammonia <sup>(22), (23)</sup>. Again, these studies demonstrated excellent resolution of spectral lineshapes when compared to the HITRAN database, but did not report on minimum detectable limits.

Clearly there is more research needed to determine whether or not VCSELs can compete with normal diode lasers for sensitivity, open path and outdoor applications, and cost considerations. The research presented in this thesis deals with these issues, and as far as the author knows, reports the first sensitivity findings for VCSEL spectroscopy of methane gas.

## Chapter 3: System Design

This section is dedicated to describing the design of the spectroscopy system and experimental conditions used in this research. With the exception of the oscilloscope, the entire experimental equipment is powered by two sets of heavy duty 12V batteries, supplying +/- 12V. The oscilloscopes, while capable of battery operation, are typically operated from an AC line. The VCSEL is mounted in the TCLDM9 housing and fixed to an optical table. One battery pack is positioned nearby, and after passing through a 5V regular, powers the laser driver and modulation circuitry. The laser output is directed along the optical table, and usually through a gas cell before reaching the photodetector. The output of the detector is then applied to the either the PLL or external reference receiver and monitored with an oscilloscope. Figure 3.1 is a diagram of the lab set up. More detail on each of the important features of the system is given in the following sections.

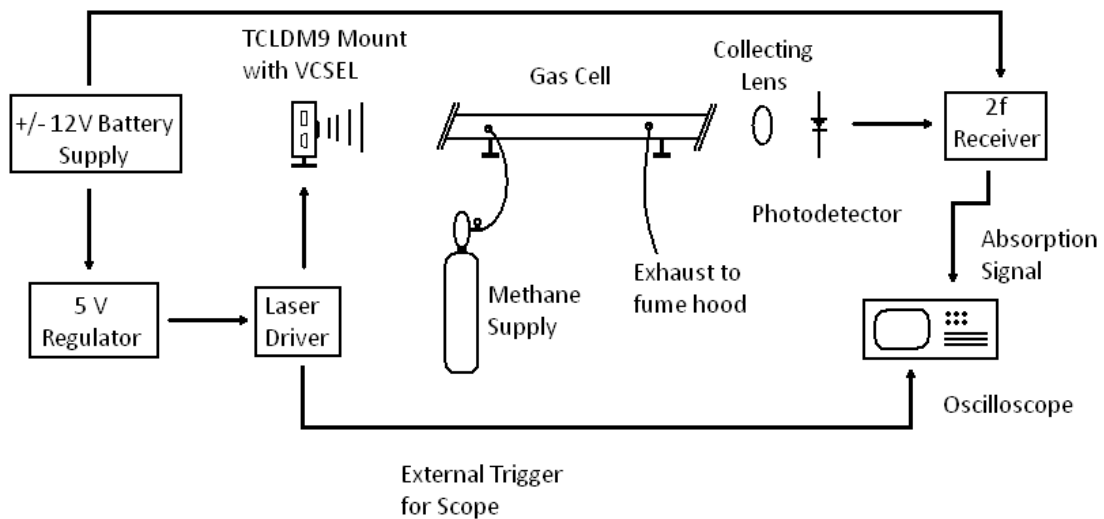


Figure 3.1 – Experimental VCSEL system

### 3.1 The Driver Board

The entire design of the VCSEL system is very important to generating solid results, as well as moving towards portability. The VCSEL itself used for the system construction is a VL-1654-4-SP-A-T4 supplied by Vertilas. The

wavelength of the VCSEL is 1654 nm, chosen for its proximity to a strong methane absorption line. The laser is incredibly diminutive in both power requirements and physical dimensions. The bias current needed for CW operation is around 0.4 mA, while it is about 5mm in diameter, and 3 cm long (including pins; excluding pins the housing is only about 5mm long). [refer to appendix for detailed specifications]. The size and power advantages of the laser are somewhat tempered by the need for an accurate way to control the laser temperature. As such, the VCSEL is mounted in a TCLDM9 housing from Thor Labs. This mount increases the dimensions of the laser head to 8.89cm x 8.89cm x 5.03cm, and has a weight of 590g. It is easily possible to reduce the size of this apparatus with a custom temperature control design, however that was not covered in the scope of this project.

The driving system for the laser is one of the most important components of the system. The driver was chosen and modified in order to meet very exacting standards. Firstly, it must supply current to the laser in a very precise manner, with very little long term fluctuation or noise. Furthermore, the driver must provide protection against overloading the laser, since CW currents as low as 5mA and up can cause damage to a VCSEL. The driver must be capable of controlling the temperature of the housing with considerable accuracy, as well as supplying both a low and high frequency modulation. The driver system has been through several iterations, but the system currently in use consists of the following: a Thor Labs VITC 002 VCSEL driver board, an external circuit to supply high frequency modulation, another external circuit to generate low frequency ramping, and associated power supplies.

One major goal of the system design was to realize battery operation. Obviously, battery power is desirable for portability, but it also generally has the added benefit of significantly reduced noise due to the absence of 60Hz harmonics. The batteries used for the majority of experiments were two large, heavy duty batteries wired to give a +12 and -12V DC output. The battery unit

used in the lab weighs at least 20 pounds, clearly much heavier than desired for portability. However the main reason for using such powerful batteries was to allow for very long periods of operation without needing to recharge. Much smaller batteries could be employed and still easily achieve several hours of continuous operation. The 12V batteries are regulated to 5V with a DC-DC converter, since both the Thor Labs board and high frequency modulation board operate on 5V supplies. A 12V supply signal is taken directly from the battery to power the triangular modulation board.

The VITC 002 board is an extremely useful device in the operation of VCSELs. This board is specially designed for VCSELs, and as a result is capable of maintaining very accurate currents at very low levels. In order to better explain the operation of the laser driver as a whole, as well as the procedures used to test laser operative states, it is useful to explain a significant amount about the VITC 002 board.

Important features of the VITC 002 board:

- Capable of adjustable safety limit on both DC and modulating waveforms. The board will hard limit any waveforms exceeding the user specified limit current. Transient waveforms partially exceeding the limit are simply clipped. This is a very important feature for safe operation of the laser.
- Built to generate either a CW output current or a highly adjustable triangular wave modulation. The range of modulation frequencies varies between 1-100Hz and 100-10kHz.
- Has 2 external inputs for outside modulation sources. More importantly, these inputs have on-board voltage to current amplifiers, meaning that precisely controlled voltages inputs are converted to current when driving the laser. This is valuable because voltage modulation signals are generally easier to design and build than current driven signals.
- Has a temperature control device designed to integrate with the TCLDM9.

-Generates many control output signals to allow for the precise monitoring of the laser operation conditions. These signals include both the set current and actual current through the laser, the set resistance of the thermistor and actual resistance of the thermistor (used for controlling the temperature), as well as temperature window and error monitoring.

There are three major ways of operating the VCSEL for spectroscopy, as discussed earlier. The first is simply to apply a current ramp along with a DC bias through the laser; strong absorption signals will cause a slight dip in the ramp as the laser wavelength sweeps through the absorption line. This 'direct' absorption technique, while simple, is generally not powerful enough to detect trace levels of gases. The method employed in of these experiments is  $2f$  absorption. As mentioned earlier,  $2f$  absorption uses high frequency modulation in addition to wavelength scanning to generate a derivate signal based on the actual absorption. In addition to the high frequency modulation, the laser must be properly biased into CW operation using a DC current, as well as swept through the absorption region either using a temperature shift or a current ramp. Although both methods were used fairly extensively, ramping signals are generally superior to temperature. This is because ramp based scans are significantly faster than temperature scans, allowing for quicker results and more flexibility to average individual scans.

The method of choice for  $2f$  spectroscopy using the VCSEL is current scanning using a ramped waveform, while maintaining constant temperature using the TEC. The reader is reminded that the VITC 002 is capable of generating triangular waveforms at low enough frequencies for current scanning. Triangular modulation, however, is not as desirable as ramp waveforms, since symmetric waveforms tend to generate an absorption signal twice per cycle. The up-scan and down-scan absorptions cause by triangular absorption tend to be slightly different, and therefore make averaging more difficult. As a result, the use of the VITC 002 for current generation is generally limited to only the bias current.

Both the high frequency sinusoidal wave, as well as the low frequency current ramp must thusly be supplied by external circuitry. We recall that the VITC 002 board has two external modulation inputs, governed by the equation,

$$I_{LD} = I_{SET (Board)} + I_{CON 2} + I_{CON 3} \quad (3.1)$$

where  $I_{CON}$  refers to the two external inputs on the board. (Con2 and Con3 are the actual names given to the ports by the VITC 002 manual). The input amplifiers connected to the con ports are specifically designed according to the following characteristic:  $I_{Input} = V_{CON} \times 1\text{mA}/100\text{mV}$ . For example, an input voltage of 1V applied to the Con ports will generate 10mA of current in the laser diode. This input characteristic made the design of external modulation systems extremely easy.

### 3.2 High Frequency Modulation

The operation of the high frequency circuit is critical to successful spectroscopy using  $2f$  methods. The frequency must be chosen such that it is significantly higher than the ramp frequency to avoid harmonic interference. VCSELs are capable of extraordinarily high operation frequencies, even into the gigahertz range, but the practical limitations of electronics must also be considered. We chose 10 kHz for the modulation frequency – this range is high enough to be well removed from ramp frequencies in the 50-300Hz range, as well as sufficiently low to make electronic designs fairly simple. WMS spectroscopy requires very stable modulation signals for accurate results and low noise. The modulation signal must be kept as close to fundamental as possible, since stray 2<sup>nd</sup> harmonic components in the output translate to a DC offset on the receiving end. For these reasons, a crystal oscillator is used as the source for the high frequency modulation. The oscillator is based around a 40.00 kHz crystal. The main reason for using a 40 kHz crystal is availability, but the necessity of frequency division to achieve 10 kHz also serves to buffer the oscillator, thereby increasing circuit stability. The crystal oscillator and subsequent frequency divider network generate a 10 kHz square wave, which is then filtered into a sine wave with a

high-Q 10 kHz bandpass filter. Finally the output is applied to the VITC board through an adjustable voltage divider network. The block diagram of the modulation frequency circuit is show in Figure 3.2.

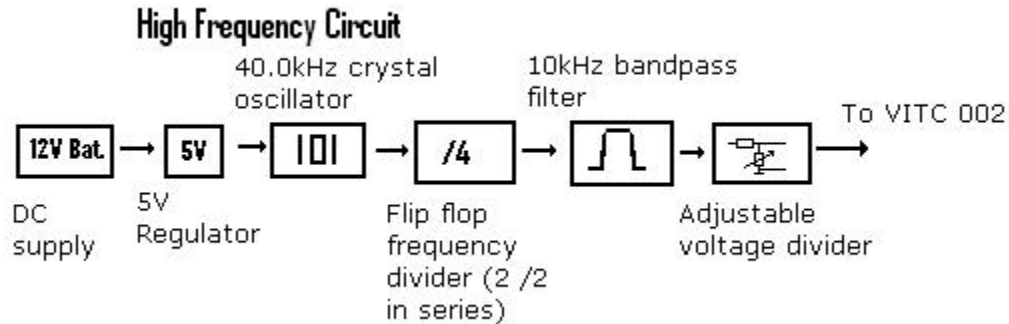


Figure 3.2 – Block diagram of the high frequency modulation circuit

### 3.3 Design of the Ramp Generator

The ramp generator is the second external input to VITC 002 driver board. The circuit was built by lab technician Alan Lim, and is designed to supply a highly controllable ramp to the driving circuitry. This particular design is a common ramp oscillator circuit, with several potentiometers giving adjustable controls for ramp frequency, ramp duty cycle and ramp amplitude. In particular, the duty cycle control (in this case the balance between ramping up and down) is important since very sharp downramps can cause unwanted spiking behaviour that persists through the detection circuitry. By adjusting the duty cycle to 0.9T ramp up, and 0.1T ramp down, the high frequency spikes can be greatly reduced. The ramp generator also generates a sync output, which is used to trigger the oscilloscope at the receiving end of the circuit, allowing for more accurate detection.

### 3.4 Receiving and Data Processing Systems

One major goal of this work was to compare and contrast the different possible methods for signal reception and processing in  $2f$  spectroscopy. My work focused on the viability of analog circuitry for detection, and how it compares digital systems (the digital detection methods were investigated

simultaneously by some of my colleagues in Dr. Tulip's lab group). It is of particular interest to know how much, if any, signal to noise ratio is lost by analog to digital conversion when using digital systems. Are analog systems still necessary for measurements at extremely low concentrations? Two different analog detection schemes have been designed and built, one using a phase locked loop (PLL) to generate a reference signal, the other employing an external reference from the driver. Both systems function impressively in 2<sup>nd</sup> harmonic detection, however each has its own advantages and disadvantages, discussed in chapter 4.

### **3.4.1 Photodiode and Front End Amplifier**

The photodetector at the receiver is a TO packaged photodiode, model number ETX 1000T, made by JDSU. The detector has its peak sensitivity in the near-IR range around 1500 nm, and is well matched with the VCSEL emission wavelength. The photodiode also exhibits low dark current while maintaining a relatively large active region (1 mm diameter); both desirable traits for accurate detection.

Two different types of front end amplifier have been tested, a transimpedance amplifier, and a more typical voltage amplifier. The transimpedance configuration is capable of extremely high gains, but is not as linear as a voltage amplifier, nor as controllable. Generally speaking, the voltage amplifier was capable of enough amplification for this application, and as a result it was the configuration of choice for the system. The photodiode and front end voltage amplifier are both packaged together in a metal case, and the circuitry uses low noise components to improve the accuracy of the detection system.

### **3.4.2 Phase Locked Loop Detection System**

Although discussed earlier, a lot of the theory in  $2f$  spectroscopy is highly relevant to the design of the detection system; therefore some parts may be repeated. The received waveform at the photodiode is usually very similar to the

modulating waveforms supplied by the driver. The waveform consists of a DC bias, slowly ramping laser power which causes the laser to sweep a range of wavelengths, and the high frequency sinusoidal modulation. In the presence of an absorptive gas, in this case usually methane, variations to both ramp characteristic and the harmonic components of high frequency modulation are altered according to the lineshape of the gas. Owing to the theory of  $2f$  spectroscopy, the second harmonic of the high frequency modulation is related to the derivative of the absorption line of the gas. As such, the goal of the detection system is to isolate the second harmonic frequency, 20 kHz, with the greatest degree of accuracy.

The first step towards honing in on the 20 kHz signal is to remove the signals that are unnecessary in the process. The DC bias and low frequency ramp can be largely removed by AC coupling of the photodiode's front end amplifier. A second AC amplifier is used on the front end of the phase locked loop (PLL) receiver to ensure the modulation signal strength is adequate. This gain could be realized in one stage, but in the interests of op amp bandwidth, two stages are desirable.

The procedure used to isolate the 20 kHz signal is to mix it with an in-phase reference signal at the same frequency. The mixing then produces signals in the DC band and at 40 kHz. By filtering out the high frequency components, only the DC band remains. The signal in the DC band represents the variance in 2<sup>nd</sup> harmonic component over the period of the ramp; if the laser crosses a methane absorption line during that period, the DC band transcribes a plot of the derivative of the methane absorption line.

The PLL is what allows for the generation of the in-phase reference signal. The input 10 kHz waveform is first applied to a 10 kHz bandpass filter, then input to the phase reference of the PLL. The voltage controlled oscillator (VCO) of the PLL is set to run at 20 kHz. One part of the VCO is output to the mixer, while the other is divided back to 10 kHz and applied to the other phase reference. While the circuit seems complicated, the operation is fairly simple. As long as the input

to the PLL from the photodiode is near 10 kHz with signal amplitude  $>0.2V$  (ref needed), the divided frequency of the VCO will track the phase of the input. The locked frequency VCO output continues to run at 20 kHz, but with the same phase as the incoming 10 kHz waveform. The 20 kHz VCO output (a square wave at this stage) is then put through a 20 kHz bandpass filter and becomes a sinusoid once more, and is then applied to one input of the mixer.

The other input to the mixer is derived from the amplified photodiode output. This is the signal that contains the second harmonic information. The incoming signal is passed through two cascaded 20 kHz bandpass filters in order to remove the fundamental component at 10 kHz, while amplifying the second harmonic. The filtered signal is then mixed with the in-phase reference generated by the PLL.

The final stages of the system involve a low pass filter, which isolates the DC/low frequency band of the mixer output, and finally an output amplifier to increase the signal strength. When monitored with an oscilloscope, the output of the system represents the second harmonic component of the waveform received by the photodetector. The block diagram of the PLL circuit is show in Figure 3.3.

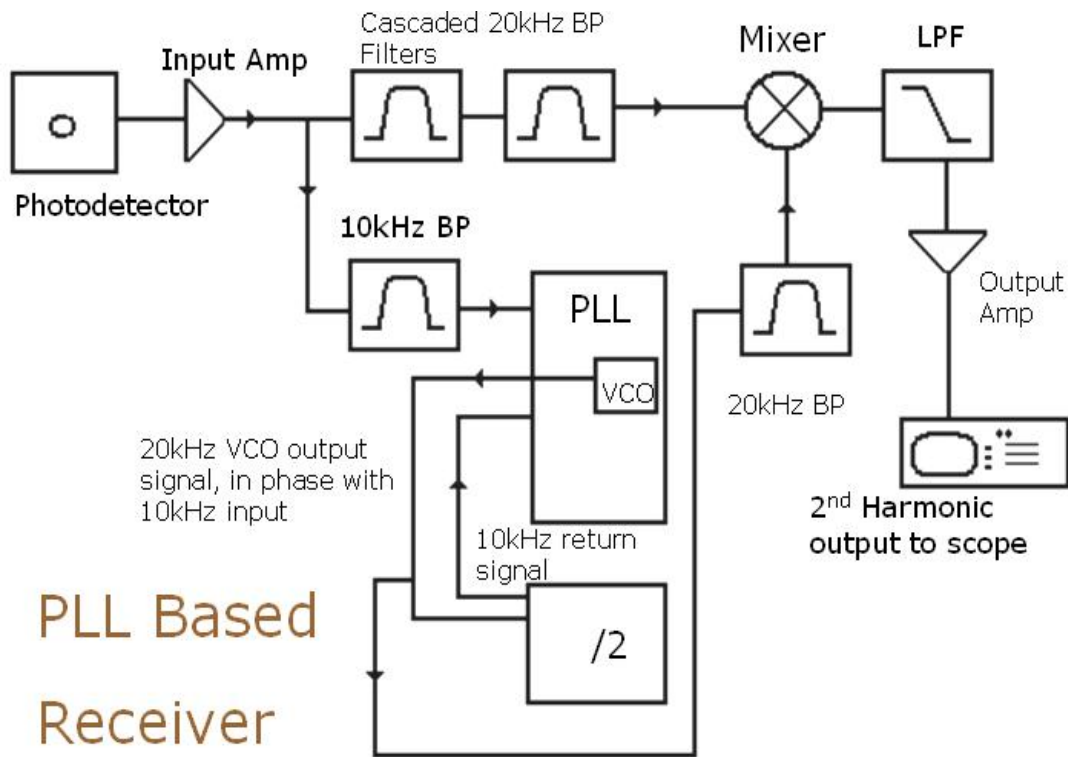


Figure 3.3 – Block diagram of the PLL receiver system.

### 3.4.3 External Reference Receiver

The external reference system relies on the same fundamental principles as the PLL system for detection; namely using an in-phase reference at 20 kHz to mix down the absorption signal. The major difference is in the generation of the reference waveform. As the name implies, rather than using a reference generated by the receiver, the system relies on a reference waveform imported from the laser driver.

The laser driver modulation output to the VITC 002 board is very small in magnitude, so the output supplied to the receiver is taken prior to the final voltage divider. Since the output of the modulation board is at 10 kHz, the receiver employs a frequency doubling circuit to bring the frequency to 20 kHz. Although the reference is now the exact same frequency as the incoming waveform received at the photodetector, the two wave forms are almost certainly out of phase with

each other. The external reference is therefore passed through an adjustable phase shifting circuit before its entry in the mixer.

The received signal from the photodetector is passed through two cascaded 20 kHz bandpass filters just as in the PLL case. Once again this is to eliminate outside noise the fundamental frequency as much as possible. The remaining second harmonic information is then mixed with the external reference, low pass filtered into the DC band, and finally amplified for best signal strength. One major difference of this circuit when compared to the PLL system is that it must be tuned for best results using the phase shifter. Figure 3.4 is a block diagram of the external reference receiver.

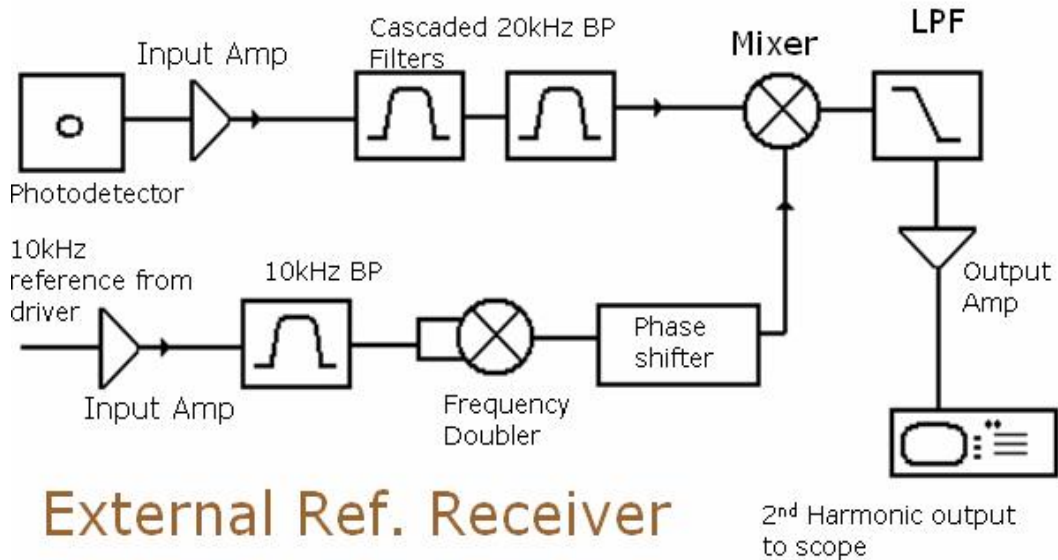


Figure 3.4 – External reference receiver block diagram.

## Chapter 4: Experimental Results

The following is a presentation of the results obtained over a variety of different testing conditions. The graphs shown are saved images generated by the oscilloscopes in the lab. Based mainly on availability, several different oscilloscopes and capture methods have been employed, including Tektronix TDS 2012, TDS 3032B, and Agilent DSO5032A. Using different capture methods causes some difference in graphical resolution and style, but the overall accuracy is relatively similar.

### 4.1 Receiver Functionality Demonstration

To demonstrate the functionality of lock-in detection, the following figures show the waveforms present at each stage of the receiver circuit. The progression of the incoming signal through the receiver circuit is shown at the same operating conditions, in this case, a 500ppm-m cell of CH<sub>4</sub> is in the path.

In the phase-locked loop receiver, the input waveform after the first amplification stage is shown in Figure 4.1, channel 2. Channel 1 displays the tracking output from the driver, displaying both the ramp current and high frequency modulation.

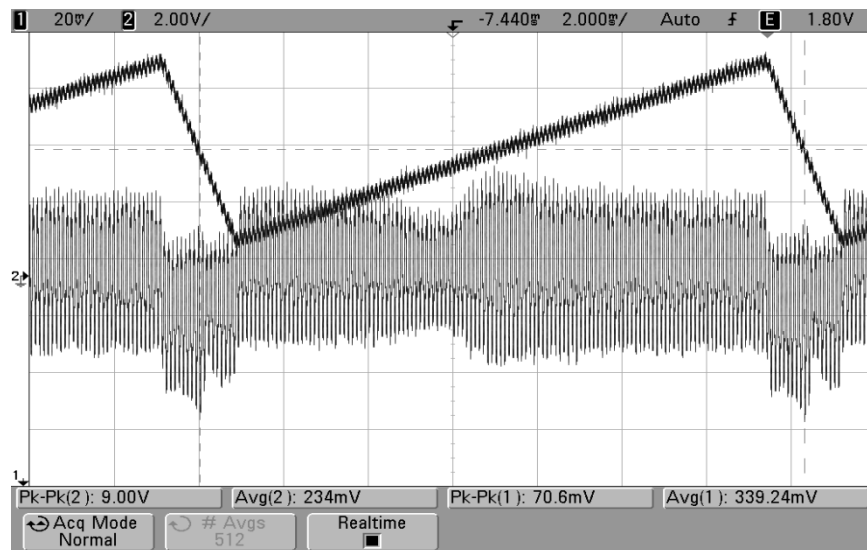


Figure 4.1 – Receiver input from the photodiode, after first amplifier stage, 500ppm-m gas sample.

At higher concentrations, such as those demonstrated in figure 4.1, the effect on the modulation signal is clearly visible on the envelope of the sine wave. In circumstances where there is no gas, the envelope of the modulation is simply a flat line.

Figure 4.2 is the input signal after passing through the two cascaded 20 kHz bandpass filters. Although a large component of the 10 kHz carrier still remains, the shape created by the gas absorption has been significantly increased.

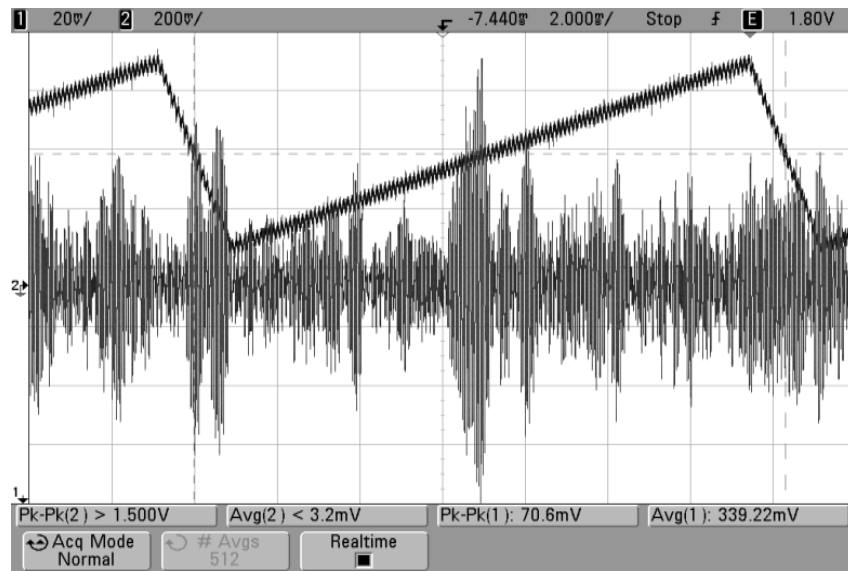
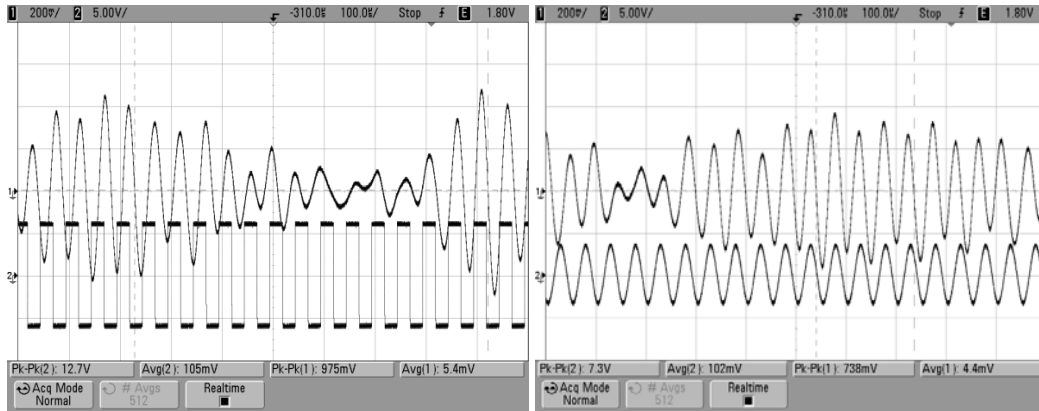


Figure 4.2 – Output of the 20 kHz bandpass filters with a 500ppm-m gas methane sample.

As explained in chapter 3, the PLL uses the 10 kHz carrier frequency to generate an in-phase 20 kHz reference for mixing with the input. Figure 4.3 shows the output of the voltage controlled oscillator as a square wave (a), and after passing through a 20 kHz bandpass filter (b). When compared with the input waveform (top), it is clear that the phase matching produced by the PLL is excellent.



(a) (b)  
 Figure 4.3 – VCO 20 kHz output (bottom) compared to signal 20 kHz (top) (a), and the same comparison after a 20 kHz bandpass filter (b).

The mixer output produced by the multiplication of the PLL generated reference and the input 20 kHz waveform is shown in Figure 4.4.

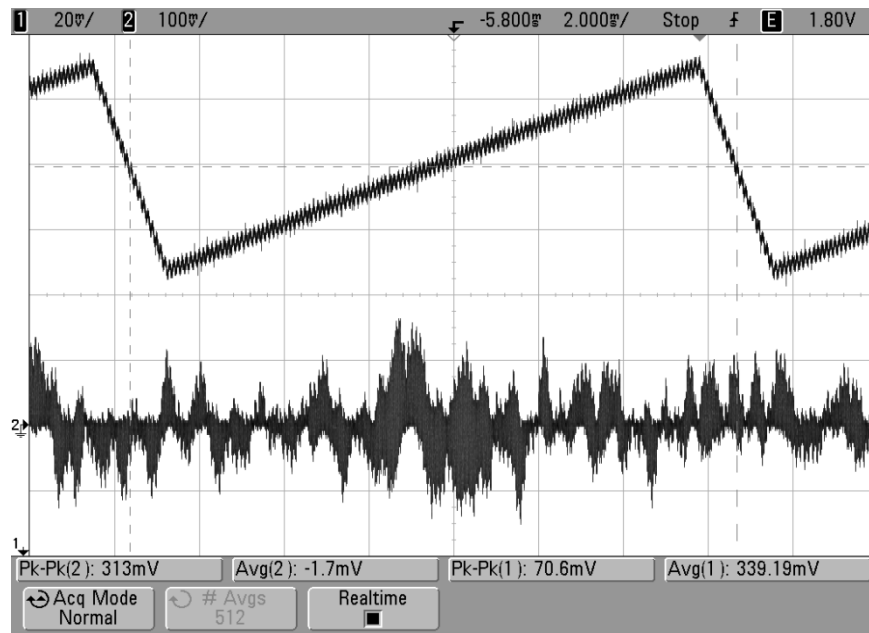
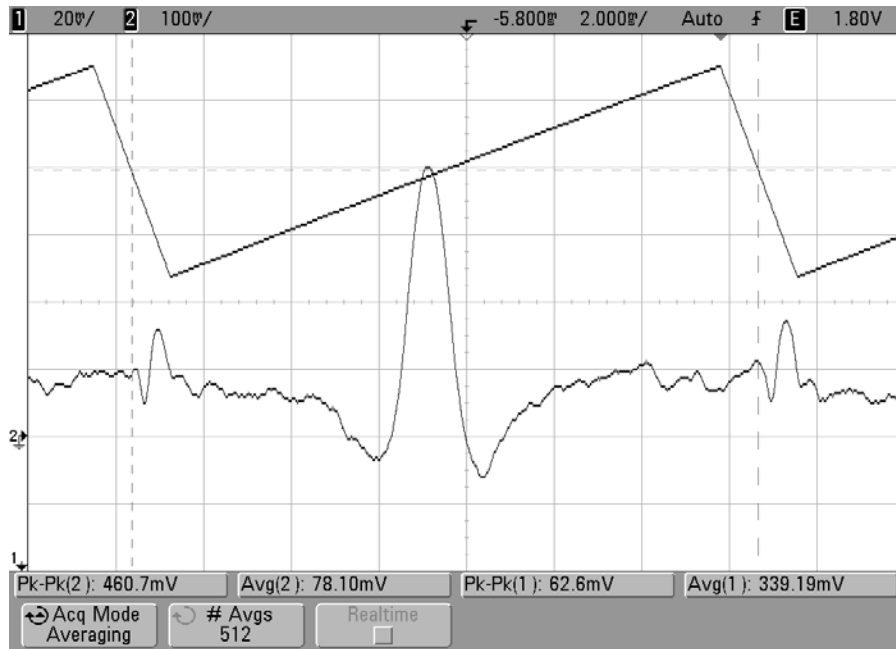
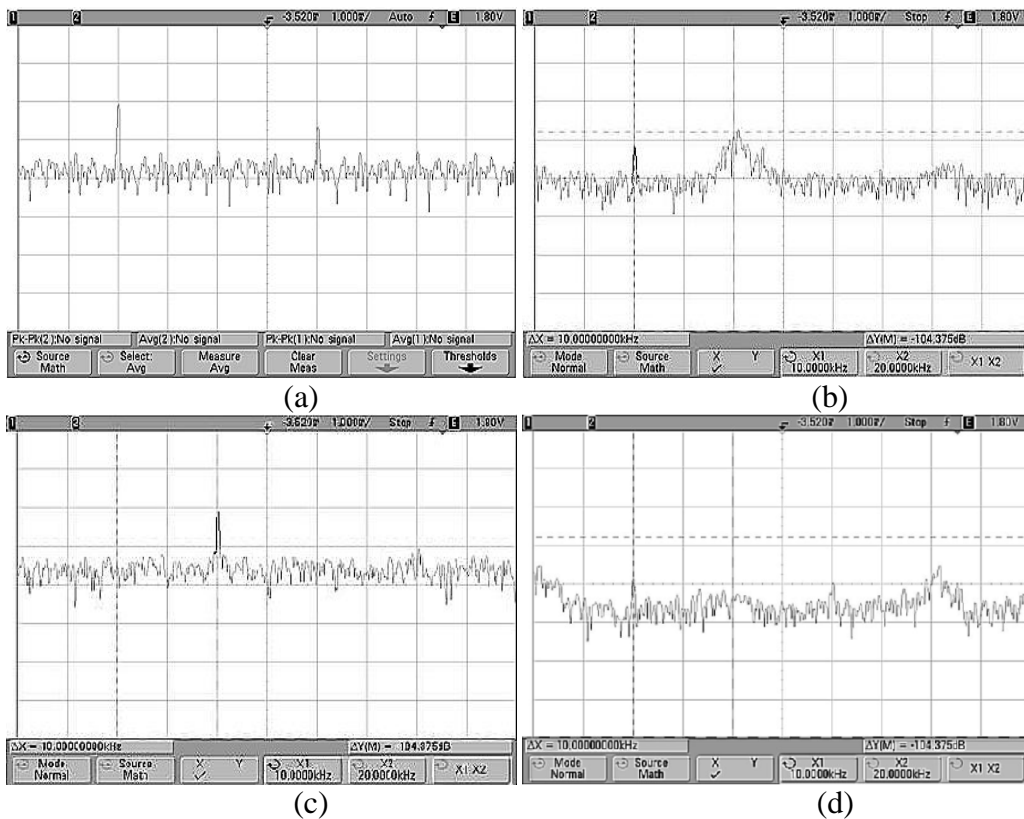


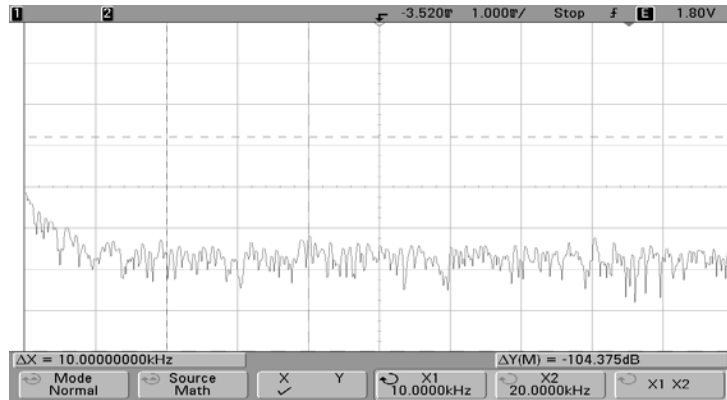
Figure 4.4 – Mixer output with a 500ppm-m gas sample

Finally, the output after the low pass filter and output amplifier is shown in figure 4.5, with 512 averages.



It is also useful to consider the frequency domain signals in the receiver. Figure 4.6 shows the corresponding fast Fourier transforms (FFT) for various signals in the PLL receiver.





(e)

Figure 4.6 – Frequency domain signals at various stages of the PLL receiver.

In Figure 4.6, (a) is the frequency domain representation of the incoming signal from the photodiode after the input amplifier. The strongest component of the signal is at 10 kHz, a small component at 20 kHz is visible, and the 30 kHz harmonic of the modulation signal is also quite strongly represented. Illustration (b) corresponds to received signal after passing through the two 20 kHz bandpass filters. The effect of the filters is clearly apparent, as the 10 kHz carrier has been drastically reduced, while the 20 kHz information has been amplified significantly. Figure 4.6 (c) is the reference waveform generated by the PLL prior to mixing, and is a clean sinusoid at 20 kHz. Figure 4.6 (d) is the output of the mixer. As predicted by communications theory (and the identities regarding multiplication of sinusoids), the mixing of a 20kHz and a signal containing 10 kHz and 20 kHz components produces sum and difference components at 0 and 40 kHz (20-20, 20+20) and at 10 kHz and 30 kHz (20-10,20+10). Finally in (e), the 20 kHz information that has now been down-mixed to zero is isolated using a low pass filter.

For the most part, the external reference receiver exhibits very similar time and frequency domain characteristics to the PLL receiver. Of course, the main difference between the two is the use of a reference generated by the driver rather than one produced by the receiving circuitry. Unlike the PLL receiver, the external reference version must be tuned to an ideal phase shift for best results. Figure 4.7 (a) shows the amount of phase shifted required for best mixing results,

and (b) compares the reference with the 20 kHz absorption information. Note that in (b), rather than being in phase, the waveforms are perfectly out of phase. This is due to the fact that the phase shifter does not have the capability to shift in the full range of  $[-\pi, \pi]$ , and as a result, the fully inverted phase was the only one achievable. Fortunately, having inverted phase does not reduce the amplitude of the mixed results, but merely produces an inverted  $2f$  shape.

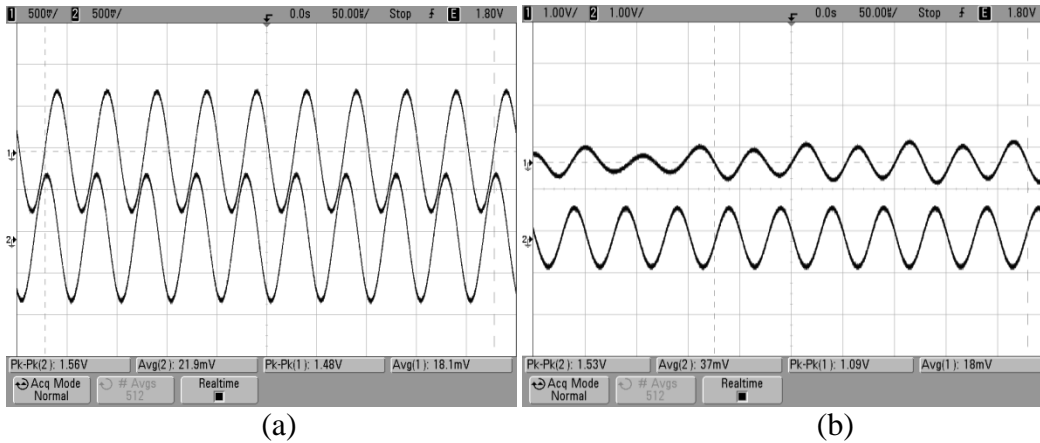
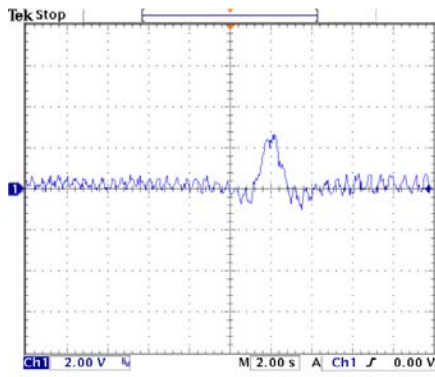


Figure 4.7 – (a) 20 kHz reference waveform from the driver prior to shifting (bottom), and after (top). (b) Shifted waveform (bottom) compared to the receiver input (top).

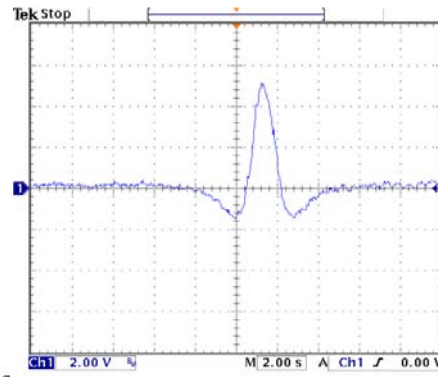
## 4.2 Modulation Index and Temperature Scanning

One of the first experiments undertaken was the isolation of an optimum modulation index for spectroscopy. Theory predicts that the modulation index greatly affects output signal strength as well as noise performance (refer to section 2.4). The receiver system was tested with a variety of modulation indexes in order to determine the best range.

The experimental set-up employed a VCSEL modulated with 10 kHz sine wave, and ramped through a wavelength range using temperature. (This experiment was done before the realization of a working current scan model). The modulation index of the high frequency sine wave was changed at regular intervals, and the effect on received second harmonic signal strength was observed. The test subject in this case was a 1.22m cell of 50 ppm methane. Results at several different points are shown in figure 4.8.



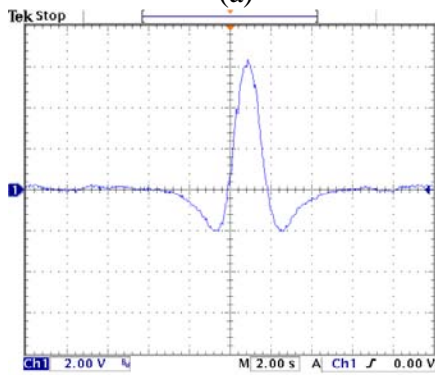
7 Jun 2006  
15:07:09



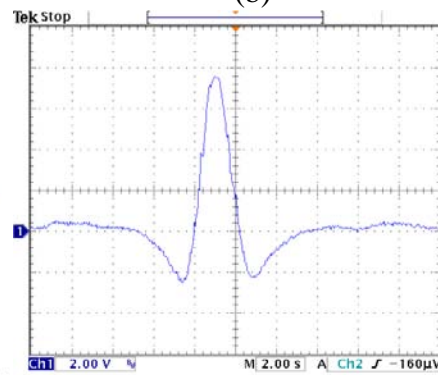
7 Jun 2006  
15:18:07

(a)

(b)



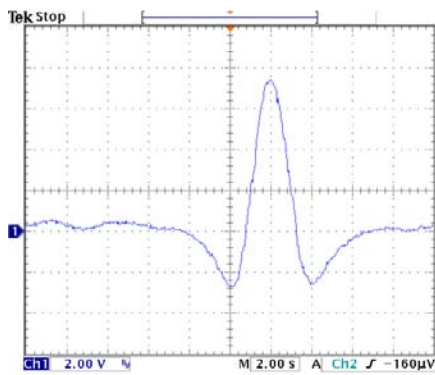
7 Jun 2006  
15:27:03



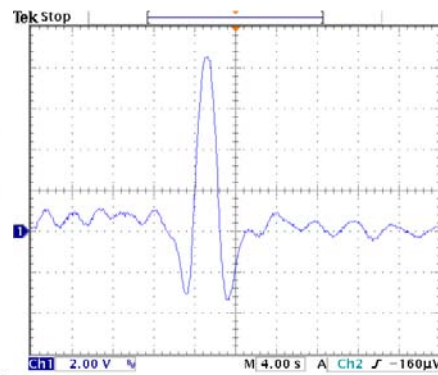
7 Jun 2006  
15:46:20

(c)

(d)



7 Jun 2006  
16:01:18



12 Jun 2006  
09:57:47

(e)

(f)

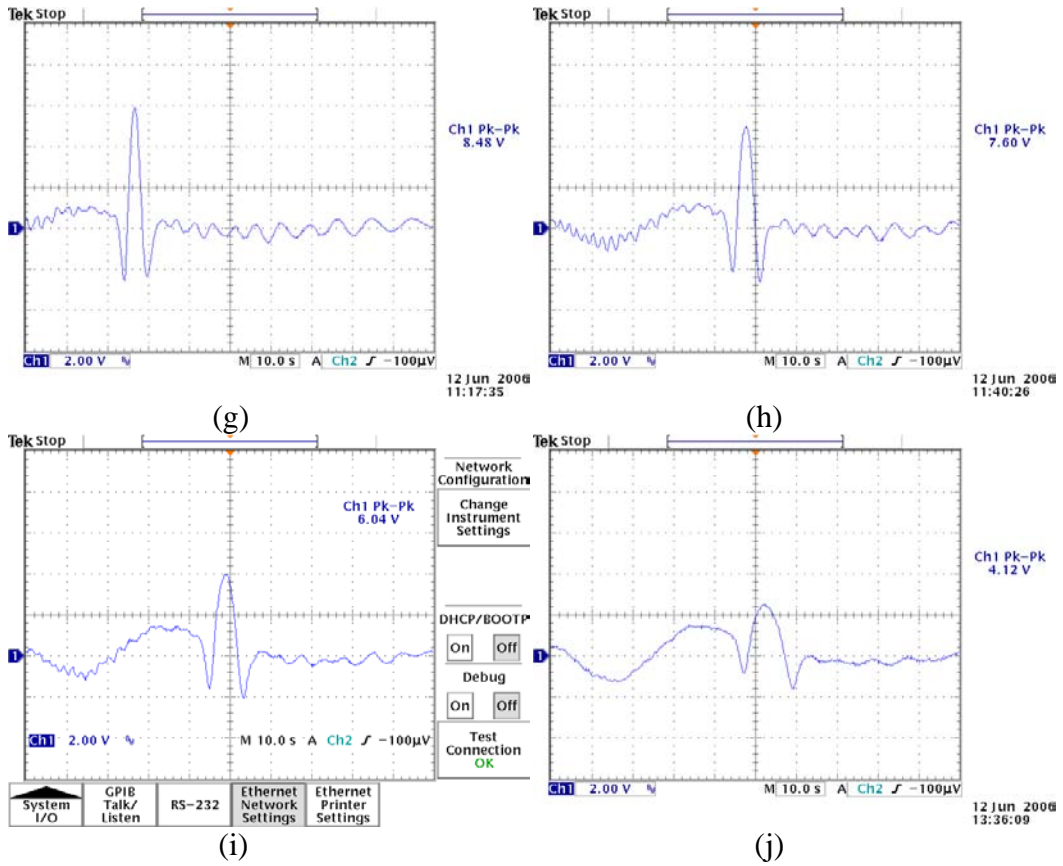


Figure 4.8 – Received second harmonic at (a) 2mV peak to peak sine wave modulation strength, (b) 3mV, (c) 4mV, (d) 5mV, (e) 6mV, (f) 8mV, (g) 10mV, (h) 12mV, (i) 15mV, (j) 20mV.

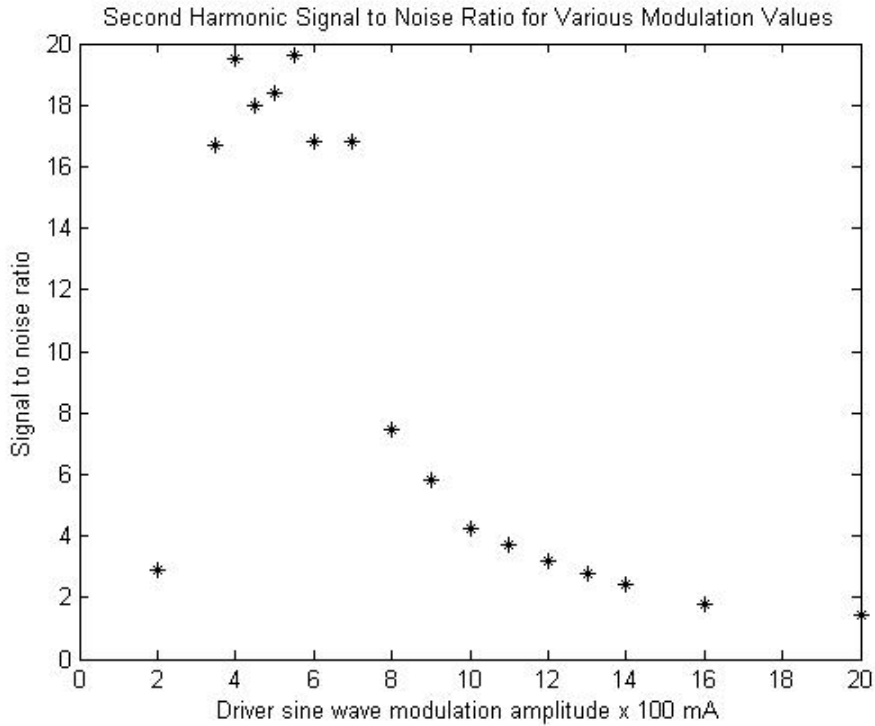


Figure 4.9 – Signal to noise ratios for various modulation amplitudes

The results of this experiment clearly indicate that there is an optimal range of modulation index which gives the best signal to noise performance. It is interesting to note that stronger modulations are not necessarily better, as the best results are achieved at between .04 and .045 mA peak to peak.

In order to compare these experiments with theoretical models, the optical modulation index,  $m_{opt}$ , must be computed.

$$m_{opt} = \frac{\Delta\nu_{laser}}{\Delta\nu_{line}} , \quad (4.1)$$

where  $\Delta\nu_{laser}$  is the maximum deviation in the operating frequency of the laser produced by the modulating current, and  $\Delta\nu_{line}$  is the full width half maximum of the absorption line at the appropriate wavelength. The expression for  $m_{opt}$  also takes the same form when considered in wavelength; despite the inverse relationship between frequency and wavelength, a larger variation in wavelength still produces a larger change in frequency.

The VCSEL laser used to generate these results is centered around 1654nm. In this experiment, the laser was operated at a DC bias of 2.31mA, and temperature scanned in a region of 18.5C to 25C. Consultation of the data sheet of the laser (refer to appendix A) does not have a listing for operating wavelength in this range of temperatures, however, by observing the trend shown by the 40C and 30C functions, a safe estimate is that the laser sweeps from around 1650.5nm to 1651.5nm under these conditions. For simplification of calculations, the tuning rate of the laser at these temperatures is assumed to have the same slope characteristics as the 30C graph. Therefore, in the range of interest, the tuning rate of the laser is approximately 0.86nm/mA. The absorption line for methane in this region of wavelengths, as estimated by HITRAN (see appendix C), has a full width half maximum of approximately .05nm.<sup>(15)</sup> By recalling that each applied modulation voltage applies a corresponding current to the laser of 1mA/100mV, the modulation index for each scenario is given by Table 1.

$V_{mod}$ (mV)	2	3	4	5	6	8	10	12	15	20
$m_{opt}$	0.344	0.516	0.688	0.86	1.032	1.376	1.72	2.064	2.58	3.44

Table 1 – Optical modulation indices for various modulation amplitudes

Comparison of these results with the theoretical results in the  $2f$  background theory presented earlier shows some similarities and some differences. The overall shape of figure 4.2 is similar to Figure 2.9 (a), although somewhat exaggerated. The maximum amplitudes occur at lower modulation indices than predicted by the theory, but the theoretical model only considers noise from intensity modulation. One interesting result is that at very high modulation indices, the resultant  $2f$  waveform agrees very closely with the theoretical model such as the  $m=10$  case in 2.9 (c). The maximum modulation index produced in the lab was 3.44, but the waveform was already approaching the  $m=10$  theoretical waveform. In fact, the entire results seemed compressed when compared to the theoretical expectations.

In keeping with this experiment, it is also important to consider the effect (if any) of the modulation signal on the overall noise floor of the system. For the next test, the gas cell containing 50ppm methane was removed, and observed the final system output under the same ramping and modulation index operating points. Figure 4.10 shows the results of this experiment.

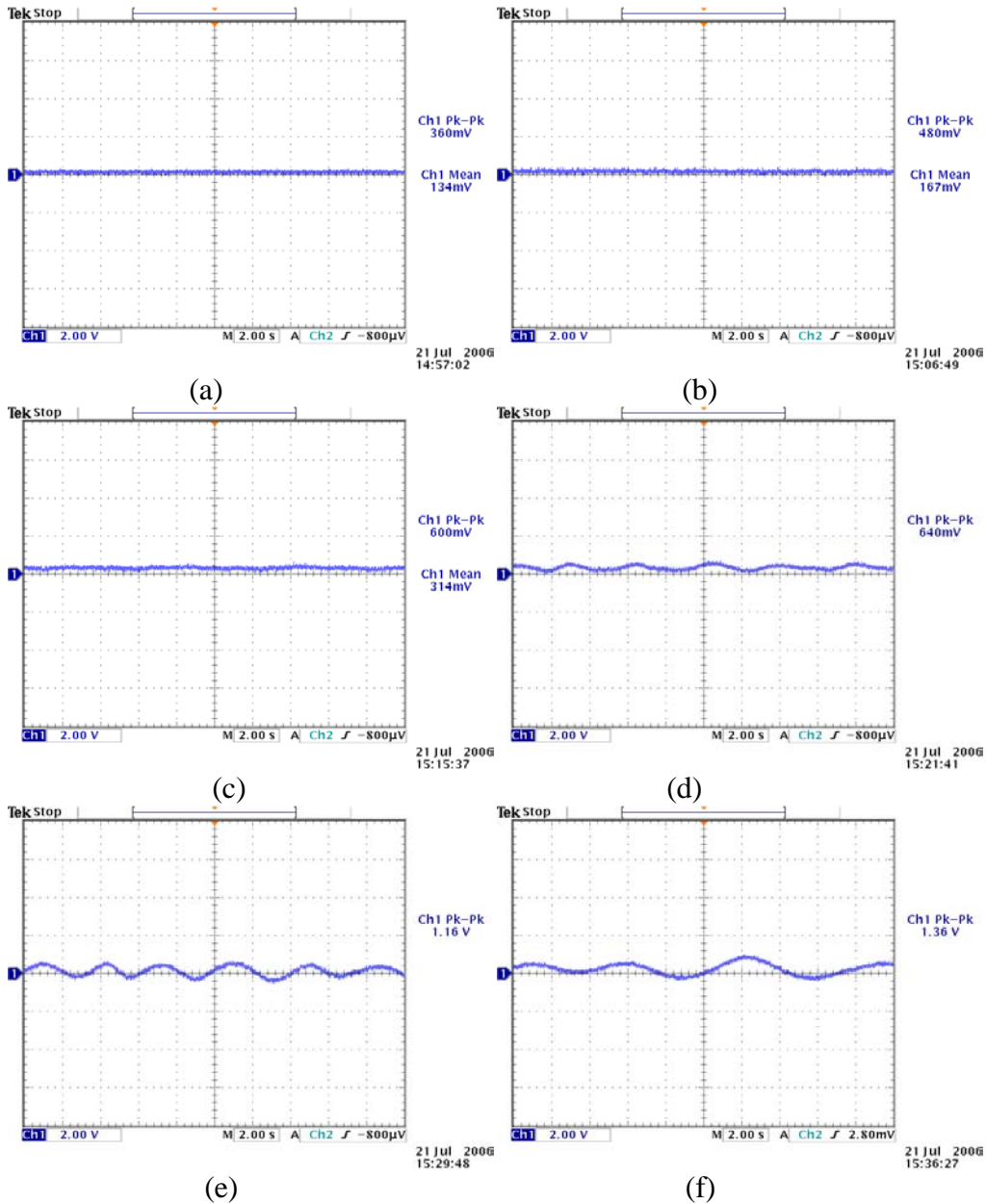


Figure 4.10 – PLL receiver output, no gas cell in path, during a temperature ramp. Results are shown with modulation amplitudes of (a) none (b) 3.5mA (c) 5mA (d) 7.5mA (e) 10mA (f) 12.5mA

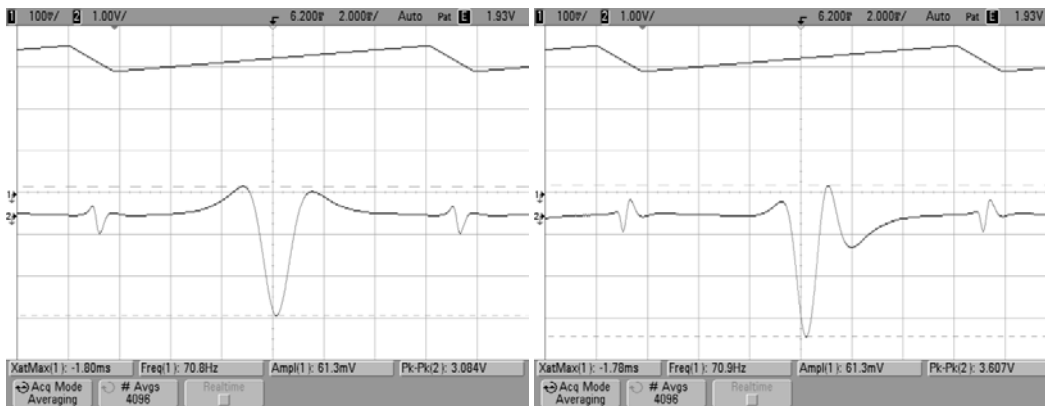
The results show that, in general, increasing the modulation amplitude of the sine wave leads to increased system noise.

### 4.3 Current Scan Results and Receiver Comparison

Although there are advantages to temperature scanning techniques, such as a greater likelihood to avoid etalon related problems, and seemingly better resolution in general, current scans are a more desirable sweeping method. Due to the length of time required to make one scan with temperature, averaging over several scans is impractical. The longer scanning time of temperature also hurts the speed at which results are available (which could be of importance to some applications, especially in safety based environments). Ramping the output with current allows for scans at around 50-100 Hz (with one scan performed per cycle), and higher numbers of scans are easily achievable. Gathering a large sample size in a small period of time allows for averaging, and a much greater data acquisition rate.

Changing between the two systems requires very little in terms of hardware modification. In terms of the receiver, the low pass filter at the output must be adjusted to allow frequencies of approximately 5-10 times the ramp frequency pass, but cut off before the high frequency modulation.

Figure 4.11 shows the results of both receivers operated with current scanning at a variety of concentrations.



(a)

(b)

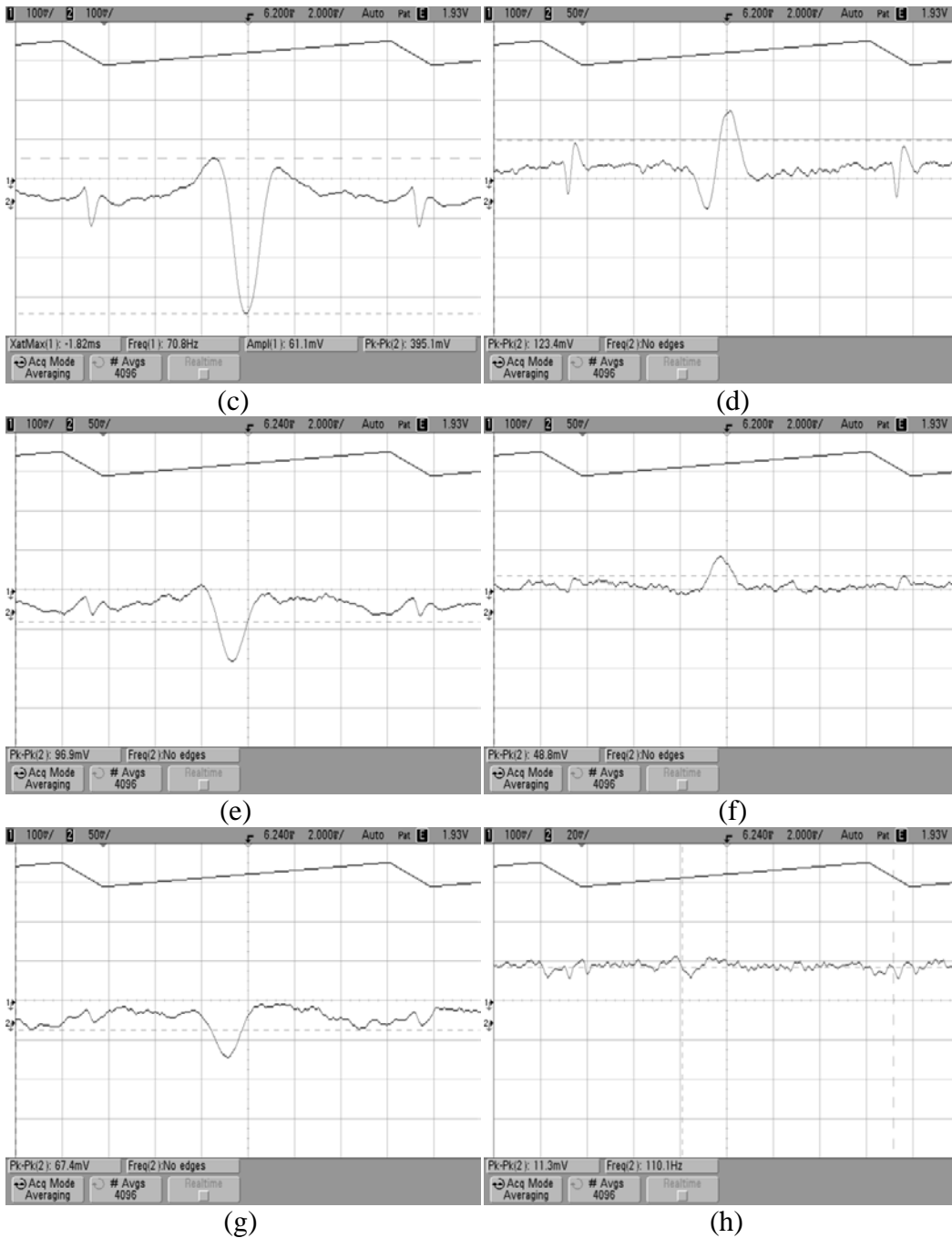


Figure 4.11 – External reference receiver (left) compared to phase-locked loop receiver (right) at (a),(b) 3000 ppm, (c),(d) 500 ppm (e),(f) 100 ppm and (g),(h) 50ppm (in a 50 cm cell).

In general, at higher concentrations, the results generated by the two systems are fairly similar. The asymmetry in the PLL results in this particular example is due to a slight mismatch in the phase lock, which is intermittent. Towards the lower concentrations, it becomes clear that the external reference receiver produces better results. Although tuning the external reference is

necessary upon first operation, the amount of phase shift needed for optimal results remains relatively constant. The ability to tune the phase of the mixing signal also allows for elimination of asymmetric results such as those shown in Figure 4.11 (d). The ability to adjust the external reference receiver, and its superior sensitivity make it the better of the two receiver types.

#### 4.4 Waveform Validation

As the system comes close to its detection limit, the noise in the system begins to cause more and more distortion of the detected waveform. Around this point, it is important to consider how to determine whether a signal is produced by actual gas detection, or is just a noisy waveform that resembles absorption. There are several ways to test the validity of a waveform; if a detected waveform passes these tests it is reasonable to conclude the signal is indeed a product of gas absorption.

The first test is simply to block the laser beam. Any signal produced by the detector and receiver circuitry with no laser input is purely a product of system noise and is obviously not related to absorption. The PLL and external reference receivers that were constructed for the system exhibit very low system noise with the beam blocked. Furthermore, the dominant noise source under this regime is white Gaussian noise, which can be averaged out quite easily (see Figure 4.12).

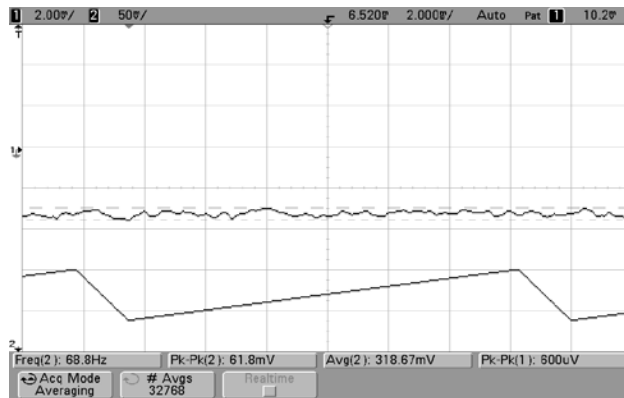


Figure 4.12 – External reference receiver output with no light input, averaged 32,000 times. The averaged output is less than 1mV.

Another test for determining the validity of a detected signal is to adjust the DC bias of the laser. Altering the DC bias consequently changes the laser operating frequency, and should cause a shift in the detected signal relative to the ramp. Enough change in the bias current can cause the absorption line to migrate right to either end of the ramp, and eventually completely out of the picture. Alternatively, if the changes in the bias current produce no effects on the detected signal, then absorption is not causing the waveform.

At operating points near the detection limits, it can be difficult to discern which peaks, if any, correspond to absorption. Comparison of the signal with a sample from a higher concentration can serve as a method for validation. As long as the DC bias current and operating temperature of the laser remain constant, the absorption peak should occur at the same position on the current ramp regardless of the amount of gas in the path. In an open path regime, inserting a cell containing methane into the path is quick and easy to way to establish the location of the absorption line. In measurements where a sampling cell is used (and the ambient path length is small enough to be negligible), starting at a higher concentration and gradually reducing the amount of gas in the cell allows for accurate determination of the line placement. Conversely, a baseline measurement for the system can be observed by filling the cell completely with another gas which does not absorb in the region of interest. In my case, nitrogen is perfect for such a role. Clearly a reading with no absorbing gas is unavailable in the ambient case however, since it is essentially impossible to ensure no methane exists in the atmosphere.

## **4.5 Open Path Results**

With the goal of these experiments being to produce a system capable of operating in open path regimes, it is important to get accurate open path readings (change this). One disadvantage of VCSEL systems is that their output power is generally extremely low. Where other lasers such as DFBs produce enough

optical power to allow beam collection even from scattering media, we were unable to collect enough light from scattering surfaces when using a VCSEL. As a result, the usage of a VCSEL system in open path spectroscopy requires a retro-reflector, and fairly accurate system alignment. The requirement of an external reflector is a serious detriment to the ability of a VCSEL system to be made portable and handheld, but the system can still be employed in open path situations where alignment is possible.

The ambient concentration of methane in the atmosphere varies slightly depending on the region and many other factors. In most outdoor locations, the average is around 1.75 ppm<sup>(24)</sup>, while indoors the average concentration is slightly higher, around 2.0 ppm. In performing spectroscopy experiments, the total amount of absorption is a function of both the concentration and path length. For example, a 1 meter path length through 2.0 ppm methane produces 2 parts per million meter (ppm·m); a path length of 10 meters yields 20 ppm·m (or the same as 1 meter of 20 ppm methane). In open path regimes, it is generally necessary to use fairly long path lengths in order for ambient absorption to be visible. Higher power systems that employ DFBs or high power edge emitting semiconductor lasers often have path lengths in the hundreds of meters or higher. In general, a VCSEL does not have enough power to cover that sort of range and still be resolvable at the detector.

The first open path experiment in the lab employed the use of several mirrors in order to achieve an effective path length of around 10 meters. Figure 4.13 shows the results of an open path measurement taken in the lab with a path length of 12.43 meters (approximately 25 ppm). This experiment was performed using triangular ramping, which allowed for averaging of the output signal for better results (64 averages in this case).

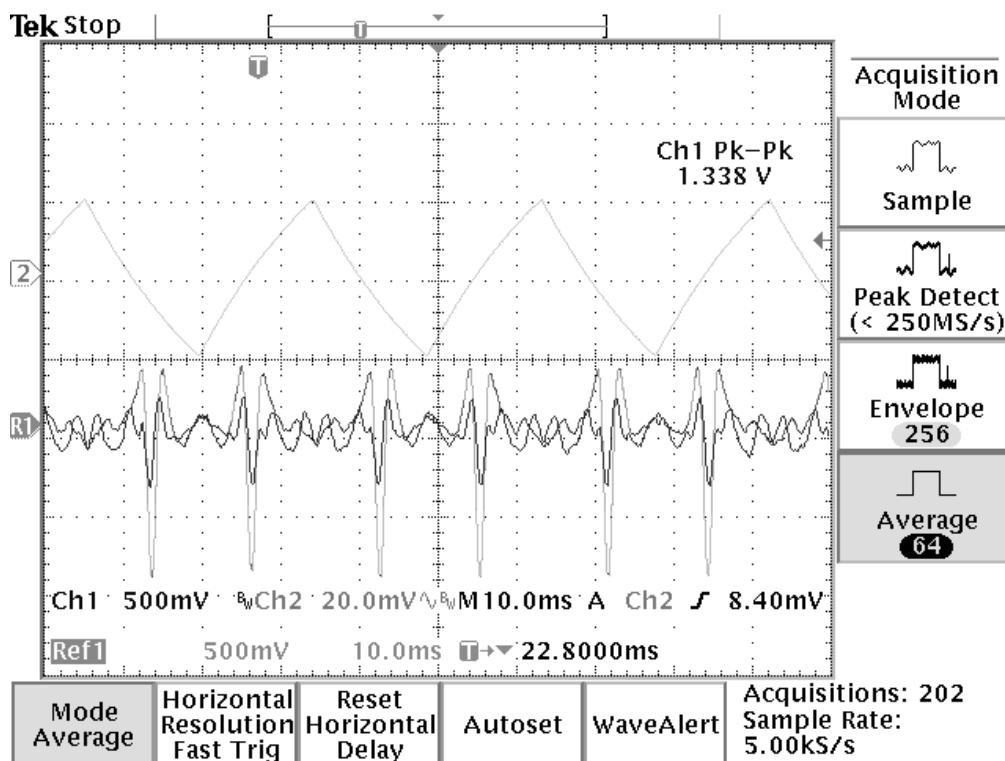


Figure 4.13 – Open path measurement of ambient methane in the lab (black waveform), and a comparison measurement of the same path length with a methane cell also in the path (grey).

The ambient waveform in figure 4.13 shows some clear distortion from an ideally shaped  $2f$  waveform, due to being near the detection limit of the system; however the overlay of a higher concentration clearly demonstrates that the detected signal is indeed produced by gas (and not noise).

## 4.6 Data Processing

The theory of absorption spectroscopy shows that absorption is a linear effect. That is to say, halving the concentration of absorbing molecules in a particular scan should halve the expected resultant waveform. Linearity of absorption allows for fairly simple curve fitting and calibration data.

Linear regression is a powerful method for curve fitting and comparison of data sets. In general, data sets are compared with a linear regression model defined by the following formula:

$$y_i = \sum_{j=1}^m X_{ij}\beta_j + \varepsilon_i, \quad (4.2)$$

where  $x_i$  represent the individual components of  $m$  independent data sets,  $y_i$  is the corresponding dependent variable, and  $\varepsilon_i$  are the error terms. In the case of relating to two data sets, where one is chosen as the basis, and the other is the responding variable, the generalized form reduces to:

$$y_i = \beta_1 + x_i\beta_2 + \varepsilon_i. \quad (4.3)$$

Here, the relationship becomes a straight line, where  $m = 2$ ,  $\beta_1$  is the intercept,  $\beta_2$  is the slope of the line, and the basis coefficients are  $X_{i1} = 1$  and  $X_{i2} = x_i$ .<sup>(25)</sup>

The mathematics governing linear regression can be fairly complicated, so it is valuable to understand the usefulness of the technique. As mentioned earlier, the linearity of absorption allows for direct comparisons between samples at different concentrations. By regressing samples of two different concentrations, the slope of the linear regression model gives the ratio of the concentrations. In these calculations, the choice of the basis set is simply the data set produced by a scan at fairly high concentrations. The signal produced by such a scan generally exhibits a close to ideal shape with little to no discernable noise. Data from various other concentration levels can then be compared with the basis signal using regression.

All of the regression calculations were done using MATLAB, which has pre-programmed linear regression algorithms available. MATLAB also produces a number of statistical measures pertaining to a given regression; most importantly, the coefficient of regression,  $R^2$ . The quantity  $R^2$  is a statistical measure of a regression fit, the value of which represents how correlated the data sets in question are. The coefficient of regression can only assume values between 0 and 1, where 0 is two data sets that are completely different, and 1 represents identical data sets.

In using linear regression to estimate concentrations and as a basis for signal to noise ratio considerations, production of the best comparisons requires

some initial operations on the data sets. Of crucial importance is that data sets must be properly aligned; the maxima occur at the same place. Also, windowing is employed to remove switching spikes on ramp transitions. Changes in alignment of the signal can be caused by variations in temperature, the electrical currents in the driver, and the placement of the waveform trigger on the oscilloscope. As long as the ramp signal remains similar in amplitude and frequency, and same methane line is scanned, shifting the alignment of the signals for better comparison does not affect the integrity of the results. An example of the way in which alignment shifting and windowing affects the regression slope and  $R^2$  is shown in figure 4.14.

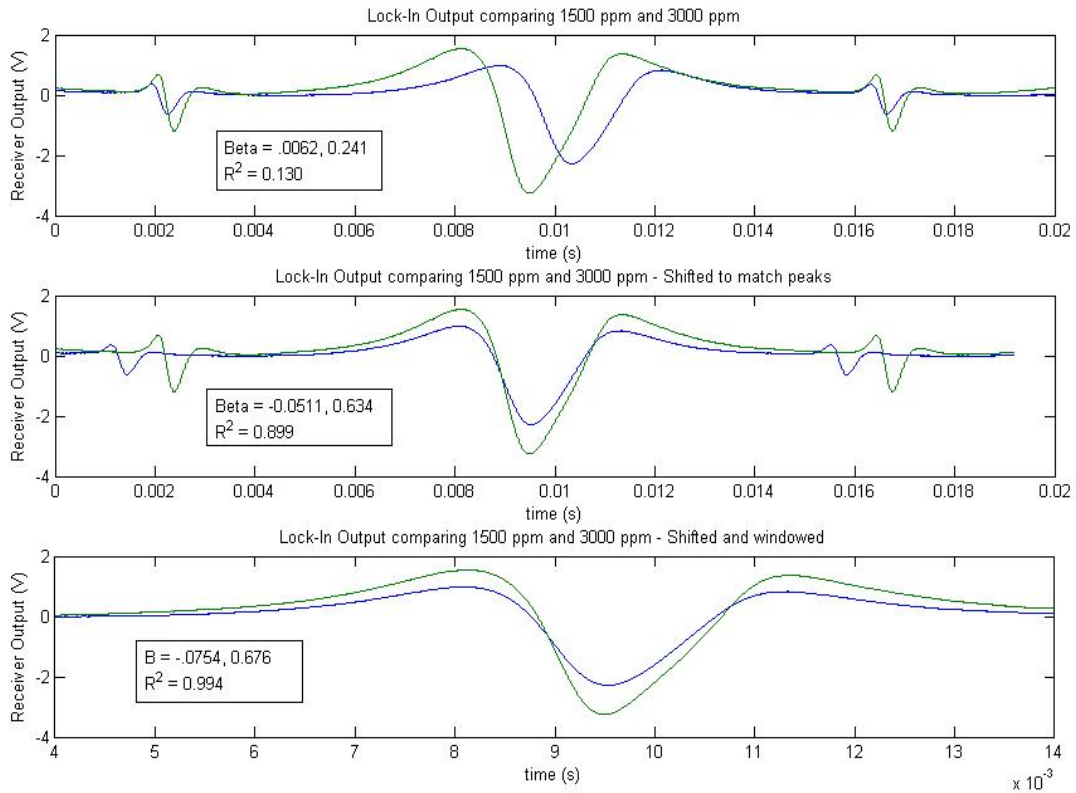


Figure 4.14 – Sample showing the effects of shifting and windowing on regression slope (second number of Beta) and  $R^2$ .

As is clear from figure 4.14, even waveforms that have a great deal of similarity give very poor results for  $R^2$  unless properly shifted. The elimination of the switching spikes (transients caused by the extremely rapid downward shift of

the ramp current) also improves the accuracy of the regression results. It should be noted that the switching spikes represent the same absorption signal as the upwards scan, but the speed at which the downwards transition occurs causes distortion. Considering only the upwards scan leads to more accurate readings.

Using the results of a number of readings taken at concentrations ranging from 50ppm to 2000ppm, a simple calibration curve based on linear regression was created. The data point at 500ppm was chosen as the basis sample, as it was the lowest concentration that exhibited little to no noise (choosing the lowest possible value provides more accurate results at very low concentrations). The results are shown in Figure 4.15.

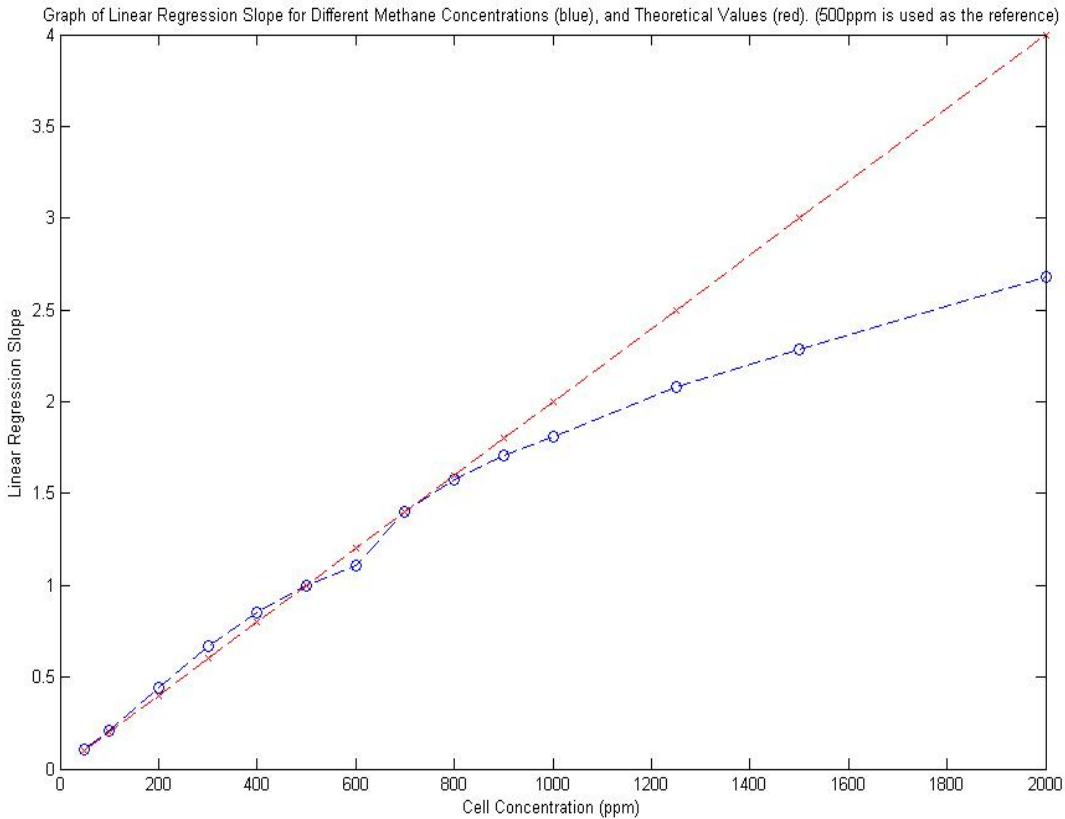


Figure 4.15 – Experimental and theoretical regression slopes for various gas concentrations (using 500ppm as the basis).

The results show excellent agreement between experimental results and theoretical linearity at lower concentrations, however the experimental results level off at higher concentrations. This is caused by saturation of the absorbing signal, and is an expected occurrence. Although not shown on the figure, the  $R^2$

values for the high concentration data points were all very high (over 0.9, most over 0.99). In general, as the concentration of the sample is lowered, the  $R^2$  value is expected to lower due to reduced signal levels (making the absorption less distinguishable from noise). Table 2 shows the corresponding  $R^2$  values for each concentration.

Concentration (ppm)	$R^2$	Concentration (ppm)	$R^2$
50	0.67018	700	0.99911
100	0.86074	800	0.99623
200	0.95286	900	0.99395
300	0.9797	1000	0.98711
400	0.99194	1250	0.99614
500	1	1500	0.99363
600	0.99097	2000	0.99144

Table 2 – Value of the regression coefficient at various concentrations

When regressing a sample against a high concentration reference, as the concentration of the sample becomes smaller, the accuracy of the slope reading decreases. Near the limit of detection, both the slope and regression coefficient are very low. Another method of using regression to push the limits of detection is to correlate the regression coefficient to concentration. At high concentration samples this method is useless, since the regression coefficient forms essentially a flat line, but as the concentration lowers, the  $R^2$  value begins to taper off. Curve fitting the regression coefficient slope can also offer insight into the amount of gas in the sample. The basis for this method is that, when there is no gas in the sample, the  $R^2$  should theoretically be zero; by adding a slight amount of gas to the system, a change in  $R^2$  can indicate the presence of gas. This is by no means a definitive procedure, and the resultant accuracy cannot be guaranteed, but this is still a valuable tool for estimating the minimum detectable concentration of gas. The procedure for this analysis is modeled on the work of Ram Hashmonay.<sup>(26)</sup>

The data for a regression comparison was collected in the following way: the 50cm cell was placed between the laser and detector with the shortest total path length possible, with the cell connected to a flow mixer for adjusting the

concentration, a number of measurements were then taken at each concentration. It is important for this experiment to have a fairly large data set, since the overall trend of the regression coefficient is the main point of interest. At low concentrations, a high degree of variation is seen in the regression coefficient, therefore the ability to average a large sample size is desirable. Figure 4.16 shows a series of 15 measurements taken through the 50 cm cell at concentrations of 0, 10, 20, 30, 40 and 50 ppm, and the corresponding value of  $R^2$  for each measurement (marked with an x). The 'o' marking shows the average value of the regression coefficient at each concentration.

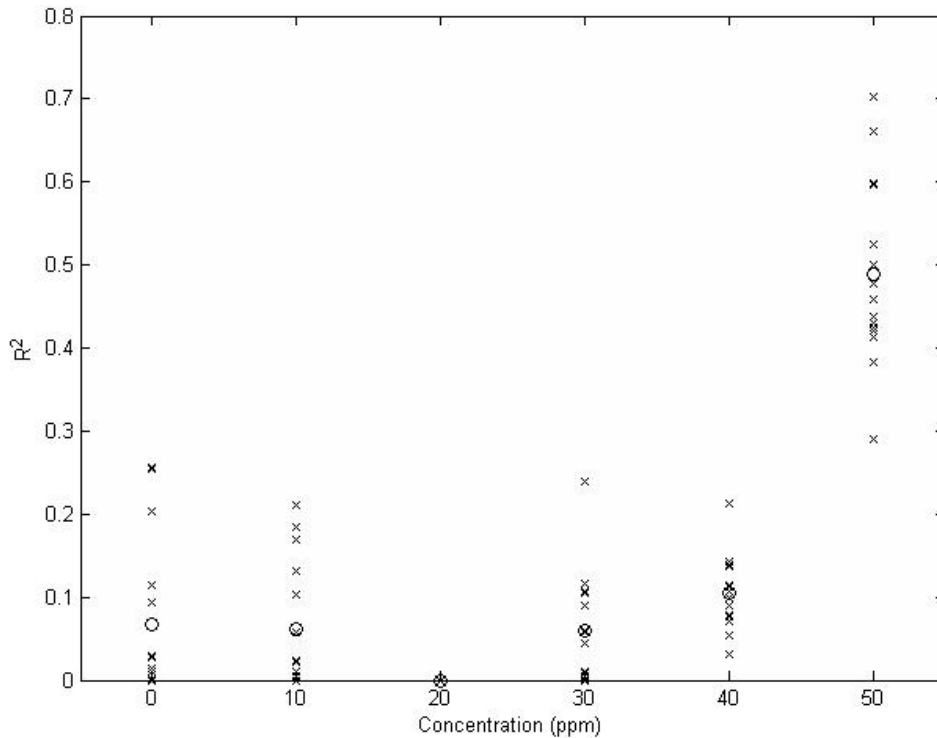


Figure 4.16 –  $R^2$  versus concentration

For the analysis of the results show in Fig. 4.16, regression models that generated negative slopes were automatically set to zero in order to avoid false positives. This is necessary since  $R^2$  can assume fairly large values for situations where the measured signal exhibits correlation to the negative of the reference (the  $R^2$  of a signal regressed against its negative is exactly 1). In this application, negative slopes are not indicative of absorption signal, and the corresponding  $R^2$  data points must be zeroed or discounted. Unfortunately, the results of this

experiment failed to produce a linear relationship between  $R^2$  and low concentrations. Nevertheless, some interesting observations can be noted from Figure 4.16; all the measurements taken at 20 ppm produced negative regression slopes, and were therefore zeroed. Of particular interest is the regression value with no gas – the average for the 15 samples taken with no gas in the cell was .0668. Perfect theoretical conditions would yield  $R^2 = 0$ , however synchronous noise sources are clearly producing some relation. Clearly any value for  $R^2$  below this floor is unreliable.

## 4.7 Wavelet Transforms

It is of great interest in all spectroscopy applications to determine whether the sensitivity of the system can be improved through mathematical analysis and signal processing. One mathematical system that was explored in detail as a potential tool for increasing sensitivity is the wavelet transform. The wavelet transform is a mathematical operator similar to the Fourier transform, however it also gives information on where certain frequencies occur in the time domain. The transform is defined by the equation:

$$T(a, b) = w(a) \int_{-\infty}^{\infty} x(t) \psi^* \left( \frac{t-b}{a} \right) dt, \quad (4.4)$$

where  $x(t)$  is the original signal,  $\psi^*$  is the complex conjugate of the wavelet; a function of  $t$  and the translation scaling factor  $b$ , and the frequency dilation factor  $a$ , and  $w(a)$  is a weighting function. There are many different types of wavelet functions, but they all satisfy the following conditions: finite energy, zero mean, and (in the case of complex wavelets) the Fourier transform must be real and vanish for negative frequencies. The wavelet used in these calculations is a Gaussian based function, more specifically, the negative second derivative of a Gaussian, given by:

$$\psi \left( \frac{t-b}{a} \right) = \left[ 1 - \left( \frac{t-b}{a} \right)^2 \right] e^{-.5 \left\{ \frac{t-b}{a} \right\}^2}. \quad (4.5)$$

This wavelet function is also commonly referred to as the Mexican Hat wavelet, and is a strictly real valued function (so the complex conjugate need not be calculated). Figure 4.17 shows the shape of the Mexican Hat wavelet, and the changes in the function caused by the parameters  $a$  and  $b$ .<sup>(27)</sup>

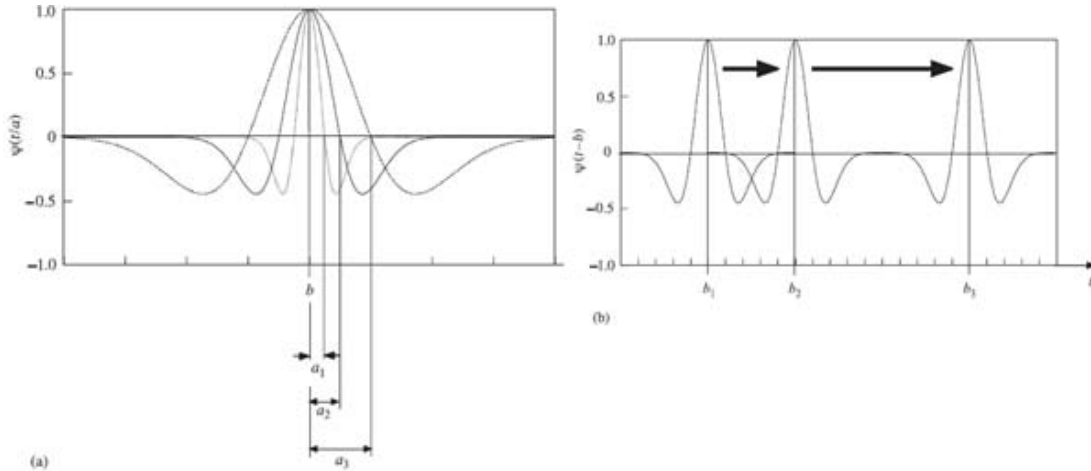


Figure 4.17 – The Mexican Hat wavelet (a) Dilated by the factor  $a$  and (b) translated by  $b$ .  
 Source: Addison, 2002 p. 21 (27)

The Mexican Hat wavelet was chosen for its obvious similarity to the 2<sup>nd</sup> derivative absorption signal of interest in spectroscopy, as well as reduced complexity when compared to other wavelets.

The wavelet transform can be thought of as a convolution of a set of basis wavelets with the signal of interest. The original (“mother”) wavelet is dilated to a specific frequency by the parameter  $a$ , and then scanned through the signal spatially. At each time interval generated by  $b$ , the similarity between the wavelet and the sample forms the value at  $T(a,b)$ . The result of the transform is essentially a surface plot, with axes  $a$  denoting frequency,  $b$  relating to time, and  $T(a,b)$  the height at each point. Because of the frequency scanning properties of the wavelet transform, it can also be thought of as a series of bandpass filters. The goal of employing this transform is to separate random, and hopefully synchronous noise sources from absorption signals by isolating the time and frequency of the absorption.

MATLAB has a powerful toolbox dedicated to wavelet transforms and their applications. Using these tools, wavelet transforms were investigated as a potential noise removal tool. The following figures are surface plots generated in MATLAB, and correspond to the continuous wavelet transform of several different measured absorption signals.

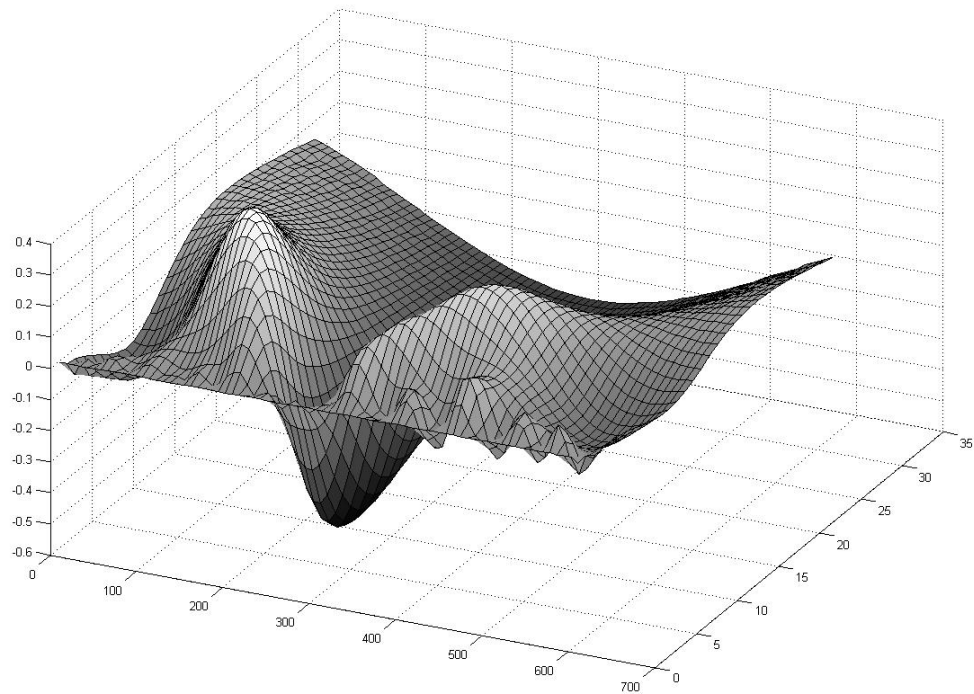


Figure 4.18 – Surface plot of the wavelet transform of a 50 ppm absorption signal.

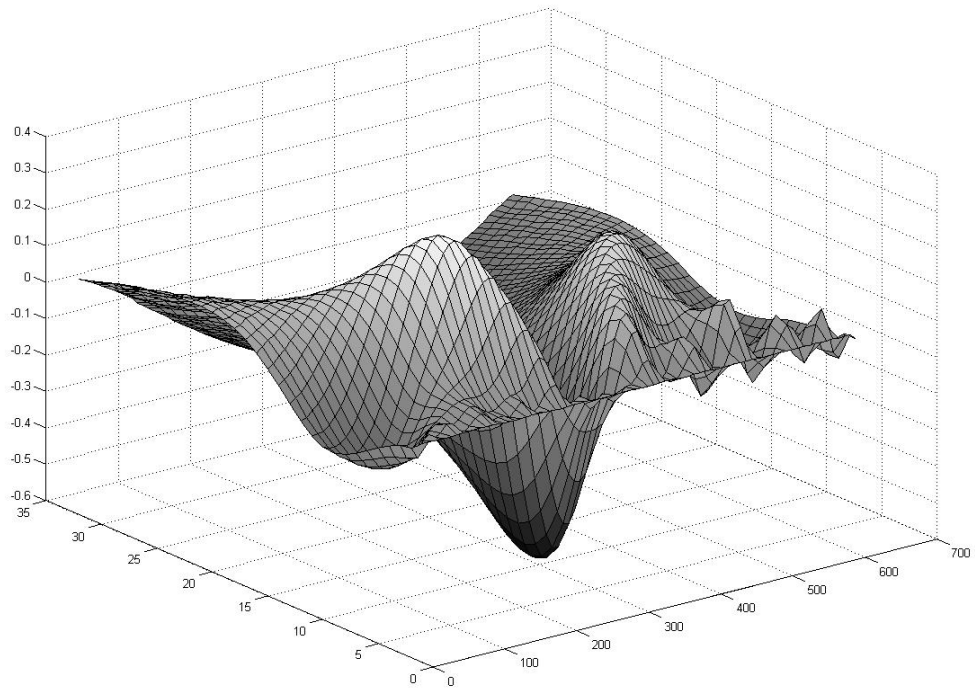


Figure 4.19 – Same as the previous plot, viewed from another angle.

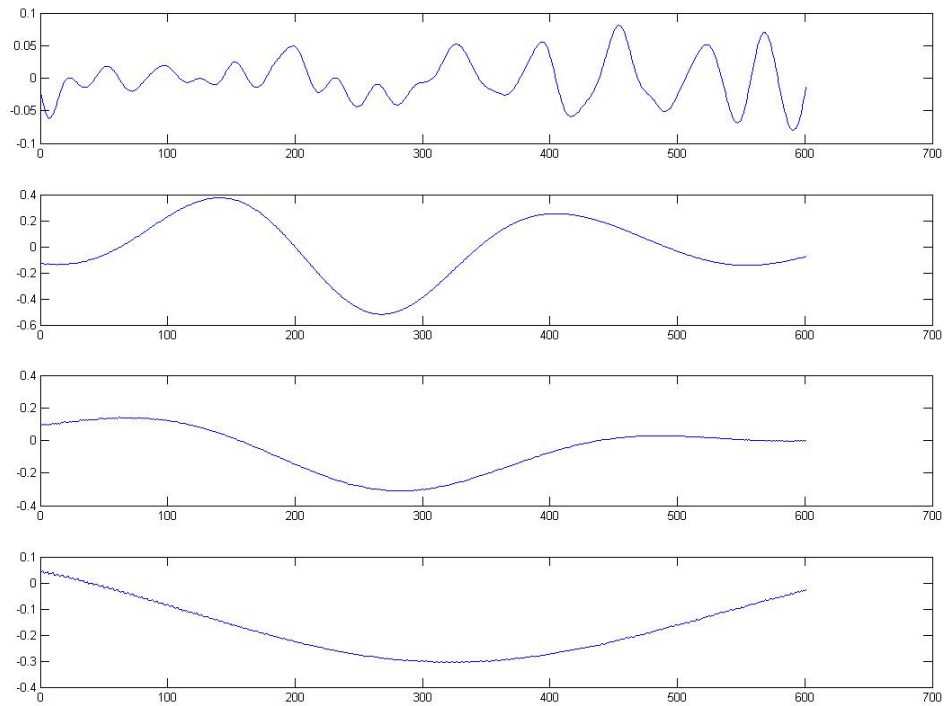


Figure 4.20 – Cross section of the wavelet transform in 4.18 and 4.19 at various dilation values.

The surface plot of the wavelet transform serves to illustrate several important factors. The front of the y-axis corresponds to the highest frequency in the signal, decreasing towards the lowest frequencies at the back end. It is clear that there is an optimal range of frequencies in which the absorption signal is most cleanly resolved.

One of the absorption samples recorded with zero gas in the cell that showed an unexpectedly high  $R^2$  (from the earlier data set represented in Fig. 4.16) is shown in figure 4.21, and another sample (also with 0 ppm) which showed extremely low  $R^2$  is shown in figure 4.22.

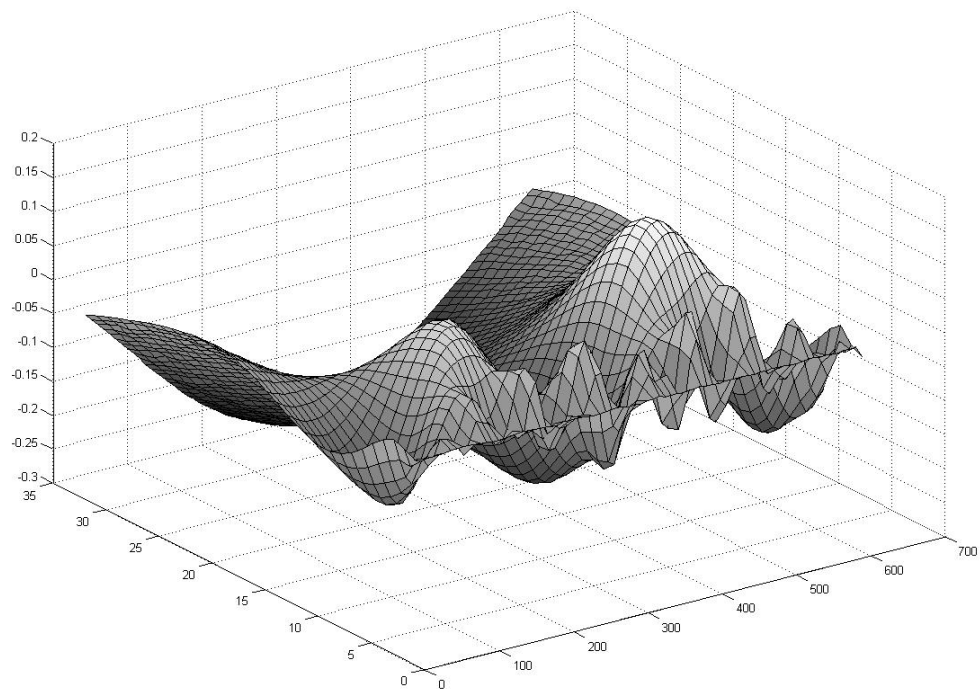


Figure 4.21 – Wavelet transform of 0 ppm signal (original  $R^2 = .25539$ )

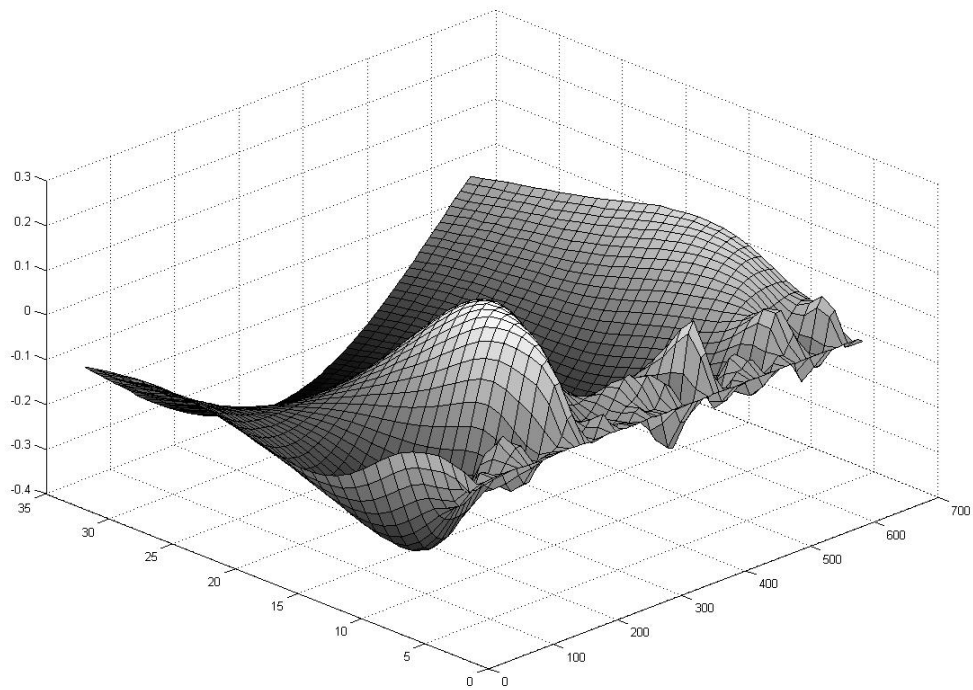


Figure 4.22 – Wavelet transform of 0 ppm signal (original  $R^2 = .00026$ )  
By using the wavelet transform on each data point on the 80 data points from figure 4.16, then selecting the frequency which produces the highest  $R^2$  with the original reference data, a new version of the figure can be generated, as shown below.

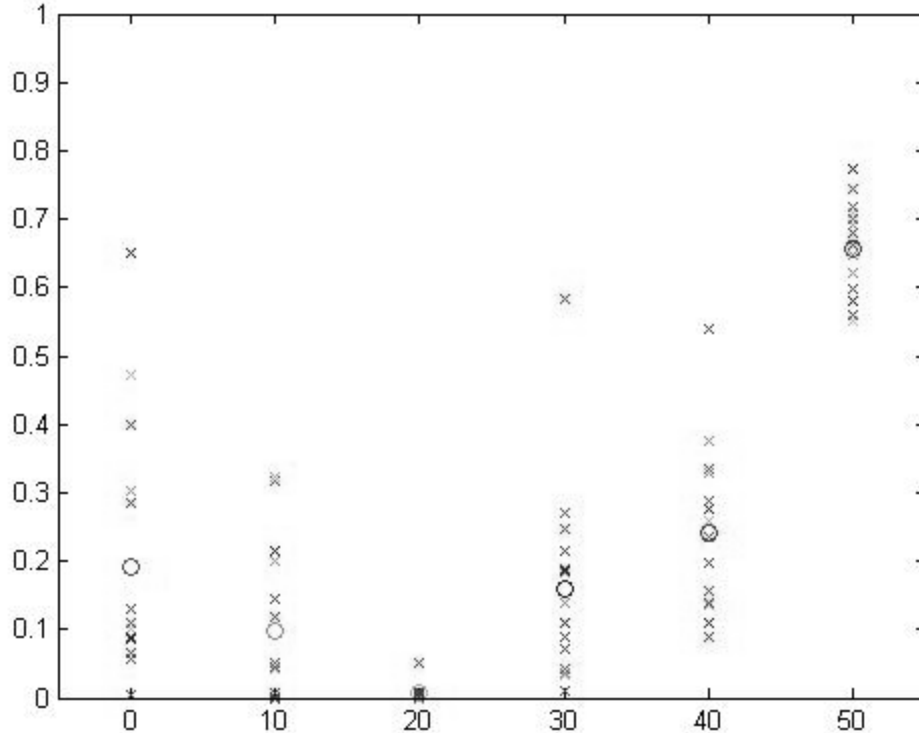


Figure 4.23 – Regression data set generated by using the maximum wavelet transform value for each point.

A comparison of figure 4.23 with the previous regression set in (4.16), it is clear that the wavelet transform has created an upward shift in the regression coefficient for nearly all of the non-zero data points. While the trend of the averages is still non-linear, this is an indication that the wavelet transform has potential for increasing system sensitivity by increasing the  $R^2$  values of the samples.

In using tools such as the wavelet transform on data sets, it is important not to compromise the integrity of the data. For example, arbitrarily adding in offsets and functions to augment a data set for better regression results would make the original data irrelevant. Figure 4.23 was generated by using the maximum value for the regression coefficient created by regression between the original reference sample, and the wavelet transform of each data point (the cross-sectional line of the surface plot that most closely correlates to the reference data). At this stage, it is unclear how to accurately predict the degree of data distortion introduced by regressing transformed signal against a genuine one, however, it is

useful to at least establish the boundaries. Several test situations were established in order to estimate the error/distortion induced by the wavelet transform:

- Regression of the wavelet transform of the reference with itself produced a maximum  $R^2 = 0.9303$
- A randomly generated vector ( $R^2 = .000423$  against the reference signal) produced a maximum wavelet transformed regression coefficient of .2802
- The average maximum  $R^2$  for each sample wavelet transform regressed against the original sample is .7349.

While an almost 30% reduction in the regression coefficient due to the wavelet transform is significant, the “smoothing” created by the transform eliminates some of the noise in the absorption signals. Figure 4.24 shows one of the nitrogen only samples, and the cross section of its wavelet transform that produces the highest  $R^2$  (.7384 in this case). The wavelet transform has removed a lot of the high frequency variation while still accurately approximating the overall shape.

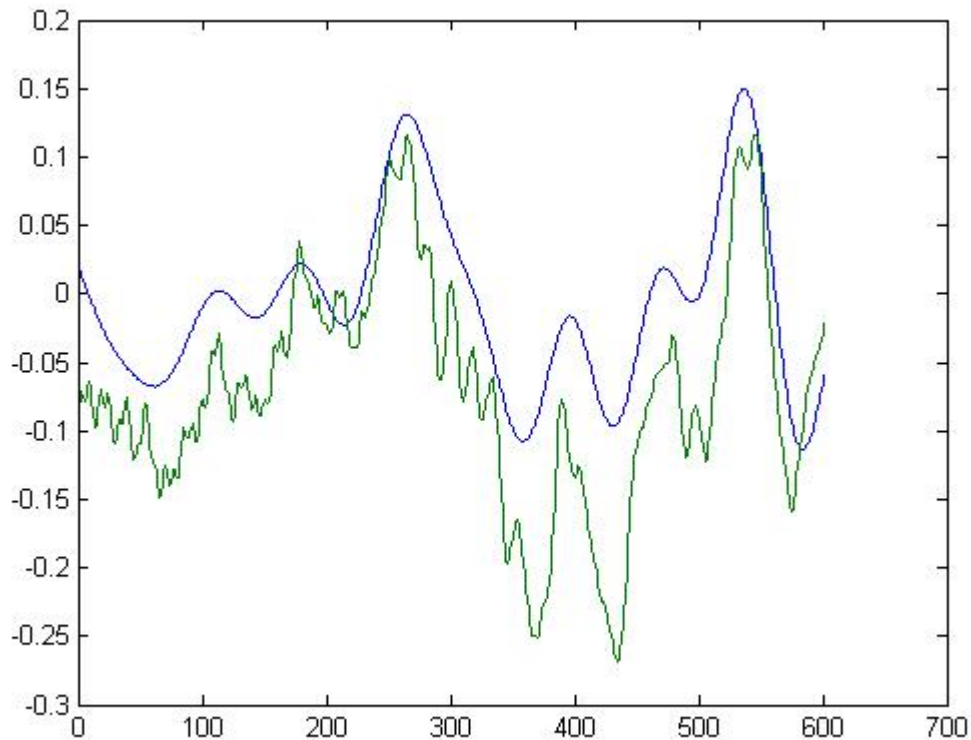


Figure 4.24 – A measured signal at the detector with only nitrogen in the cell (green), and its closest match generated by the wavelet transform (blue).

The wavelet transform can often increase the regression coefficient between a low concentration absorption signal and a reference, but not without inducing some distortion of the data. A more rigorous estimation of the error introduced by the transform, as well as further exploration of other wavelet families (such as Morlet or Daubechies) is needed before definite conclusions can be drawn. However, early results using the wavelet transform indicate potential for increased sensitivity when applied to absorption spectroscopy.

## **4.8 Noise Factors**

It is highly relevant to understand all of the contributing noise factors that limit the performance of the system, and what can be done to improve the detection limits of the system. All electrical systems generate some thermal noise, and therefore the driver circuitry, the photodetector system and the receiver circuit all produce some noise. In addition, electrical systems tend to pick up noise from power supplies, as well as external radiation sources. Radiative noise is generally periodic and non-random, often produced by other electrical devices such as computers. The easiest method for eliminating radiation problems is simply by physically isolating circuitry as much as possible with a conductive container. Power supply noise is mainly a concern when dealing with AC outlets. Even most standard supply cables that convert an AC source to 5 or 12V DC leave considerable 60 Hz residue which can adversely affect circuitry performance. The noise often observed at 60 Hz is easily avoided by employing batteries wherever possible, which generally have extremely low supply noise. Most thermal noise produced by electrical circuits is Gaussian distributed white noise, which means that the noise averages to zero. In these experiments, large amounts of averaging did indeed remove virtually all traces of thermal and white noise sources.

Of more importance to the system's noise performance are the "synchronous" noise sources. These are signals which do not average to zero and are generally on the same approximate frequency order as the absorption feature

itself, which makes filtering the noise also extremely difficult. Synchronous noise sources are much more difficult to identify and even more so to eliminate. Some sources of potential synchronous noise include the laser itself, etalon effects produced by lenses, and residual intensity modulation caused by the modulation current.

An etalon is created simply by having a beam transmit through an interface with a different index of refraction than the normal medium (usually air). Any optical element with non-zero width will produce transmission resonances when the wavelength of the incoming light is an integer factor of the width. These resonance phenomena are often called etalon effects or Fabry-Perot resonators. Etalons are often used purposely in many optical applications, however, any optical element will produce some etalon effects even if that is not its intended use. Virtually all lasers require a collimating lens to properly focus the beam, and most systems also employ a collecting lens near the detector. In addition, the windows on either end of a gas cell, and even the glass protective cover on the photodiode also produce etalon effects. Both of these lenses can produce etalon transmission characteristics. The transmission produced by an etalon is a periodic waveform, and as such, will not average out to zero. In fact, if index and sizing of an etalon are on the right order, it is possible to produce an etalon frequency very similar to the signal generated by absorption. Clearly such an effect is highly undesirable, since etalon produced waveforms drastically reduce the ability to resolve the absorption signal. For this reason, it is important to limit the number of optical transmission elements in the system wherever possible.

Most of the experiments performed included the following major optical elements: the collimating lens on the laser mount, the two windows on either end of the cell, and the collecting lens. The etalon frequency spacing for an optical element is given by:

$$v_F = \frac{c}{2nl \cos \theta} \quad (4.4)$$

where  $c$  is the speed of light,  $l$  is the length of the optical element,  $n$  is the index of refraction of the element, and  $\theta$  is the angle the incident light makes with the perpendicular axis of the lens. <sup>(28)</sup>

The collimating lens for the laser is a mounted aspheric lens from ThorLabs; part number C110TM-C. The lens is constructed from C0550 corning glass ( $n = 1.58572$ ), and has a maximum width of 5.36 mm. The light from the laser is incident along the perpendicular axis of the lens, resulting in an etalon spacing  $\nu_F = 17.65$  GHz.

The windows on either end of the cell are from Melles-Griot, and fabricated from BK7 glass, with thickness 3.6 mm and are mounted on an angle such that the laser light is incident at 57.3 degrees (this angle corresponds to the Brewster angle for the lens, ensuring maximal transmission and minimal reflection). From equation 4.4, the etalon spacing for each lens is  $\nu_F = 50.74$  GHz.

The collecting lens is also from ThorLabs; part number LA1951-C. It is a plano-convex lens constructed from BK7 glass ( $n = 1.52$ ), 25.4 mm in diameter and 11.9 mm wide along the central axis. Again, the VCSEL beam is along the central axis of the lens, producing an etalon frequency of  $\nu_F = 8.29$  GHz.

To determine whether or not etalon effects play a role in the noise sources, the frequency range scanned by the laser must also be calculated. As mentioned earlier in section 4.2, the laser was estimated to sweep a wavelength range of 1650.5 nm to 1651.5 nm during ramping modulation. This range of wavelengths corresponds to approximately 110 GHz of frequency variation in each period. Each of the optical elements in the system has etalon spacing within this range, meaning that these effects are potentially significant contributing factors to system noise.

In most semiconductor lasers, contributions from higher order modes and mode hopping under modulation conditions are a significant source of noise. Fortunately, due to the extremely low overall length of the VCSEL resonator structure, mode hopping is generally non-existent. <sup>(6)</sup>

Several experiments attempting to isolate and characterize sources of noise in the system were performed. In one test, the collimating lens was removed from the VCSEL, as well as the collecting lens, and the detector was placed directly in front of the laser. Under these conditions, no etalon effects should be possible, however, the beam diverges quickly, so it is not a practical usage for the laser in general. Figure 4.25 shows the results of this test.

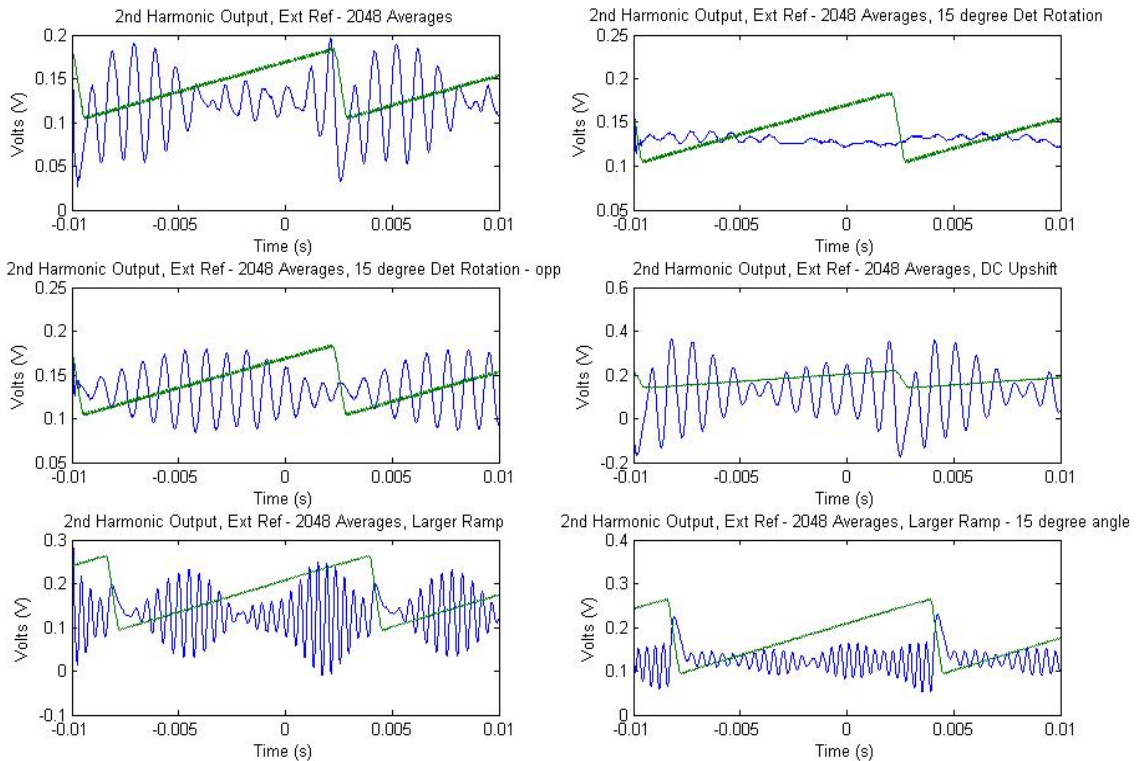


Figure 4.25 – Averaged 2<sup>nd</sup> harmonic outputs with no optical elements in the system.

In the first case, the photodetector is directly facing the laser. The second and third cases show the effect of rotating the face of the detector with respect to the laser. The fourth case considers the effect of changing the bias current of the laser, while the final two situations involve using a larger ramp. The results of these measurements allow us to draw several important conclusions. Clearly, due

to the extremely short path length and lack of optical elements, the periodic waveforms are not products of absorption or etalons effects. Although rotation of the detector affects the amplitude, the periodic noise remains, despite a large number of averages. It is interesting to note that approximately doubling the amplitude of the ramp leads to around double the frequency of the noise signal. The synchronous noise produced in this system appears to be generated by the laser, with a significant distortion due to feedback.

#### **4.9 Distributed Feedback Laser (DFB) Characterization**

In attempting to create a VCSEL based spectroscopy system, it is relevant to consider how a similar system performs when employing a different type of laser. Distributed feedback laser systems constructed with edge emitting laser diodes are a popular choice in the TDLAS field. A commercial DFB spectroscopy laser system from Boreal Laser was used for a performance comparison with the VCSEL.

This experiment is intended to compare the noise performance of the VCSEL and DFB lasers using the same receiver. A true direct comparison is difficult, since the lasers have greatly differing system requirements, however, useful results are still produced. Because the DFB laser diode is a much more powerful laser than a VCSEL, a separate driver (also from Boreal) is used; for the same reason, a different photodetector is required as well. The experimental setup is similar to before, the driver and laser head are mounted to one end of the optical table, the light travels through the gas cell before reaching the photodetector. The PLL based receiver is connected to the detector, and the resultant signal is measured with an oscilloscope. The DFB driver lacks the monitor outputs that the VCSEL driver has, which made it impossible to know the exact bias and modulation current supplied to the DFB at a given operating point. The modulation to the driver was supplied by a function generator at a frequency of 160 Hz (the lowest frequency the DFB board was designed to support, but still nearly double the frequency used in most of the VCSEL measurements). Figure

4.26 shows the second harmonic output of the PLL receiver at several different modulation indices through a 1 meter cell filled with 50 ppm methane.

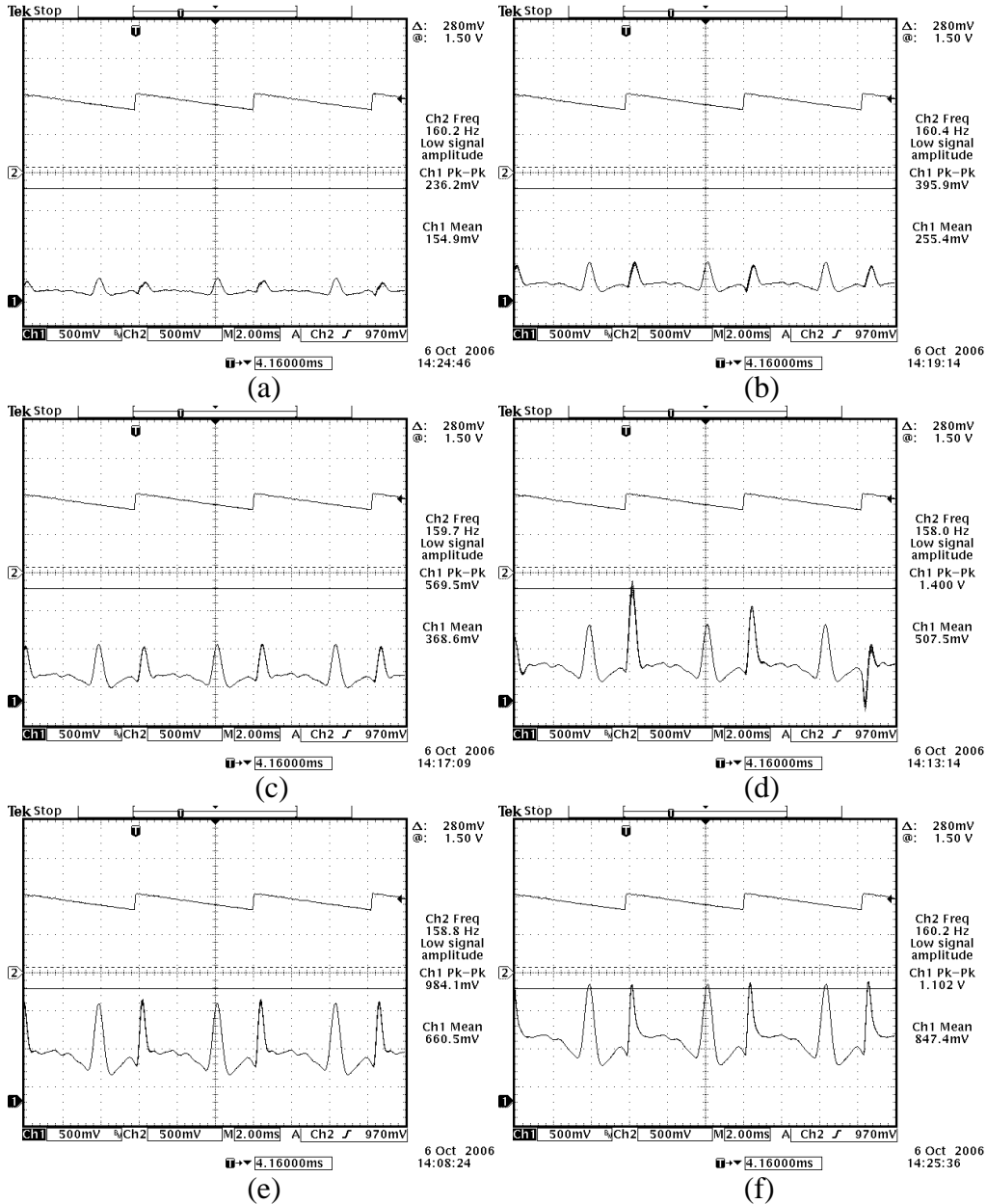


Figure 4.26 – PLL 2<sup>nd</sup> harmonic output using a DFB system, with modulation peak to peak voltage (a) 7 V (b) 9 V (c) 11V (d) 13 V (e) 15 V (f) 17 V. Cell concentration of 50ppm.

The switching spikes observed in Figure 4.26, which occur when the ramp rapidly jumps, are caused by a high duty cycle ramp (where the transition is 1% or less of the total ramp cycle). These spikes can be greatly reduced by softening the transition to 10-15%, but for the purposes of detection, these spikes should not be considered a noise source and can be safely discounted. The DFB generated

output shows similar results to the VCSEL, with higher outputs as the modulation index increases, but increased noise and drift as the index leaves the optimal range. The signal to noise ratio at this concentration is very similar for both laser types.

The fact that similar results were produced with a DFB system is another method for verifying the accuracy and versatility of the receiver system. In theory, the laser type should not matter, as long as the signal coming from the photodetector is resolvable. This experiment proves that a VCSEL system can operate (at least as well) as a DFB laser over short path lengths.

#### **4.10 Software and Hardware Receiver Comparison**

Most of the experimental results presented in this work were received with the analog detection system (either PLL or external reference), however, it is very useful to know how well this type of detection method compares to a digital receiver. The ability to use digital detection is an attractive option in spectroscopy since it has the potential for a great deal of flexibility. For example, a digital receiver can operate at many different ramp and modulation frequencies, as well as tune to different harmonics off the modulation frequency (some WMS systems use 3<sup>rd</sup> harmonic instead of 2<sup>nd</sup>). A digital lock-in receiver based in LabVIEW has been realized through the work of Aleksander Klyashitsky. The digital receiver functions in a manner very similar to the external reference receiver, although the reference is generated directly in software.

An open path characterization of the analog and digital receiver designs is used to compare their performance. The introduction of a high quality parabolic mirror rather than a lens for focusing the transmitted beam has allowed for much shorter path lengths. The experimental configuration is shown in Figure 4.27.

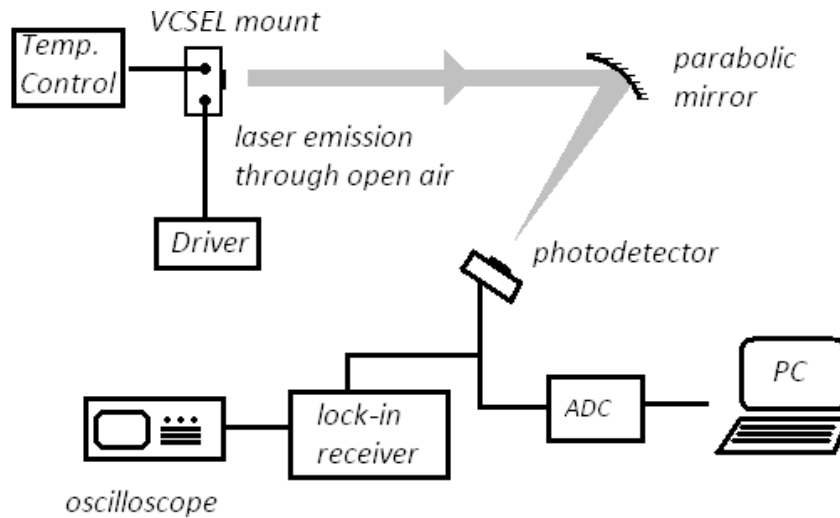


Figure 4.27 – Open path experiment for comparison of hardware and software lock-in receiver implementations.

The first comparison measurement is a high concentration reference. It is taken using a small reference cell inserted into a 4.0 meter path; the cell is equivalent to approximately 2000 ppm·m. The results for both hardware designs as well as the software result are presented in Figure 4.28.

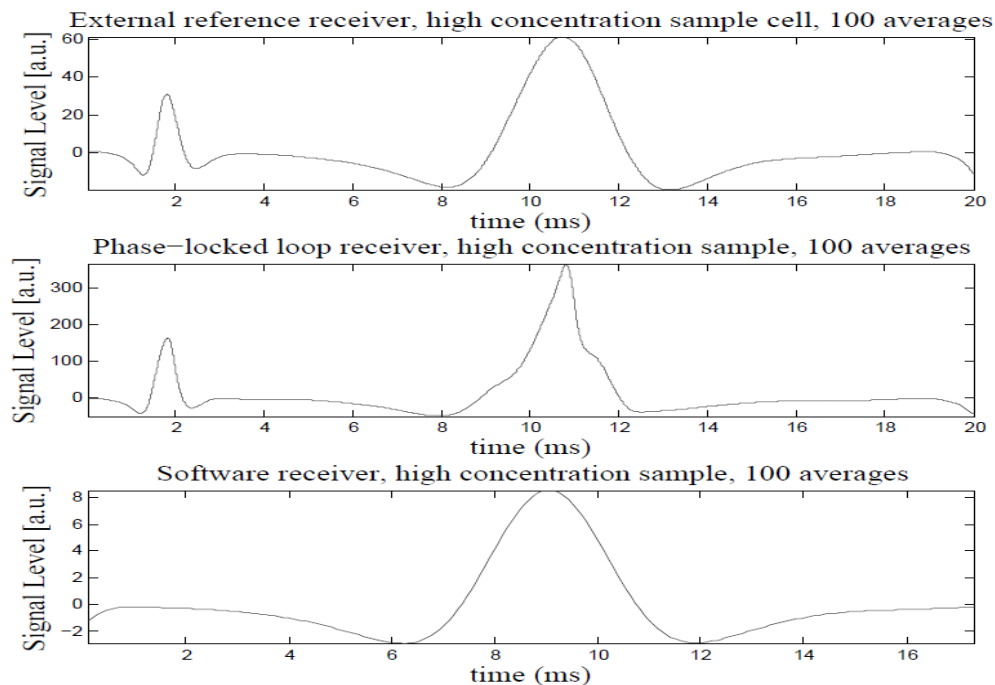


Figure 4.28 – Results from external reference hardware receiver (top), PLL receiver (middle), and software receiver (bottom) taken with a high concentration methane sample cell.

Clearly the results from the software receiver and the hardware external reference receiver are in fairly close agreement. The hardware versions both have a vestigial down-scan signal caused by the downward slope of the ramp, the software receiver does not show this signal since it triggers off the rising edge of the ramp. The phase-locked loop hardware receiver has failed in this case, the high concentration has caused overmodulation, leading to inaccurate results. The x-axis in Figure 4.28 corresponds to a 20 ms scan length, the hardware and software have a slight difference in total scan length due to a difference in triggering. The amplitudes in each case differ due to more amplification in the hardware versions, while the software receiver is normalized to the amplitude of the first harmonic. In later results, the down-scan section of the ramp has been removed from hardware samples to achieve a more accurate comparison.

With the system properly aligned using the high concentration cell, open path measurements are also recorded. Figure 4.29 shows the results of each system over a 4.0 meter open path. The external reference receiver shows excellent agreement with the software receiver in this case.

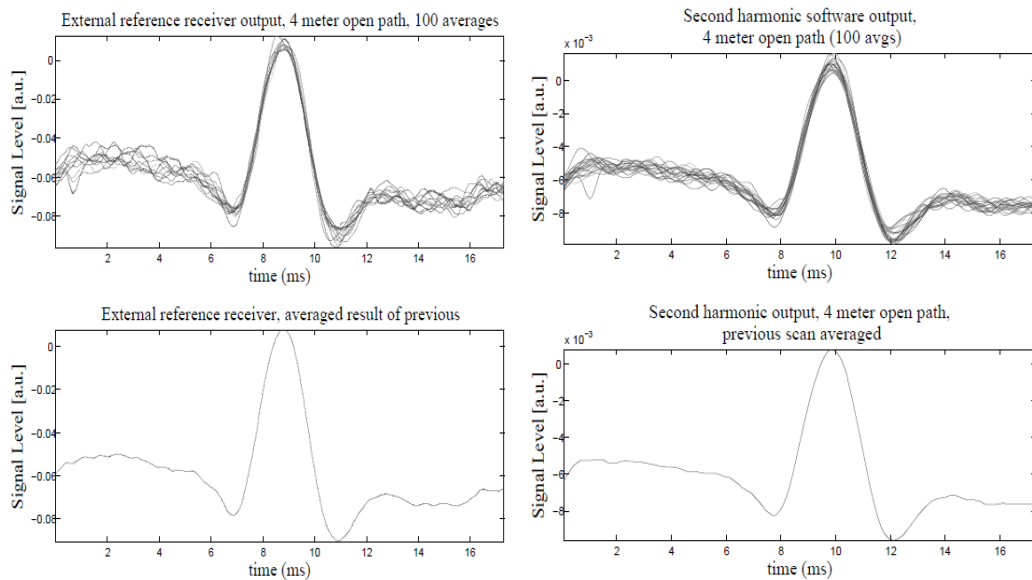


Figure 4.29 – Receiver results over a 4.0 meter open path (top left) hardware external reference receiver, 10 scans, each averaged 100 times, (bottom left) hardware external reference receiver all scans averaged, (top right) software receiver 10 scans at 100 averages each, (bottom right) average of previous software scans.

The quality of the results over a 4.0 meter path length encouraged us to take further readings at even shorter path lengths to attempt to determine the sensitivity limits of each system. The same experiment is conducted over a 1.0 meter path length, the results of which are portrayed in Figure 4.30.

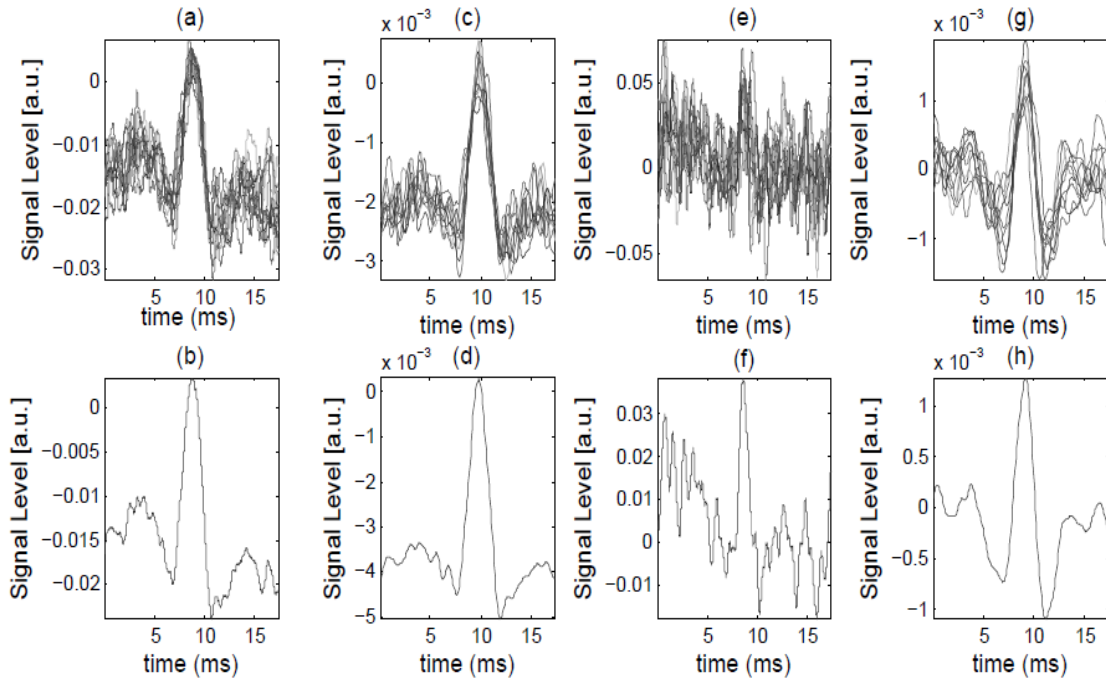


Figure 4.30 – 1 meter open path results (a) hardware external reference receiver, 10 scans of 100 averages each, (b) average of the 10 hardware external reference scans, (c) comparison result from software, 10 scans of 100 averages, (d) aggregate software scans, (e) PLL receiver, 10 scans of 100 averages each, (f) average of the 10 PLL scans, (g) comparison result from software, 10 scans at 100 averages each, (h) aggregate of the 10 software scans.

The results over a 1.0 meter path length begin to show significant separation in terms of performance between the different receiver implementations. The PLL system in particular suffers from very high random noise, as well as severe synchronous noise. As seen in Figure 4.31 (a), the absorption signal is almost indistinguishable from noise at 100 averages, while Figure 4.31 (c) which is equivalent to 1000 averages, does show an absorption signal, but with very poor signal to noise ratio. The external reference hardware receiver still shows fairly close agreement with the software version, but it is clear from Figure 4.30 that both random and synchronous noise sources are higher in the hardware receivers.

As always, reducing noise in the system is an important goal for attaining the best sensitivity possible. As previously mentioned, although random noise is undesirable, a great deal of it can be removed with averaging techniques. More averaging increases the amount of time needed to generate a clear signal, but it is fairly simple to implement. Reduction of synchronous or in-phase noise is generally a more important design consideration. One advantage of working with open path absorption is the reduction in optical elements in the system; since there are no cell windows or focusing lens, the only optical element which can create etalon noise is the collimating lens. Since the laser functions too poorly for useful operation without a collimating lens, etalon noise is minimized as much as possible. The other noise source which can play a significant role in some system is feedback. Figure 4.32 shows an experiment designed to reduce any contributions to noise from laser feedback, where the dark line is the emitted light, and the lighter line represents the path of any reflected power. The setup uses a 1.2 cm wide fused silica wedge as a beam splitter in the path of the laser emission. The wedge attenuates the amount of light reaching the detector, and any feedback from the detector will be further reduced by passing through the wedge once more. Electrical tape is used to block etalon reflection signals produced in the wedge. Under this experimental configuration, the power reaching the detector is measured as 7.3 times lower, which theoretically produces approximately 50 times less feedback power to the laser.

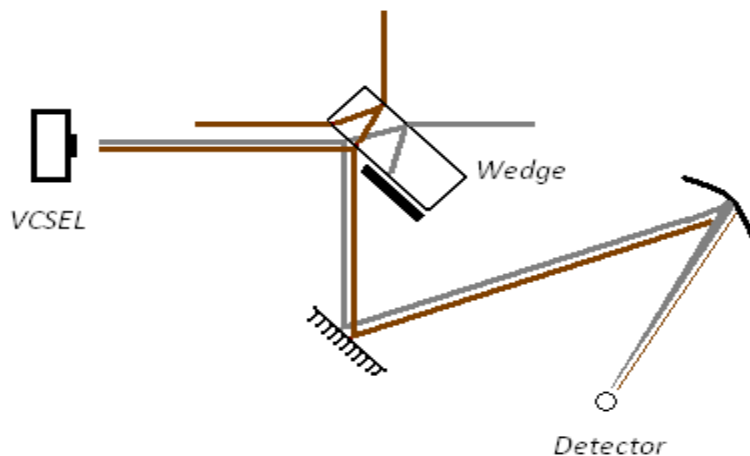


Figure 4.31 – Experimental system to reduce feedback noise.

The results of both the hardware external reference and software receiver systems in this experiment are shown in Figure 4.33. Once again both systems show remarkably similar performance, but the sensitivity of the systems has worsened in both cases. The reduced signal reaching the detector has introduced a significant amount of drift, which limits the performance of the system. In this case at least, the reduction in feedback noise caused by the introducing the wedge has not done enough to outweigh the corresponding reduction in signal power at the detector. Feedback remains an important consideration system design, but is evidently not a major sensitivity limiting factor in this instance.

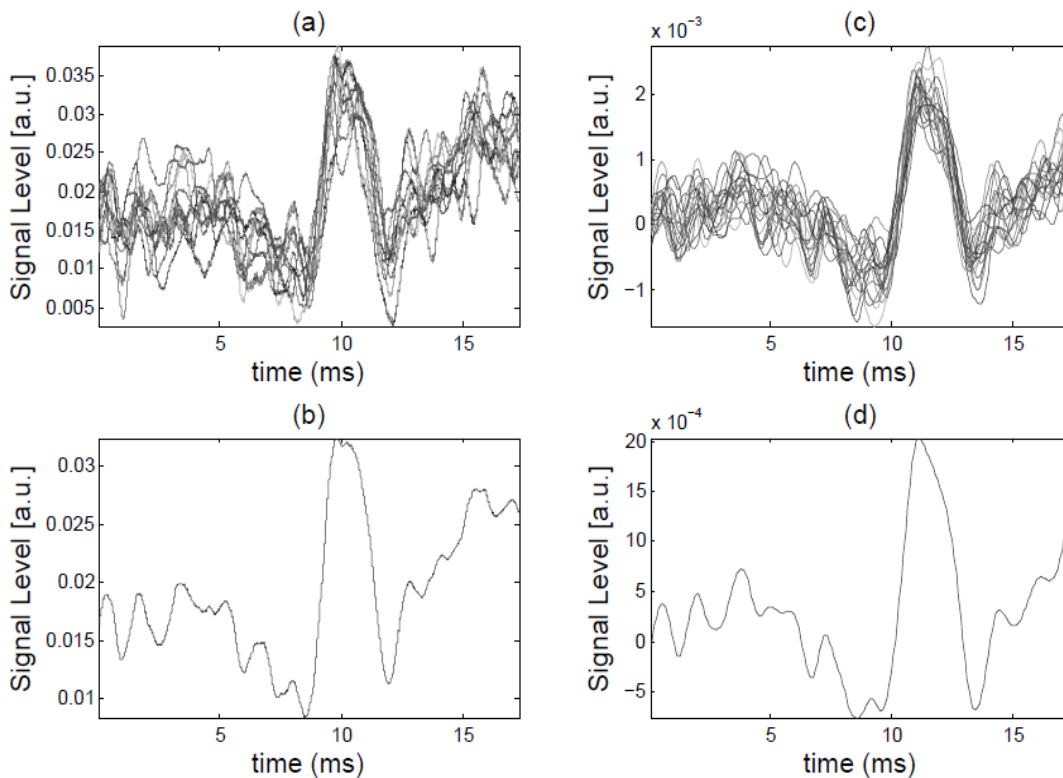


Figure 4.32 – Receiver results from 1.0 meter path with wedge (a) hardware external reference receiver, 10 scans at 100 averages each, (b) average of previous 10 scans from external reference, (c) software receiver, 10 scans at 100 averages each, (d) average of previous 10 software scans.

#### 4.11 Minimum Detectable Limit

The minimum detectable limit (MDL) of the system is an important metric for comparison with other systems and detection methods. Essentially, the MDL

is the operating point at which absorption signals become difficult to resolve from the noise in the system; the signal to noise ratio at or close to unity. The best results with the VCSEL spectroscopy system were attained in the experiments presented in section 4.10, and are used to calculate the minimum detectable limits for each receiver version. The signal to noise ratio is calculated using the simplistic method of dividing peak to peak signal value by the largest peak to peak noise value in the scan. The  $R^2$  value comparing each low concentration scan to a high concentration reference is also calculated for each receiver type. Although  $R^2$  cannot be directly linked to signal to noise ratio, it provides useful information about the accuracy of the signal. A value for  $R^2$  between 0 and 0.3 is very poor, indicating a noisy and potentially unreliable signal, between 0.3 and 0.5 is decent, while between 0.5 and 1 the correlation is strong and the signal may be considered relatively accurate<sup>(29)</sup>. The results for each receiver type are shown in Table 3. For finding the  $R^2$  metric in the PLL case, the high concentration reference from the external reference receiver is used since the corresponding PLL measurement is distorted.

	Linear regression coefficient of determination			Signal to noise ratio		
	External Reference	PLL	Software	External Reference	PLL	Software
4m open path	0.811	-	0.787	4.092	-	4.237
1m open path	0.742	0.178	0.914	2.146	1.121	4.342
1m open path with wedge	0.311	-	0.560	1.639	-	1.941

Table 3 – Regression coefficients and signal to noise ratios for different receiver implementations.

In order to estimate the MDL as accurately as possible, it is important to know the methane concentration in the laboratory environment. The indoor concentration is difficult to exactly predict, since it depends on the number of people in the area, air flow in the building, and even the time of day in some cases. Reported values for indoor concentrations generally vary between 2.0 and 3.0 ppm<sup>(30)</sup>, here we will assume the upper limit of 3.0 ppm for a conservative estimate. Based on an

ambient concentration of 3.0 ppm, the minimum detectable limit for each receiver type is estimated to be 1.4 ppm·m for the hardware external reference receiver, 0.7 ppm·m for the software receiver, and 3.0 ppm·m or higher for the PLL receiver. There is still room for improvement in the sensitivity by employing more averaging. The results used for these calculations had a total of 1000 averages, but tests at higher averages show there is still more random noise than can be removed. Although the capability exists to use almost arbitrarily high averaging, the time required to acquire an averaged signal must be considered. With the ramp frequency around 60-70 Hz, as in these measurements, each scan is 20 ms in length. A composite of 1000 averages requires 20 seconds, while 10,000 averages requires over three minutes. Depending on the application, acquisition times of several minutes may be too long, but we are confident that for the maximum sensitivity of each receiver can still be significantly improved with higher averaging.

The 1.4 ppm·m MDL of the external reference receiver is similar to results reported in literature involving other types of tunable diode lasers. As mentioned in section 2.6, Wainner (2002) built a handheld system and reported a sensitivity of 12 ppm·m, while Iseki (2004) estimated a MDL of 1.3 ppm·m (however the lowest measured value was 9.8 ppm·m). Based on the comparison between these reported findings, and those generated by these experiments, VCSELs compete very well with edge-emitting DFB lasers in terms of sensitivity. With very high averaging, it is possible that VCSELs may be slightly superior.

## Chapter 5: Conclusion

A working VCSEL spectroscopy system has been achieved. The system is capable of battery operation on the both the driver and receiving ends. At this juncture there is still the need for either an oscilloscope or computer in order to display the receiver output, although parallel work is ongoing to put this functionality onto a DSP chip. The VCSEL system shows excellent performance in resolving methane gas, both in cell measurements and in open path operation. Two hardware second harmonic receivers have been implemented, one based on a phase-locked loop, the other using an external reference from the driver to generate its mixing signal. After a detailed comparison, the external reference receiver proved to be significantly better in essentially every situation. The PLL system tends to fail at very high concentrations due to problems locking to an overmodulated signal, while the external reference receiver also shows much better sensitivity at very low gas concentrations. The only drawback of the external reference design is that the mixing phase must be manually configured, however once properly set it needed little adjustment. The MDL of the hardware configuration is estimated to be around 1.4 ppm·m, which is sufficient to detect ambient concentrations of methane over very short path lengths.

Although the realization of the hardware system was a success, the comparison to the software implementation leads to some important conclusions. In addition to showing better noise performance when compared to the hardware systems, the software system has many other important benefits. Using LabVIEW, it is fairly easy to adjust the receiver lock-in frequency to another value than 10 kHz, to adjust to a change in the ramp frequency in terms of filter cutoffs or to change to the lock-in detection harmonic. For example, although it is not presented here, measurements taken at higher modulation frequencies than 10 kHz (45 kHz in particular) showed an improvement in noise performance when using the software system. The hardware system cannot be tested at frequencies other than 10 kHz without a complete system overhaul. In addition, some tests

using 3<sup>rd</sup> harmonic rather than 2<sup>nd</sup> were also performed with the software system. Shifting to the 3<sup>rd</sup> harmonic produces a greater separation between the ramp and modulation frequency which makes filtering easier, and also provides greater isolation from residual amplitude modulation. The ideal harmonic, modulation and ramp frequency for a system is dependent many different factors, and the only truly effective method for determining the best operating point is to test a variety of scenarios. The versatility of software detection is uniquely suited to locating the best operating conditions for maximum sensitivity.

There are still several design obstacles which must be overcome in order to realize a portable implementation of VCSEL spectroscopy. The current design of the hardware receiver requires an oscilloscope to interpret the data, however capturing the receiver output with an ADC and using DSP chips for averaging and user interface is not particularly difficult. On the other hand, fully implementing the receiver into software by placing the ADC directly after the photodetector is a more complicated procedure. In this case, the DSP must perform the same operations that the LabVIEW program does. Currently a parallel project undertaken by other researchers in Dr. Tulip's group is close to implementing a DSP based software receiver. If the DSP implementation is as successful as the LabVIEW design, a portable receiver system should be attainable. The other important factor is the suitability of the VCSEL itself for open path portable applications. This research has proven that VCSELs can detect ambient concentrations of atmospheric gases over short path lengths, but there are still some other important factors. We were unable to use VCSELs in back-scattered applications, where no retroreflector is used. Ideally, a portable gas sensing system would not require a retroreflector, and indeed several DFB based systems which do not require reflectors have already been demonstrated. In addition, the maximum path length of VCSEL sources is significantly shorter than DFB lasers. The longest tested path length in this research is 12.5 m, and it is estimated that the longest possible path lengths would not exceed 25-50 m. DFB lasers on the other hand are capable of path lengths well over 100 m. Depending on the target

gas, a long path length is often desirable due to many gases exhibiting much weaker absorption strengths than methane. In spite of these mitigating factors, the VCSEL has demonstrated that its sensitivity compares very well with DFBs over short path lengths. Combined with lower cost and superior tuning capability, the VCSEL can still be a useful source in certain spectroscopy applications.

## Bibliography

1. **McCartney, Earl.** *Absorption and Emission by Atmospheric Gases: The Physical Processes.* Toronto : John Wiley & Sons, 1983.
2. **The World Bank.** 2007 World Development Indicators. [Online] [http://siteresources.worldbank.org/DATASTATISTICS/Resources/table3\\_13.pdf](http://siteresources.worldbank.org/DATASTATISTICS/Resources/table3_13.pdf).
3. **Zoidis, John D.** The Impact of Air Pollution on COPD. *RT for Decision Makers in Respiratory Care.* Oct/Nov, 1999.
4. **Knox, E.G.** Atmospheric pollutants and mortalities in English local authority areas. *Journal of Epidemiology and Community Health.* May 2008, Vol. 62, pp. 442-447.
5. **Le Treut, H and Somerville, R.** *Climate Change 2007: The Physical Science Basis.* s.l. : Cambridge University Press, 2007.
6. **Silfvast, W. T.** *Laser Fundamentals.* s.l. : Cambridge University Press, 2004. pp. 591-592.
7. **Hollas, Michael J.** *Modern Spectroscopy, 4th Edition.* s.l. : John Wiley & Sons, 2004.
8. **Weisstein, Eric W.** A Lorentzian Function. *MathWorld - A Wolfram Web Resource.* [Online] <http://mathworld.wolfram.com/LorentzianFunction.html>.
9. **Schilt, S., Thevenaz, L. and Robert, P.** Wavelength modulation spectroscopy: combined frequency and intensity laser modulation. *Applied Optics.* 2003, Vol. 42, pp. 6728-6738.
10. **Arnott, Pat.** *Absorption by Atmospheric Gases.* Reno : University of Nevada (ATMS 749), 2008.
11. **Herzberg, Gerhard.** *Molecular Spectra and Molecular Structure I. Spectra of Diatomic Molecules.* Toronto : D. Van Nostrand Company, 1950.
12. —. *Molecular Spectra and Molecular Structure II. Infrared and Raman Spectra of Polyatomic Molecules.* Toronto : D. Van Nostrand Company, 1945.
13. **Chalmers, John M. and Griffiths, Peter R.** *Handbook of Vibrational Spectroscopy.* s.l. : John Wiley & Sons, 2002.
14. **Boudon, V. et al.** The vibrational levels of methane obtained from analyses of high-resolution spectra. *Journal of Quantitative Spectroscopy & Radiative Transfer.* 2006, Vol. 98, pp. 394-404.
15. **Rothman, L. S., et al.** The HITRAN 2004 molecular spectroscopic database. *Journal of Quantitative Spectroscopy and Radiative Transfer.* 2005, Vol. 96.
16. **Arndt, R.** Analytical line shapes for Lorentzian signals broadened by modulation. *Journal of Applied Physics.* 1965, Vol. 36, pp. 2522-2524.
17. **Goff, D. R.** *Fiber Optic Reference Guide: A Practical Guide to Communications Technology, Third Edition.* s.l. : Focal Press, 2002.
18. **Numai, Takahiro.** *Fundamentals of Semiconductor Lasers.* New York : Springer-Verlag, 2004.
19. **Wainner, R. T.** Handheld, battery-powered near-IR TDL sensor for stand-off gas detection of gas vapor plumes. *Applied Physics B.* 2002, Vol. 75, pp. 249-254.
20. **Iseki, T.** A portable remote methane detector using an InGaAsP DFB Laser. *Environmental Geology.* 2004, 46, pp. 1064-1069.

21. **Lackner, M. et al.** Demonstration of methane spectroscopy using a vertical-cavity surface-emitting laser at 1.68 microns with up to 5 MHz repetition rate. *Measurement Science and Technology*. 14, 2003, pp. 101-106.
22. **Totschnig, G. et al.** High-speed vertical-cavity surface emitting laser (VCSEL) absorption spectroscopy of ammonia (NH<sub>3</sub>) near 1.54 microns. *Applied Physics B: Laser and Optics*. May 2003, Vol. 76, pp. 603-608.
23. **Lackner, M. et al.** CO and CO<sub>2</sub> spectroscopy using a 60 nm broadband tunable MEMS-VCSEL at [similar to] 1.55 microns. *Optics Letters*. Nov 1, 2006, Vol. 31, 21, pp. 3170-3172.
24. **Houghton, J.T. et al.** *Climate Change 2001: The Scientific Basis*. International Panel on Climate Change. s.l. : Cambridge University Press, 2001. p. 248.
25. **Draper, Norman R. and Smith, H.** *Applied Regression Analysis*. New York : Wiley series in probability and statistics , 1998.
26. **Hashmonay, R. and Modrak, M.** *Assessment of hydrogen sulfide minimum detection limits of an open path tunable diode laser*. s.l. : ARCADIS, 2007. Corporate paper (#495).
27. **Addison, P.** *The illustrated wavelet transform handbook: introductory theory and applications in science, engineering, medicine and finance*. Bristol : Institute of Physics Publishing, 2002.
28. **Saleh, B. and Teich, M.** *Fundamentals of Photonics*. Toronto : John Wiley & Sons, 1991.
29. **Cohen, Jacob.** *Statistical power analysis for the behavioral sciences, 2nd Edition*. Hillsdale : Lawrence Erlbaum Associates, Inc., 1988.
30. **Gustafsson, U., Sandsten, J and Svanberg, S.** Simultaneous detection of methane, oxygen and water vapour utilising near-infrared lasers in conjunction with difference-frequency generation. *Applied Physics B*. 2000, Vol. 71, pp. 853-857.

# Appendix

## 1. VCSEL Data Sheet

**VERTILAS VCSEL Diodes**

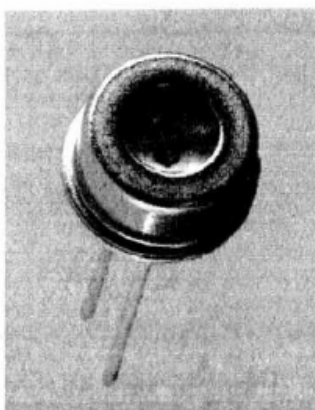


**FINAL TEST DATA**

Serial No. UBHR-SBBX-UAXW-A  
Type VL-1654-1-SE-R4

Page 1|3  
Date 2007-11-20

**Product State: Engineering Sample**



**Description**

The VL single-mode series diodes are VCSELs for customer specified emission wavelengths. The vertical cavity structure is employed to obtain excellent threshold and operating current and tuning performance. Typical range of operation is from 0°C to 50°C **in a non-condensing atmosphere.**

**Applications**

- Tunable Diode Laser Absorption Spectroscopy
- Fiberoptical Light Source

**Features**

- Wide and fast tuning performance for insitu measurements in high pressure environments
- Customer specific packaging options (TO39, TO46 and others)
- Individual laser data sheets available

**Electrical / Optical Characteristics**

Serial No. UBHR-SBBX-UAXW-A

CW Current	Recommended Range	Maximum Ratings
	1.0 mA - 8.5 mA	10.0 mA

	Threshold Current	Max. Output Power
20 °C	0.71 mA	ca. 0.77 mW
30 °C	0.84 mA	ca. 0.64 mW

I <sub>ld</sub> (20°C)	1.06 mA	3.19 mA	5.30 mA	7.43 mA	9.55 mA
Wavelength	1650.77 nm	1651.43 nm	1652.33 nm	1653.47 nm	1654.88 nm
I <sub>ld</sub> (30°C)	1.26 mA	3.10 mA	4.96 mA	6.81 mA	8.65 mA
Wavelength	1651.97 nm	1652.55 nm	1653.37 nm	1654.35 nm	1655.49 nm

**CAUTION**

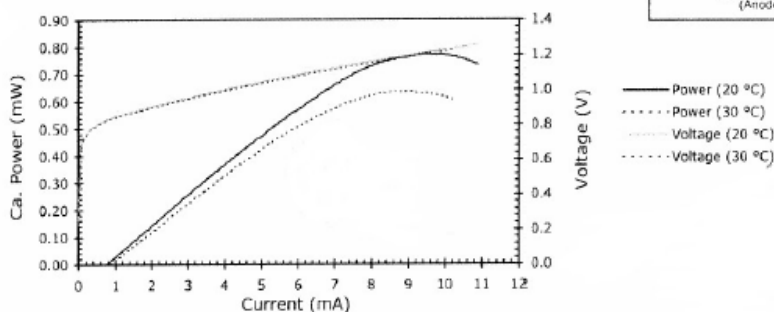
INVISIBLE LASER RADIATION  
AVOID EXPOSURE TO BEAM  
(CLASS 3B LASER PRODUCT)  
MAX 0.8 mW  
1653 nm

Complies with CE: EN60825-1:2006+A1:2009+A2:2011  
EN 60825-2:2003+A1:2009+A2:2011

**Pin Assignment  
(Bottom View)**

Isolated Pin =  
Minus Terminal  
(Kathode)

Ground Pin =  
Positive Terminal  
(Anode)

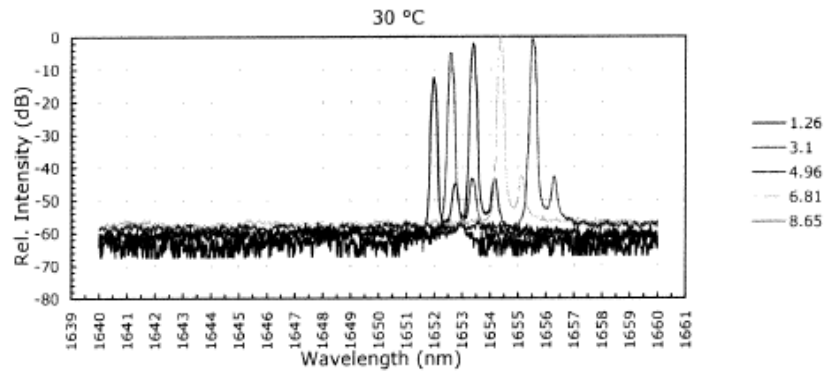
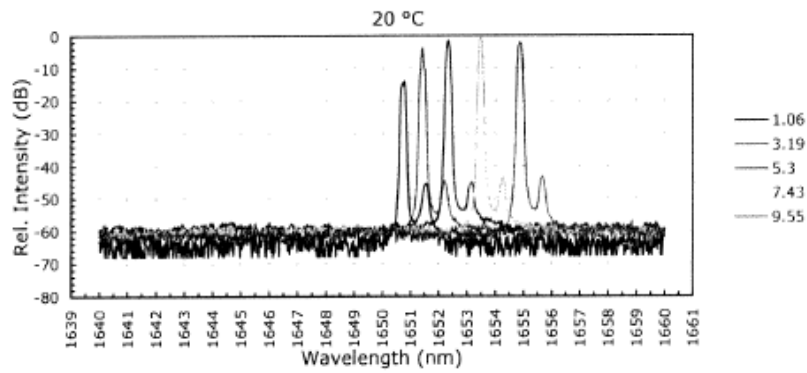
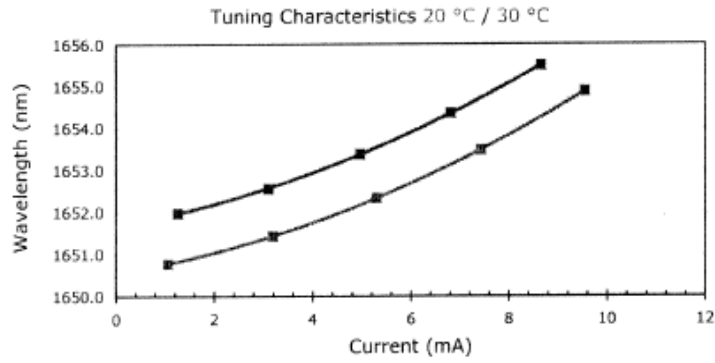


<b>VERTILAS GmbH</b> Lichtenbergstrasse 8 c/o Gate Garching D-85748 Garching	Tel.: +49 (0)89 54 84 20-00 Fax: +49 (0)89 54 84 20-19 www.vertilas.com	<b>Sales Requirements: sales@vertilas.com</b> Further information: info@vertilas.com
---------------------------------------------------------------------------------------	-------------------------------------------------------------------------------	-----------------------------------------------------------------------------------------

**FINAL TEST DATA**

Serial No. UBHR-SBBX-UAXW-A  
 Type VL-1654-1-SE-R4

Page 2 | 3  
 Date 2007-11-20



# VERTILAS VCSEL Diodes



**FINAL TEST DATA**

Serial No. HYFR-HHCA-CDJO-U  
 Type VL-1654-4-SP-A-WW

Page 1|2  
 Date 04.08.2004



**Description**

The VL single-mode series diodes are VCSELs for customer specified emission wavelengths. The vertical cavity structure is employed to obtain excellent threshold and operating current and tuning performance. Typical range of operation is from 0°C to 50°C.

**Applications**

- Tunable Diode Laser Absorption Spectroscopy
- Fiberoptical Light Source

**Features**

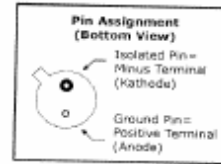
- Wide and fast tuning performance for insitu measurements in high pressure environments
- Customer specific packaging options (TO39, TO46 and others)

**Electrical / Optical Characteristics**

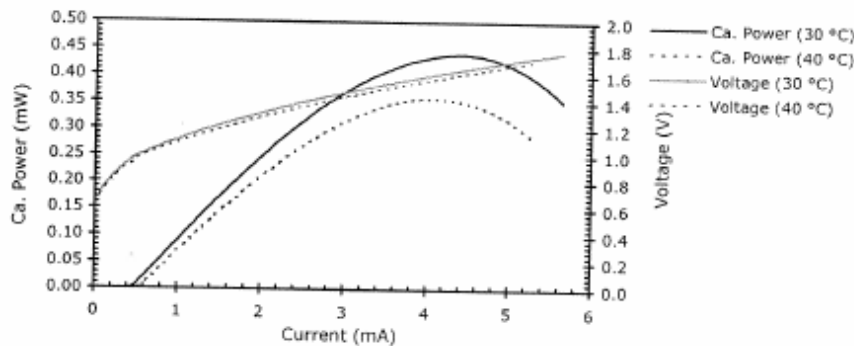
Serial No. HYFR-HHCA-CDJO-U

CW Current	Recommended Range	Maximum Ratings
	0.5 mA - 4.5 mA	5 mA

	Threshold Current	Max. Output Power
30 °C	0.41 mA	ca. 0.44 mW
40 °C	0.49 mA	ca. 0.36 mW



I <sub>ld</sub> (30°C)	0.61 mA	1.55 mA	2.48 mA	3.42 mA	4.36 mA
Wavelength	1651.17 nm	1651.89 nm	1652.71 nm	1653.71 nm	1654.80 nm
I <sub>ld</sub> (40°C)	0.73 mA	1.58 mA	2.42 mA	3.27 mA	4.11 mA
Wavelength	1652.49 nm	1653.17 nm	1653.89 nm	1654.77 nm	1655.74 nm

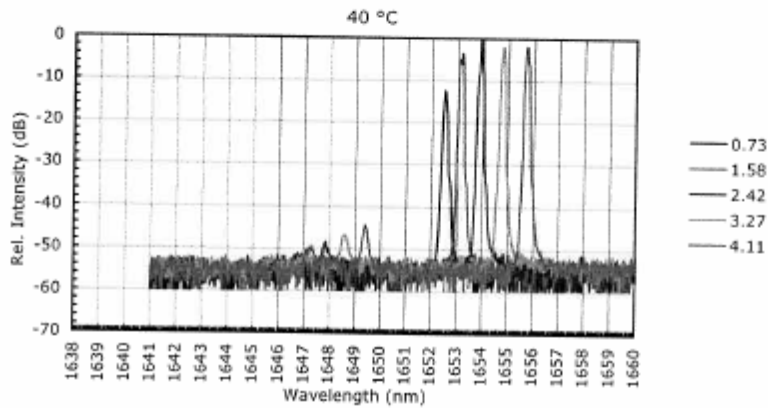
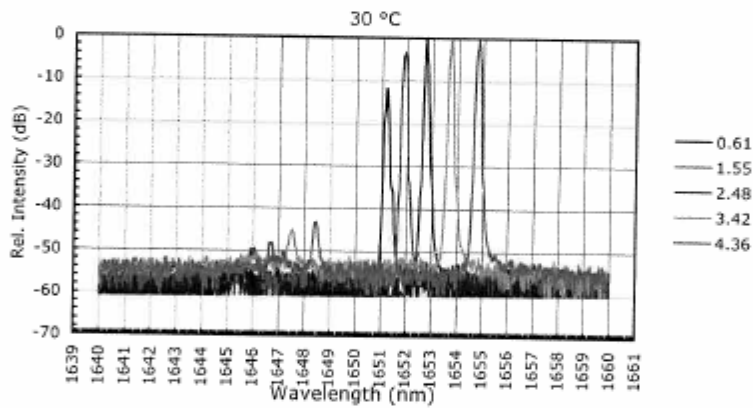
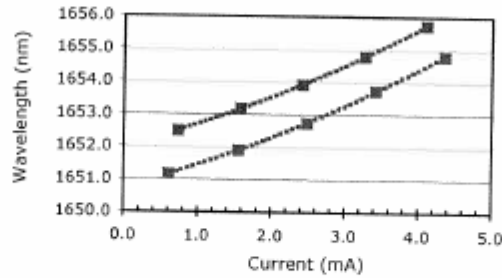


**FINAL TEST DATA**

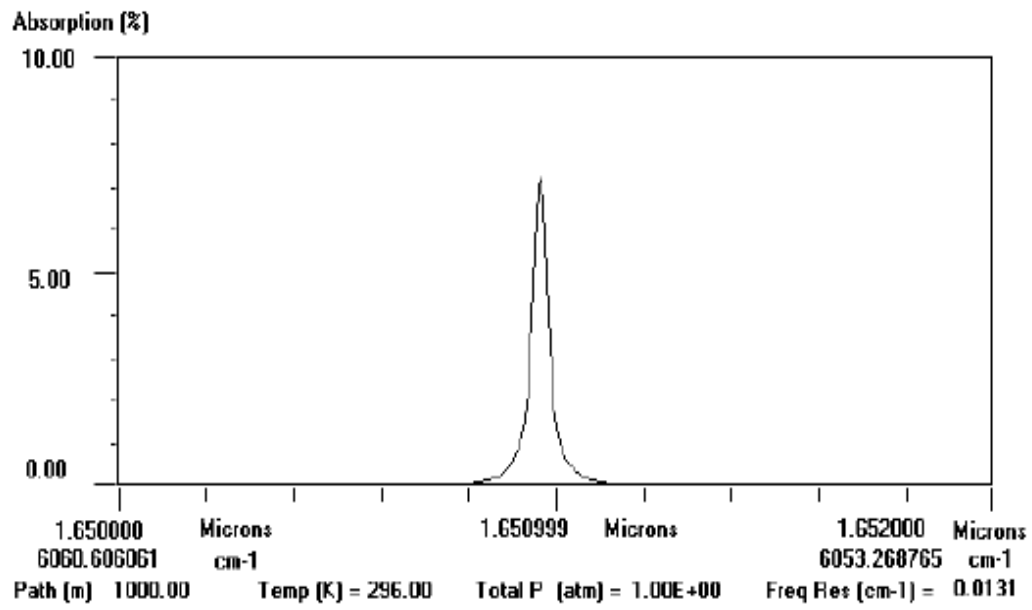
 Serial No. HYFR-HHCA-CDJO-U  
 Type VL-1654-4-SP-A-WW

 Page 2|2  
 Date 04.08.2004

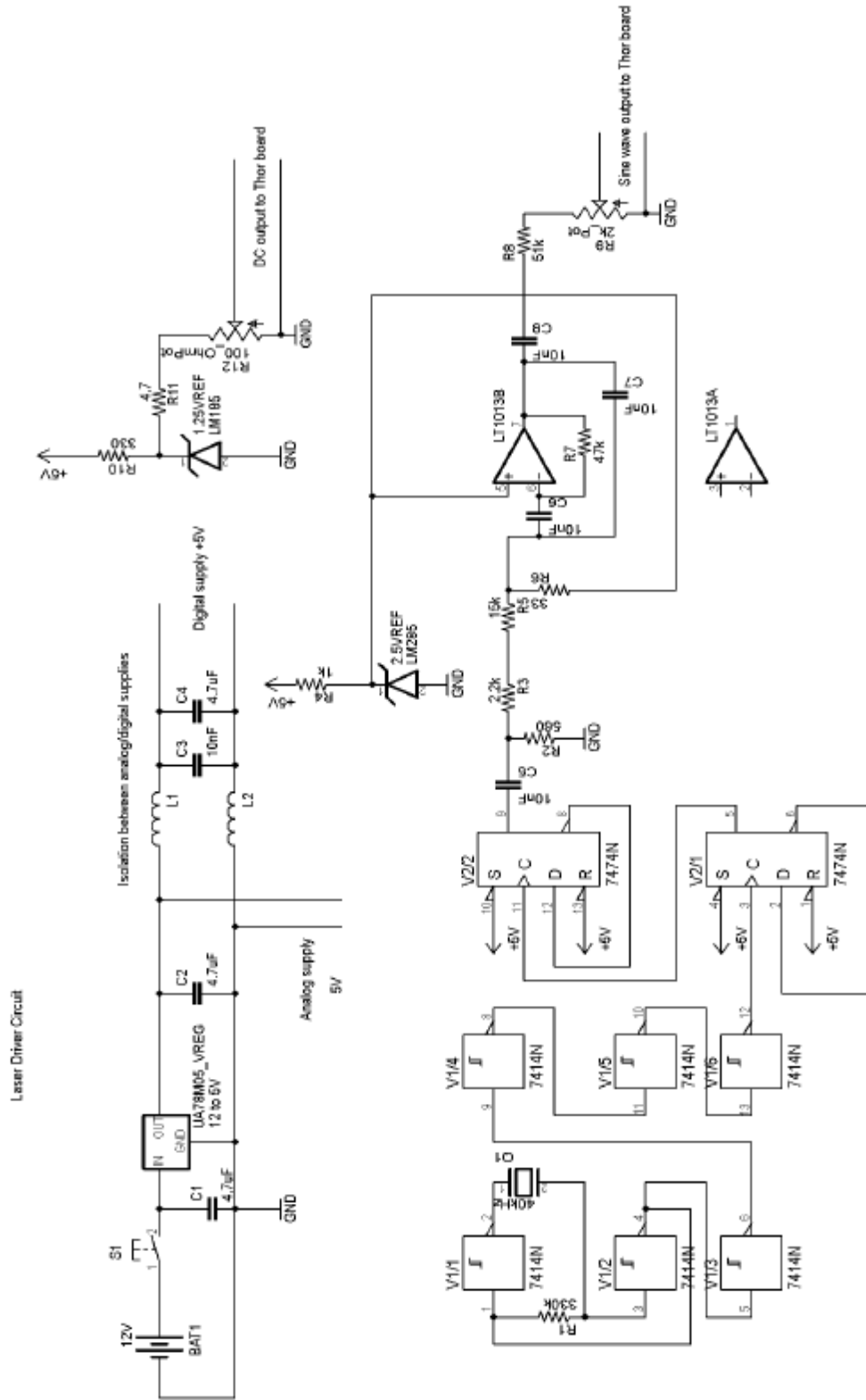
Tuning Characteristics 30 °C / 40 °C



### 3. HITRAN Data for CH<sub>4</sub> Near 1650 nm



#### 4. Laser Driver Circuit





## 6. External Reference Second Harmonic Receiver

